Universitat Autònoma de Barcelona

IMPROVING THE PERFORMANCE OF ORGANIC THERMOELECTRICS

Osnat Zapata Arteaga

OSNAT ZAPATA ARTEAGA

IMPROVING THE PERFORMANCE OF ORGANIC THERMOELECTRICS

IMPROVING THE PERFORMANCE OF ORGANIC THERMOELECTRICS

PhD thesis

OSNAT ZAPATA ARTEAGA

Supervisor: Mariano Campoy Quiles

Tutor: Aitor Lopeandía Fernández

Departament de Física
Facultat de Ciències

UAB

Universitat Autònoma de Barcelona

ICMAB
INSTITUT DE CIÈNCIA DE MATERIALS DE BARCELONA

EXCELENCIA
SEVERO
OCHOA

CSIC
CONSEJO SUPERIOR DE INVESTIGACIONES CIENTÍFICAS

February, 2021

Osnat Zapata Arteaga: *Improving the Performance of Organic Thermoelectrics,* February, 2021.

Dedicated to my wife, parents and sister.

ABSTRACT

In the current Internet of Things (IoT) era, smart sensing-devices are changing much about the world we live in, from how we sense our surroundings to the way we spend energy. On-site power generators for such devices will be essential, especially if they are maintenance-free, flexible, cheap, printable, or even disposable. Organic thermoelectric materials — semiconductors that can transform heat into electricity at near-room temperature — can fulfill these characteristics. Nevertheless, there are still issues in the current state-of-the-art materials that need improvement, such as the thermoelectric performance, benchmarked by the dimensionless thermoelectric figure of merit (ZT), and the thermoelectric stability under continuous thermal stress.

This thesis reports on strategies to improve thermoelectric efficiency and stability. As a testbed material system, we employ poly(2,5-bis(3-tetradecylthiophen-2-yl)-thieno[3,2-b]thiophene) (PBTTT) doped with the molecular acceptor 2,3,5,6-Tetrafluoro-7,7,8,8-tetracyanoquinodimethane (F4TCNQ). As a transversal tool for our studies, we developed high-throughput fabrication and characterization methods based on annealing-, doping- and thickness-gradients to study and correlate the relationship between microstructure, thermoelectric properties, and stability for many samples. The first set of results reports on a strategy to improve thermoelectric stability. We demonstrate that the formation of charge transfer complexes (CTCs) leads to more thermally enduring samples, although less electrically conductive. By developing a method to adjust the partial to integer charge-transfer ratio, we can improve the long-term stability without sacrificing the electrical conductivity. The subsequent chapter centers on the relationship between crystallinity and thermal and electric transport. We demonstrate that the degree of crystallinity largely determines the thermal conductivity of the film. Upon doping, even a relatively small dopant content increases the electrical conductivity several orders of magnitude but lowers the thermal conductivity without noticeable deterioration in the crystallinity. In the final chapter, we focus on a simple yet effective technique to simultaneously enhance the electrical conductivity and Seebeck coefficient. By using a matrix of PBTTT and adding small fractions of other polymers, such as regioregular poly(3-hexylthiophene) (RR-P3HT), we can enhance the order and microstructure quality of the film, improving the charge transport characteristics. While centered on a particular polymer and dopant combination, our results stretch the current knowledge of the relationship between the microstructure, thermal-electric transport, and stability.

LIST OF CONTRIBUTIONS

[1] Osnat Zapata-Arteaga, Bernhard Dörling, Aleksandr Perevedentsev, Jaime Martín, J. Sebastian Reparaz, and Mariano Campoy-Quiles. "Closing the Stability-Performance Gap in Organic Thermoelectrics by Adjusting the Partial to Integer Charge Transfer Ratio." In: *Macromolecules* 53.2 (Jan. 2020), pp. 609–620. DOI: `10.1021/acs.macromol.9b02263`.

[2] Osnat Zapata-Arteaga, Aleksandr Perevedentsev, Sara Marina, Jaime Martin, Juan Sebastián Reparaz, and Mariano Campoy-Quiles. "Reduction of the lattice thermal conductivity of polymer semiconductors by molecular doping." In: *ACS Energy Letters* 5.9 (Sept. 2020), pp. 2972–2978. DOI: `10.1021/acsenergylett.0c01410`.

LIST OF COLLABORATIONS

[1] Bernhard Dörling, Osnat Zapata-Arteaga, and Mariano Campoy-Quiles. "A setup to measure the Seebeck coefficient and electrical conductivity of anisotropic thin-films on a single sample." In: *Review of Scientific Instruments* 91.10 (Oct. 2020), p. 105111. DOI: `10.1063/5.0021715`.

[2] Jose Piers Jurado, Bernhard Dörling, Osnat Zapata-Arteaga, Alejandro R Goni, and Mariano Campoy-Quiles. "Comparing different geometries for photovoltaic-thermoelectric hybrid devices based on organics." In: *Journal of Materials Chemistry C* 1.207890 (2021), p. 3777. DOI: `10.1039/D0TC05067A`.

[3] Deyaa Abol-Fotouh, Bernhard Dörling, Osnat Zapata-Arteaga, Xabier Rodríguez-Martínez, Andrés Gómez, J. Sebastian Reparaz, Anna Laromaine, Anna Roig, and Mariano Campoy-Quiles. "Farming thermoelectric paper." In: *Energy and Environmental Science* 12.2 (2019), pp. 716–726. DOI: `10.1039/c8ee03112f`.

[4] José P. Jurado, Bernhard Dörling, Osnat Zapata-Arteaga, Anna Roig, Agustín Mihi, and Mariano Campoy-Quiles. "Solar Harvesting: a Unique Opportunity for Organic Thermoelectrics?" In: *Advanced Energy Materials* (2019). DOI: `10.1002/aenm.201902385`.

[5] Laura Ciammaruchi, Osnat Zapata-Arteaga, Edgar Gutiérrez-Fernández, Jaime Martin, and Mariano Campoy-Quiles. "Structure dependent photostability of ITIC and ITIC-4F." In: *Materials Advances* (2020). DOI: `10.1039/d0ma00458h`.

There ain't no surer way to find out whether you like people or hate them than to travel with them.

— Mark Twain

ACKNOWLEDGMENTS

First of all, I would like to thank Mariano Campoy Quiles for allowing me the opportunity of doing my Ph.D. studies under his supervision and, of course, for enduring the bureaucratic process required for hiring me in the first year. His help with accommodation long before I arrived to Spain was invaluable. Mariano was always patient and positive during my learning process. Moreover, he was really patient with my non-chatty personality and lack of skills for talking in public. It was indeed bliss having him as a supervisor.

I also want to express my gratitude towards Bernhard Dörling. I must say that to me, he was like a second supervisor, always willing to explain experiments and theory as many times it was needed. I really appreciated his help in proofreading most of my work during the Ph.D. and for not sugarcoating my mistakes (or maybe he was...). Without a doubt, that helped me improve the quality of my work.

Additionally, I want to express my gratitude to Juan Sebastián Reparaz for his on-to-one writing tutelage. I still have a lot to learn, but I leave with the motivation to keep learning the art of writing a scientific article and also my day-to-day results.

I also thank researchers from the NANOPTO group; Miquel Garriga, María Isabel Alonso, Alejandro Goñi, and Agustín Mihi. They were all super friendly during the last four years and always offered me a smile on the way through. I hope I can meet or read from them in the future.

I also have to mention Bartłomiej Twardowski, who taught me the basics of python for creating better figures and processing data. Now the only drawback is that I would like to pursue an in-depth computer science and data processing course.

I am incredibly thankful to Enrique Pascual for being super-friendly since day one I arrived in Spain. It was a joy to share the office with Enrique, Adrián Francisco, Bernhard, and Aleksandr Perevedentsev. Special thanks to Pau Molet and Leonardo Scarabelli, who helped me retake my climbing passion. I also thank Cristiano Matricardi, Camilla Dore, Martí Gibert, Pau, Begoña Buades, and Cristina Navarro, who were great company in the lab, outdoors, and during the trip to Mexico. I also have to mention my fellow students Mayte Gómez, Juan Luis, Valentina Belova, Luis Alberto, Xavier Rodriguez, José Jurado, Rana Adel, Miquel Casademont, Jinhui Hu, Albert Harillo, Minghua Kong,

and Kai Xu. It was a pleasure to share with them the time and space at ICMAB.

I also acknowledge my country's support, specifically by the Consejo Nacional de Ciencia y Tecnología (CONACyT) for the scholarship they provided me (no. 472571). While I felt somewhat frustrated over their recurring issues with my scholarship, the truth is that I owe them having completed my Bachelor, Master and now Ph.D. studies. I will undoubtedly try to repay my country in any manner possible for the support they have given me throughout my academic life.

Por último y más importante, le doy las gracias a mi esposa, madre, padre y hermana. Me brindaron su apoyo emocional en inclusive económico cuando tuve problemas con mi beca. Sencillamente no lo habría logrado sin su apoyo.

CONTENTS

I INTRODUCTION

II EXPERIMENTAL SECTION

III RESULTS

IV CONCLUSIONS

V APPENDIX

LIST OF FIGURES

LIST OF TABLES

ACRONYMS

OTE	organic thermoelectric
TE	thermoelectric material
TEG	thermoelectric generator
nMM	non metallic minerals
nFM	non ferrous metals
P	paper and printing
FB	food and beverages
IS	iron and steel
MO	molecular orbital
AO	atomic orbital
RRa-P3HT	regiorandom poly(3-hexylthiophene)
RR-P3HT	regioregular poly(3-hexylthiophene)
4T	quarterthiophene
PBTTT	poly(2,5-bis(3-tetradecylthiophen-2-yl)-thieno[3,2-b]thiophene)

BBL	poly(benzimidazobenzophenanthroline)
P3HT	poly(3-hexylthiophene-2,5-diyl)
PFO	poly(9,9-di-n-octylfluorenyl-2,7-diyl)
F4TCNQ	2,3,5,6-Tetrafluoro-7,7,8,8-tetracyanoquinodi-methane
F6TNAP	1,3,4,5,7,8-hexafluoro-11,11,12,12-tetracyanonaph-tho-2,6-quinodimethane
PCPDTBT	poly[2,6-(4,4-bis-(2-ethylhexyl)-4H-cyclopenta[2,1-b;3,4-b′]dithiophene)-alt-4,7(2,1,3-benzo-thiadiazole)]
PCDTBT	poly[N-9′-heptadecanyl-2,7-carbazole-alt-5,5-(4′,7′-di-2-thienyl-2′,1′,3′-benzothiadiazole)]
PTB7-Th	poly([2,6′-4,8-di(5-ethylhexylthienyl)benzo[1,2-b;3,3-b]dithiophene]3-fluoro-2[(2-ethylhexyl)carbonyl]thieno[3,4-b]thiophenediyl)
Li-TFSI	bis(trifluoromethane)sulfonimide lithium salt
TCNQ	tetracyanoquinodimethane
PEI	polyethylenimine
$PC_{71}BM$	[6,6]-phenyl-C71-butyric acid methyl ester
NDT	nap-htho[1,2-b:5,6-b′]dithiophene
BCF	tris(pentafluorophenyl)borane
PEDOT	poly(3,4-ethylenedioxythiophene)
PANI	polyaniline
TQ1	poly[[2,3-bis(3-octyloxyphenyl)-5,8-quinoxalinediyl]-2,5-thiophenediyl]
PC71BM	[6,6]-Phenyl-C71-butyric acid methyl ester
N-DMBI	4-(2,3-Dihydro-1,3-dimethyl-1H-benzimidazol-2-yl)-N,N-dimethylbenzenamine
N2200	Poly[N,N′-bis(2-octyldodecyl)-naphthalene-1,4,5,8-bis(dicarboximide)-2,6-diyl]-alt-5,5′-(2,2′-bithioph-ene)
PET	polyethylene
PS	polystyrene
PP	polypropylene
CB	chlorobenzene
DCB	1,2-orthodichlorobenzene
ICT	integer charge transfer
FCT	fractional charge transfer
CTC	charge transfer complex
IPA	ion pair
IE	ionization energy

EA	electron affinity
T_{subs}	temperature on the polymer's substrate
t_d	doping time
TAVD	temperature assisted vapor doping
E_F	Fermi energy
E_{tr}	transport energy
HOMO	highest occupied molecular orbital
LUMO	lowest unoccupied molecular orbital
SOMO	singly-occupied molecular orbital
DOS	density of states
E_g	band gap
PTFE	polytetrafluoroethylene
FTIR	fourier transform infrared spectroscopy
FDTR	frequency domain thermoreflectance
GIWAXS	Grazing Incidence Wide-Angle X-ray Scattering
AFM	Atomic Force Microscopy
W	free exciton bandwidth
DFT	density functional theory
NNH	nearest neighbor hopping
VRH	variable range hopping
PYS	Photoelectron Yield Spectroscopy
CV	Cyclic Voltammetry
Rh	Rheology
UPS	Ultraviolet photoelectron spectroscopy
DSC	Differential Scanning Calorimetry
T_g	glass transition
T_m	melting temperature
T_g^{blend}	glass transition of a polymer blend
ZT	thermoelectric figure of merit
FET	field-effect transistor
IoT	Internet of Things
CNT	carbon nanotubes
PSS	poly(styrenesulfonate)
Tos	tosylate
TDAE	tetrakis(dimethylamino)ethylene
GO	graphene oxide

FTS	tridecafluoro-1,1,2,2,-tetrahydrooctyl)-trichlorosilane
CPEs	conjugated polyelectrolytes
pg42T-TT	poly[3,3′-bis(2-methoxyethoxy)-5-methyl-5′-(5-methylthiophen-2-yl)-2,2′-bithiophene]
P3HTT	poly(3-hexylthiothiophene)
p(gNDI-gT2)	N2200 derivative
PTEG-x	family of fullerene derivatives prepared
OTS	trichloro(octadecyl)silane
PAc	polyacetylene
OCL	orientational correlation length
RSoXS	resonant soft x-ray scattering
CP	conjugated polymer
DMSO	dimethyl Sulfoxide
P3HTT	poly(3-hexylthiothiophene)
P3EHT	poly(3-(2′-ethyl)hexylthiophene)
NMR	nuclear magnetic resonance
CSA	camphorsulfonic acid
NDI	naphthalene diimide
TBAF	tetra-n-butylammonium fluoride salt (TBAF)
TAM	triaminomethane
CSM	conjugated small molecule

Part I

INTRODUCTION

1

MOTIVATION

The much-hyped IoT revolution where household appliances, clothes, vehicles, packaged goods, and buildings are interconnected and sharing information via machine-to-machine connections is just around the corner. Smart-sensing devices that are continuously mining data from the real and virtual world and subsequently turning it into actionable knowledge promise unprecedented innovation in agriculture, industry, commercial products, and services. For example, we already see aquaculture and agriculture operations equipped with wireless sensing devices performing real-time condition monitoring. The collected data is fed into an IoT platform that can allow prediction, warning, risk control, and on-demand micro-adjustments of the physical and chemical parameters, which can lead to cost savings or better products. [1, 2] A similar approach is the so-called Smart Building Management, in which proper control of the temperature and artificial lights, may result in significant energy savings.

The market value of IoT-related industries is estimated to evolve from a global \$3.9 to \$11.1 trillion US dollars, with the food-, sport-, health- and wearable-related sectors expected to have 70 % of market share by 2025. [3] However, the development of on-site power-generators for such devices is crucial, especially if they are desired to be maintenance-free, flexible, easily processable, or even recyclable.[4] Organic thermoelectrics (OTEs) —— semiconductors that convert heat into electricity —— have the potential to fill this particular niche.

1.1 POWERING THE IOT REVOLUTION USING WASTE HEAT

To date, batteries are the most practical solution for powering mobile and machine-to-machine IoT-related devices. [6] However, their utilization introduces miniaturization and design constraints related to the battery's mechanical- and lifespan characteristics. Energy harvesting technologies based on chemical, thermal, radiant, and mechanical sources are potential solutions. [2] Each has a particular niche depending on the on-site availability and intended application, nonetheless waste heat is probably the most ubiquitous. In this regard, on-site power generation, mainly through thermoelectric generators harvesting waste heat is highly attractive. [6, 7]

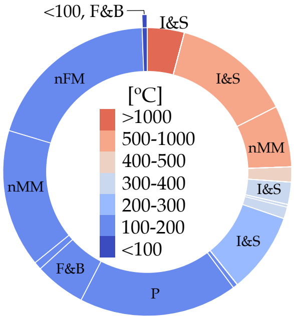

Figure 1.1: Waste heat fraction per temperature range and industrial sector:
Food and beverages (FB)
Iron and steel (IS)
Non metallic minerals (nMM)
Non ferrous metals (nFM)
Paper and printing (P)
data was compiled from reference [5]

WASTE HEAT POTENTIAL Sources of waste heat are everywhere, from heat stored in surfaces that are heated up by sunlight, to byproducts of metabolic and industrial processes. For example, only in the European Union, industry's estimated waste heat potential is 304.13 TW h/year and represents 9 % of its total industrial energy consumption. [5, 8, 9] The temperature range at which this energy can be harvested varies depending on the source. For instance, more that 50 % of the total waste heat potential is lost between 100 °C to 200 °C and is available in a large variety of industries, as seen in Figure 1.1. The waste heat potential above 300 °C represents roughly one third of the total one, and is found mainly in iron and steel industries. The fraction below 100 °C represent 1.25 TW h/year and is found mainly in the food industry. [5] Similarly, the human body wastes between 75 % to 95 % of the energy derived from metabolic processes as heat energy, but within temperature ranges around 35 °C to 37 °C. [10] In a few words, the most abundant waste heat potential lies below 200 °C, yet all these industries may potentially benefit from IoT-related technologies, either through a production- or management- approach.

1.2 BASIC PRINCIPLES OF THERMOELECTRICITY

When a temperature gradient is applied to a thermoelectric material (TE), carriers flow from hot to cold regions, generating a current flow and a voltage potential ΔV across the material via the Seebeck effect, as seen in Figure 1.2.

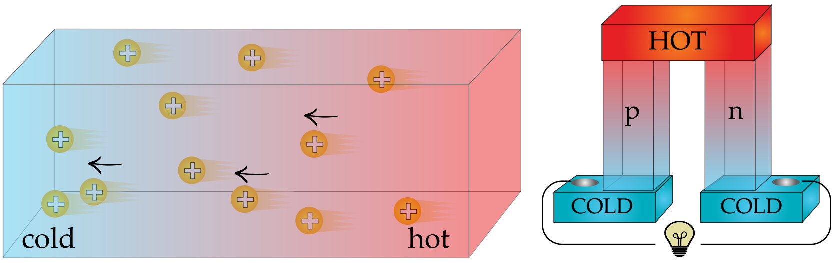

(a) Thermoelectric effect (b) Thermoelectric generator

Figure 1.2: (a) Schematic illustration of the thermoelectric effect and (b) of a thermoelectric generator with a single p- and n-type leg.

The magnitude of the voltage difference that builds up in an open circuit, is dependent on the applied temperature difference, as well as the material. Its sign also depends on the material and is negative for n-type (electron rich) and positive for p-type (electron deficient) materials. Thermoelectric generators (TEGs) are constructed from pairs of each type of material, interconnected electrically in series and thermally in parallel.

FIGURE OF MERIT ZT Benchmarking the thermoelectric performance of these materials is done using the dimensionless figure of merit, ZT, given in Equation 1.1

$$ZT = \frac{S^2 \sigma T}{\kappa_{tot}} \tag{1.1}$$

where S is the Seebeck coefficient, σ is the electrical conductivity and κ_{tot} is the total thermal conductivity and T the average temperature $(1/2(T_{\text{hot}} + T_{\text{cold}}))$. The larger the ZT, the better an application can benefit from an efficient thermal → electrical conversion. Thus, a good thermoelectric material is often referred to as a 'phonon-glass electron-crystal', meaning that the material should have a short phonon-mean free path and low thermal conductivity, but a long electron mean free path and high electrical conductivity.

Section 2.3 details the concepts of σ, S and κ

POWER FACTOR Besides the ZT, another method for judging the thermoelectric performance is through the power factor, $S^2\sigma$. The latter is particularly useful when measuring κ is complicated.

THERMOELECTRIC EFFICIENCY The thermoelectric efficiency (η) of a TEG is directly related to the ZT and the temperature difference (ΔT) following Equation 1.2.

$$\eta = \frac{\Delta T}{T_{\text{hot}}} \frac{\sqrt{ZT+1}-1}{\sqrt{ZT+1}+\frac{T_{\text{cold}}}{T_{\text{hot}}}} \tag{1.2}$$

where $\Delta T / T_{\text{hot}}$ is the Carnot efficiency and the rest of of the expression is the material-related contribution that depends on the ZT.

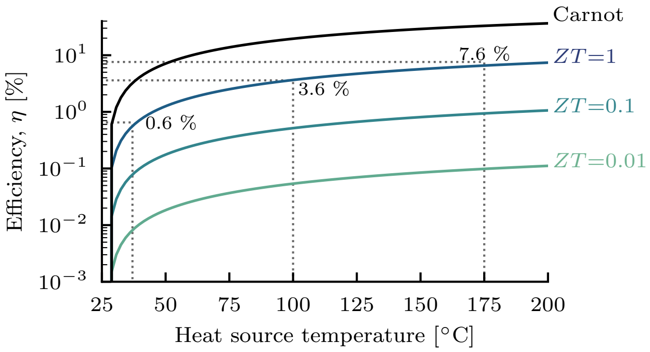

Figure 1.3: Variation of thermoelectric efficiency as a function of the hot-end-temperature calculated using Equation 1.2, values of ZT= 0.01, 0.1 and 1, and a T_{cold}=27 °C.

Thus, for a fixed ZT, η increases the larger the temperature difference is between the heat source and the cold side of the material, as seen in Figure 1.3.

1.3 WHY ORGANIC THERMOELECTRICS?

Research in thermoelectric materials has a long trajectory. Inorganic-based thermoelectrics such as Bi_2Te_3 is amongst the first studied materials with a reported *ZT* of 0.5 in 1958. [11] Since then, the thermoelectric performance of these materials, has significantly increased, as seen in Figure 1.4. To date, for near-ambient applications, the most representative materials are bismuth telluride (Bi_2Te_3), tin selenide (SnSe), lead telluride (PbTe), and silicon-germanium (SiGe). However, these materials are designed mostly for specialized cooling and heating applications due to their high cost, toxicity, and low flexibility. [7]

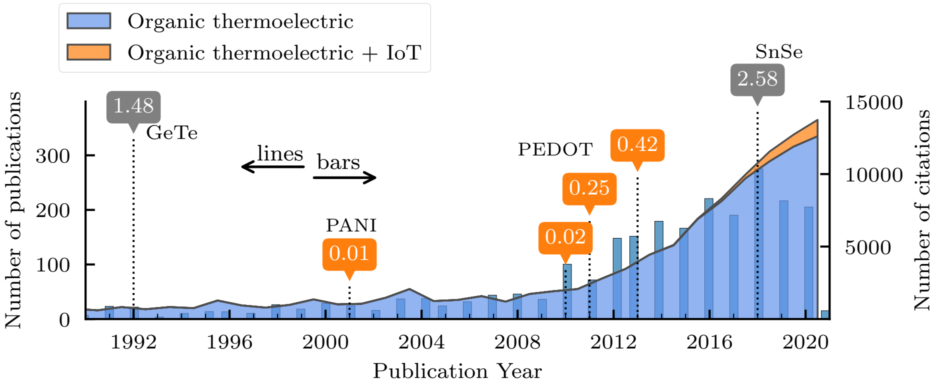

Figure 1.4: Data from the publication report using Clarivate Analytics Web of Science service and the words 'Organic thermoelectric' and 'Organic thermometric + IoT'. Data extracted on the 20, January 2021. Numeric labels indicate the *ZT* of selected inorganic-based (gray) [12, 13] and organic-based TE materials (orange). [14–17]

Conversely, development and research of organic semiconductors for OTEs materials lagged compared with their inorganic counterpart, (cf. Figure 1.4) at least until major breakthroughs by Bubnova et al. achieved a *ZT* of 0.25 [16] with poly(3,4-ethylenedioxythiophene) (PEDOT) and then by Kim et al. reaching a *ZT* of 0.42. [17] To a great extent, these milestones reignited interest from the scientific community towards OTE materials as seen by the rapid increase in the number of papers published and citations in the field (see Figure 1.4).

1.3.1 *Advantages of organic-based thermoelectrics*

Organic semiconductors also have other advantages that are particularly attractive for the development of powering alternatives for the IoT industry.

FLEXIBILITY AND PROCESSABILITY Flexible, foldable and mechanically robust OTE materials have been already fabricated from carbon nanotubess (CNTs)-, and PEDOT-based materials. [4, 18–20] Many organic semiconductors are also solution processable, which is highly attractive for printing techniques and for the fabrication of OTE fibers and textiles. [7, 21, 22]

ABUNDANCE The major constituting elements of organic semiconductors (i. e., carbon, oxygen, nitrogen and hydrogen) are more abundant in the Earths' crust than the rare earths and metals typically found on inorganic-based thermoelectrics. (cf. abundance values in Figure 1.5).

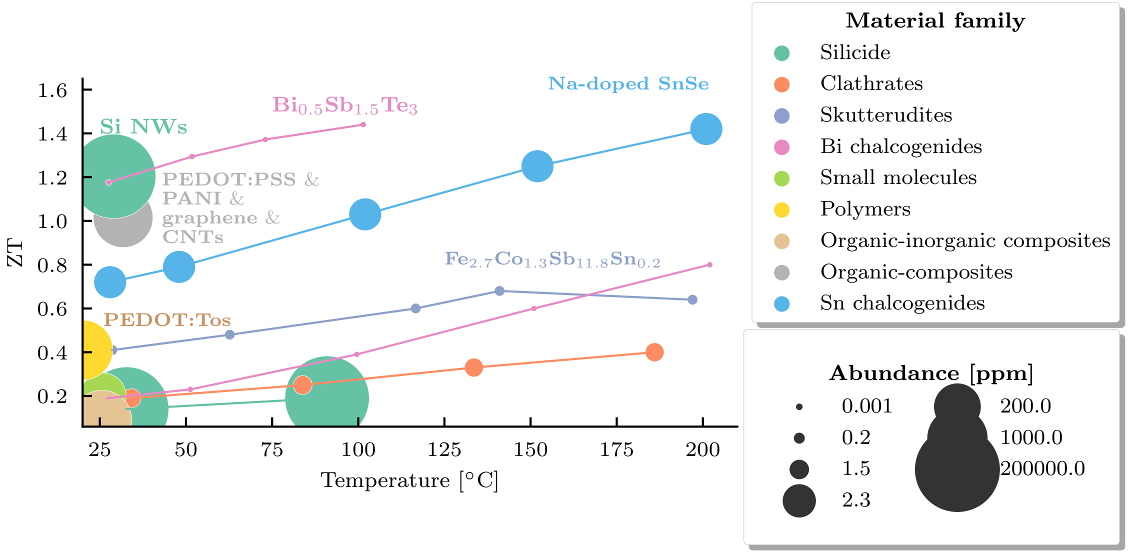

Figure 1.5: ZT as a function of temperature for representative material families. Data extracted from references [23]. Also for comparison, we show the abundance in the Earth's crust of the major constituting element of each represented family. Data compiled from reference [24]

COST Power conversion efficiency scales with $\Delta T/T_{\text{hot}}$ (Equation 1.2), thus, low-temperature applications are inherently less-efficient, and unsuited for expensive thermoelectric materials such as Bi_2Te_3. Furthermore, material scarcity plus high demand would inevitably lead to even higher prices. [7, 25]

TOXICITY Waste management and bio-compatibility are vital traits for devices fabricated in large quantities or designed to be wearable. Thus, for power sources containing bismuth, lead, arsenic, or indium, one can envision the need for additional safety measurements to prevent poisoning or contamination. The latter can have a significant impact in cost, and depending on the approach (e. g., when encapsulated) an impact on the mechanical properties of the device.

1.3.2 *Disadvantages of organic-based thermoelectrics*

The waste heat potential between 25 °C to 200 °C is particularly attractive for IoT-related applications. It contains industry segments expected to have a large market presence and also represents the largest fraction of the total waste heat potential shown earlier. As mentioned earlier, for such range, Bi_2Te_3-is probably the most relevant and efficient example currently available (cf. materials show in Figure 1.5). While not a definite rule, we can consider that an attractive TEG will be the one able to deliver the most power output per dollar and simultaneously in the widest operation range available. In this regard, we highlight two important aspects where OTEs require further improvement. (i) Thermoelectric performance and (ii) thermoelectric stability under continuous thermal stress and ambient exposition.

THERMOELECTRIC STABILITY Doping is a technique to improve σ in organic semiconductors. However, in many studied examples, dopants can react with the environment or diffuse out of the active layer after prolonged thermal exposure. In brief, the doped-state may not be stable under external stimuli, which impacts the thermoelectric efficiency, operation range and thus, the intended application. To date, there are only a handful of materials that are relatively stable above 100 °C or when exposed to air for prologued periods of time. Among them are some classes of polythiophene, naphthalene diimide (NDI) and fullerene derivatives that employ polar sidechains to improve the compatibility between the polymer and the dopant. [26–30] The limited pool of available materials with good thermoelectric stability highlights that further work is needed in this field.

The stability of thermoelectric materials will be further discussed in Section 3.4.

THERMOELECTRIC PERFORMANCE Even though organic-based thermoelectrics have traits that are appealing for the IoT industry, they still need to be able to power or at least charge devices in a way that surpasses current battery technology. However, improving the thermoelectric performance is far from a trivial task; the parameters that govern the figure of merit (i. e., S, σ and κ) are strongly correlated and typically counter-indicated, meaning that changing one parameter has a detrimental effect on another. The current OTE champions are the p-type PEDOT:poly(styrenesulfonate) (PSS) processed with dimethyl Sulfoxide (DMSO) and the n-type fullerene derivative PTEG-x doped with 4-(2,3-Dihydro-1,3-dimethyl-1H-benzimidazol-2-yl)-N,N-dimethylbenzenamine (N-DMBI), yet their *ZT* is still lower than that of Bi_2Te_3, as seen in Figure 1.6. What is needed is further understanding of the parameters that govern the figure of merit *ZT*, so that we may develop strategies to optimize it. A deeper discussion will follow in following chapters.

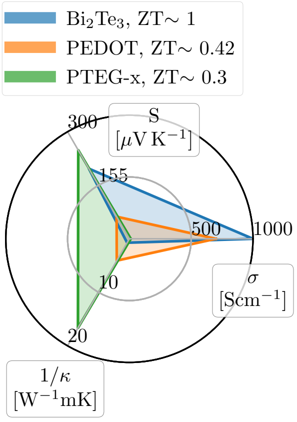

Figure 1.6: Caption

2

ORGANIC THERMOELECTRICS: MATERIALS AND KEY CONCEPTS

This chapter briefly introduces materials and concepts relevant to OTE research.

2.1 OVERVIEW OF ORGANIC THERMOELECTRIC MATERIAL TYPES

This thesis focuses on understanding and optimizing the thermoelectric properties of conjugated polymers with p-type dopants (further addressed in the next section). Nonetheless, research in OTE materials encompasses other materials, e. g., small molecules, organic-composites and organic-inorganic hybrids. Figure 2.1 and Table 2.1 show the chemical structures and a summary of the thermoelectric properties for representative materials used in OTE research.

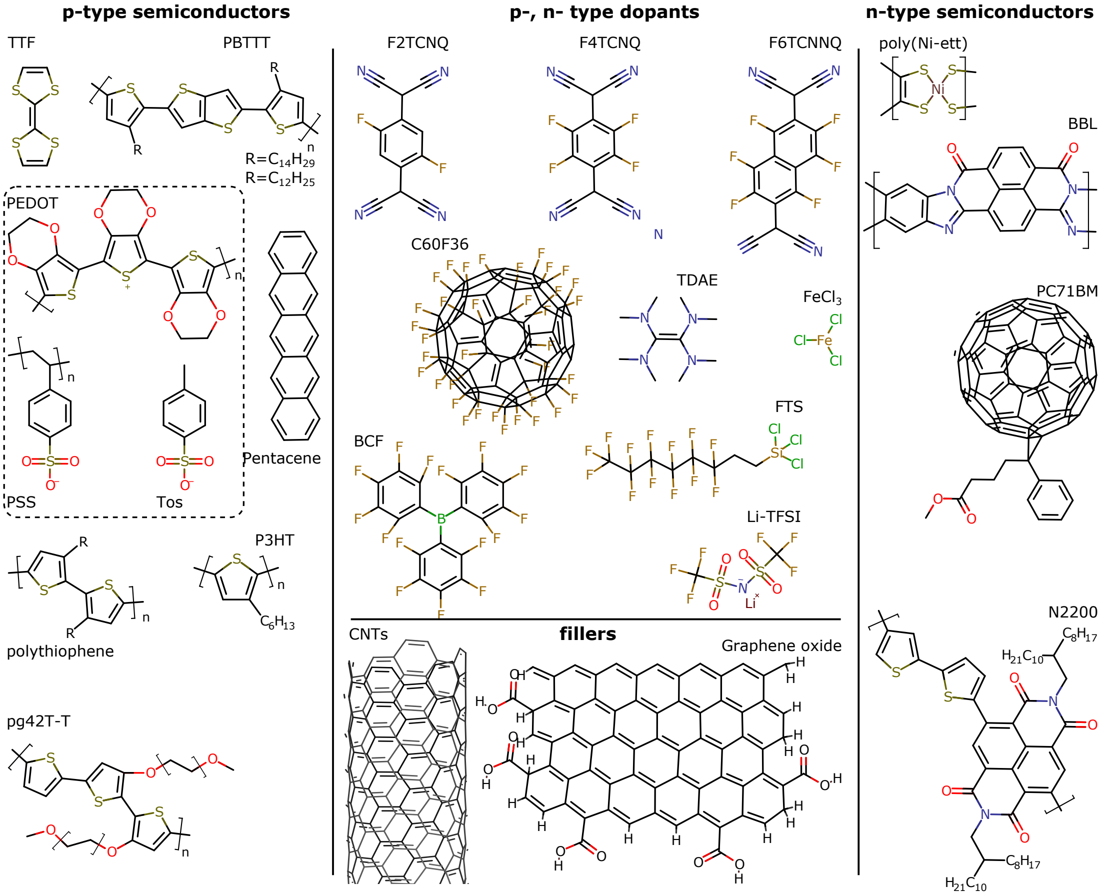

Figure 2.1: Chemical structures of representative p-, n-type conjugated materials, p-, n-type dopants and fillers. PEDOT is enclosed with two of its most common counter ions.

COMPOSITION/DOPANT	σ [$\mathrm{S\,cm^{-1}}$]	S [$\mathrm{\mu V\,K^{-1}}$]	σS^2 [$\mathrm{\mu W\,m^{-1}\,K^{-2}}$]	κ [$\mathrm{W\,m^{-1}\,K^{-1}}$]	ZT	REF
P-TYPE						
PEDOT:Tos/TDAE	80	200	320	0.37_z	0.25	[16]
PEDOT:PSS/DMSO	700	70	331	0.24_z	0.42_z	[17]
PEDOT:PSS/ Acid	1600	65	680	$\star 0.2 - 0.5_z$	0.75	[31]
PEDOT:Tos	422	25	26	1.81	0.005_z	[32]
PEDOT:PSS: CNT: PANI : GO	1900	120	2710	$\star$	$\star$	[33]
oriented-PBTTT/I_2	$2.2 \times 10^5 \parallel$	$9.4 \parallel$	1943	-	-	[34]
PBTTT/F4TCNQ	670	42	120	-	-	[35]
PBTTT/FTS	604	19	22	-	-	[36]
PBTTT/F4TCNQ→Li-TFSI	600	-	-	-	-	[37]
pg42T-TT/F4TCNQ	100	15	2.2	-	-	[29]
pentacene/F4TCNQ	0.43	200	2	-	-	[38]
oriented-RR-P3HT/$FeCl_3$	254	37	35	-	-	[34]
RR-P3HT/BCF	254	-	-	-	-	[39]
CNT/CPEs	500	46	105	$0.16_z - 1.2_{xy}$	-	[40]
RR-P3HT:TQ1/F4TCNQ	4	200	16	-	-	[41]
RR-P3HT:P3HTT/F4TCNQ	0.0002	600	0.01	-	-	[42]
N-TYPE						
N2200/N-DMBI	0.008	-850	0.58	-	-	[43]
N2200-derivative/N-DMBI	0.11	-200	0.46	-	-	[44]
p(gNDI-gT2)/N-DMBI	0.4	-100	0.4	-	-	[45]
BBL/TDAE	1	-60	0.43	-	-	[46]
CNT:PEDOT/TDAE	6	-1230	907	0.2 to 0.67	0.5	[47]
PTEG-x/N-DMBI	$1 - 12.9$	-200 to -750	•80	$0.069_z - 0.097_{xy}$	•0.34	[48]

Table 2.1: Thermoelectric properties of selected examples from literature. '-' Value was not measured. '$\star$' Value was not measured and authors used an estimated value. '•' Highest reported value for that particular reference. 'y' and 'xy' measurement in the out-of-plane and in-plane direction, respectively. '$\parallel$' measurement in the direction of the orientation.

2.2 CONJUGATED POLYMERS

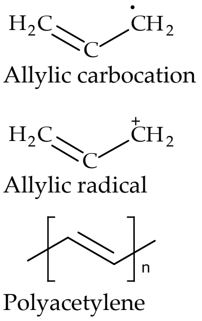

Figure 2.2: Representative examples of conjugated molecules.

Conjugated polymers (CPs) are organic macromolecules characterized by a backbone chain of alternating double- and single-bonds. What makes these materials interesting is the presence of π-electrons — delocalized over several nuclei, which can lead to different optical and electronic properties, e. g., electrical conduction in doped polyacetylene (Figure 2.2).

Ethylene, while not a conjugated polymer is a good example to understand bond formation. As seen in Figure 2.3a. the carbon-carbon double bond has a σ component and a π component. The σ component arises from the overlap of the (sp^2) molecular orbitals (MOs) along the internuclear axis. The π component is a result of the 2p orbitals having their axes perpendicular to the σ MOs and overlapping in a side-by-side manner. [49] The combination of the atomic orbitals (AOs) π_a and π_b generates two MOs that define the HOMO and lowest unoccupied molecular orbital (LUMO) (Figure 2.3b). The additive combination generates a bonding orbital (HOMO) that is lower in energy than the forming AOs, and the subtractive combination generates an antibonding orbital (LUMO), that is higher in energy. The bonding orbital is characterized by a region of high electron probability, whereas the antibonding orbital has a nodal plane where the probability of finding a π electron is zero, the more nodes an orbital has, the higher is its energy. [49]

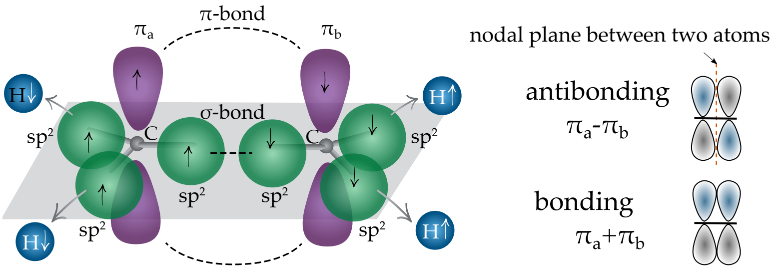

(a) Ethylene (b) MOs of ethylene

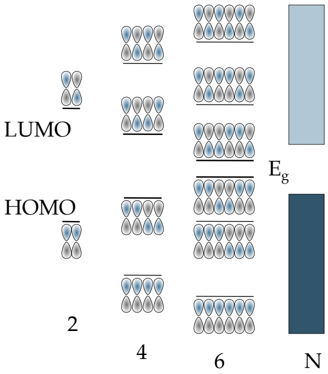

(c) MOs of polyenes

Figure 2.3: (a) Schematic illustration for the hybridization of ethylene. (b) Linear combination of the π orbitals on the carbons of ethylene. (c) band structure of N-conjugated subunits.

Increasing the conjugation length by adding consecutive π and σ bonds (Figure 2.3c) further splits the HOMO and LUMO levels. Until, for the case of a polymer, the MOs forms a tightly bound continuum of electronic states. The HOMO-LUMO differences is termed band gap (E_g), and ranges from 1.5 eV to 6 eV for most undoped conjugated polymers. [50] Experimentally, the HOMO and LUMO levels are measured using Cyclic Voltammetry (CV). Knowing these energy levels is essential to understand possible interactions with other molecules, for OTEs in particular, to choose an appropriate dopant.

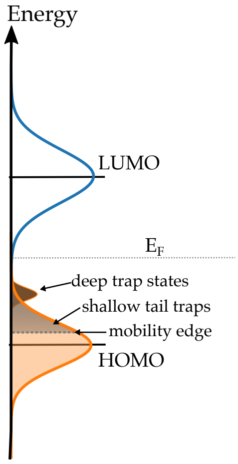

Figure 2.4: HOMO and LUMO energy levels of a large number of molecules represented as DOS having a Gaussian distribution.

DENSITY OF STATES Conjugated polymers exist in varying states of order, e. g., bends, folds and entanglements — which result in various local environments of distinct energies. [51, 52] Thus, the HOMO and LUMO levels of neighbouring polymer chains do not have exactly the same energy. Instead of sharp step-functions, a more realistic description of the energy landscape is that of a density of states (DOS) with a narrow Gaussian shape, [53] as seen in Figure 2.4. The electronic levels of organic materials are often given by their ionization energy (IE) (approximated by the HOMO) and electron affinity (EA) (approximated by the LUMO) and sitting in the middle the Fermi energy (E_F). [7]

TRAP STATES The existence of imperfections and impurities in the conjugated polymer gives rise to trap-states spatially distributed around the site of the imperfection, and energetically distributed towards its band gap. Depending on how energetically far they are from the bands edge, they are described as deep or shallow traps. Deep traps are approximated with a Gaussian distribution, while shallow traps are represented as a broad tail.

CHARGE CARRIER TRANSPORT charge transport in conjugated systems is given by thermally assisted hoping and is expected to be fastest along the conjugated backbone (intrachain Figure 2.5). Therefore, interchain ($\pi - \pi$ coupling) is said to dominate macroscopic charge transport in real polymeric systems as it is the slowest transport direction. [52, 54] Because organic semiconductors may comprise molecules of different sizes, and structural configurations, charge carriers need to hop between different backbones and boundaries.

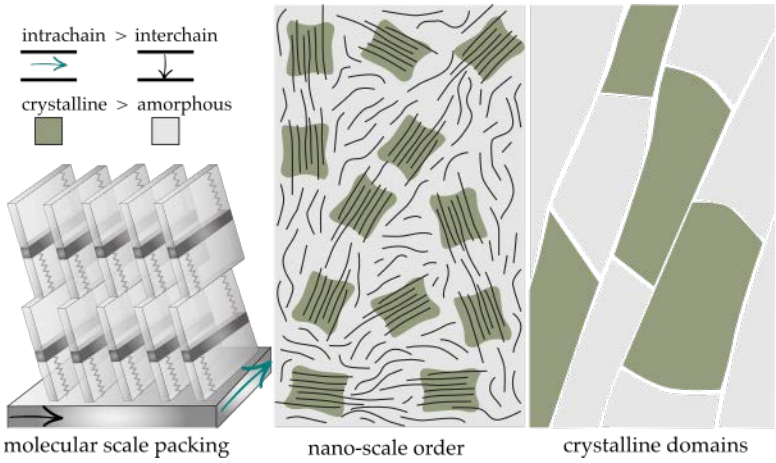

Figure 2.5: Schematic illustration of morphological features at different size scales.

The length scale of transport, is correlated to the degree of long-range structural order and overlap of the π-orbitals of nearby backbone chains — which has a strong interplay with processing and the organic semiconductor's intrinsic properties e. g., molecular weight, chemical structure, rigidity, and the presence of side-chains. [52] Also relevant, different processes can occur at each length scale.[55] For instance: Molecular packing and chemistry-related features (1 Å to 3 nm) can modify the energy levels (DOS) [53] and charge transfer mechanisms. [56] Simultaneously, the crystalline order, defects, and interface boundaries (0.5 nm to 10 nm) will influence charge trap formation and the macroscopic charge percolation path. [53]

PARACRYSTALLINITY Paracrystalline disorder is the static fluctuation of local lattice disorder spacing [57] and is described by the parameter g. Experimentally X-ray diffraction peak-shape analysis can be used to measure g, using the peak center position and breadth (Δ_q) of the diffraction peak (q_0) following Equation 2.1, where a higher g value indicates more disorder. [53, 57, 58]

$$g = \sqrt{\frac{\Delta_q}{2\pi q_0}} \tag{2.1}$$

There is a strong correlation between paracrystallinity and charge transport. In brief, paracrystalline disorder in the interchain direction induces a tail of localized states extending into the materials' E_g that act as shallow traps [57] and limit charge transport. In essence, a higher g value broadens the DOS of the organic semiconductor.[53, 54] Disorder in the π stacks is considered most relevant given that this direction is said to dominate macroscopic charge transport. [52, 53, 57] Research by Noriega et al. demonstrated that g_π for many high-mobility high-weight polymers lies between 10 % to 20 % with the exception being PBTTT which shows an exceptional level of order (around 7 %).

ANISOTROPIES In solution-processed films, the polymer chains tend to lie along the substrate with the π-conjugated plane of the backbone either in an edge-on or face-on configuration. Techniques that yield high degree of long-range order and orientation (e. g., rubbing and stretching [34, 35] create significant opportunities to understand the influence of grain boundaries and crystallite orientation on the charge mobility. For instance, in poly(3-hexylthiophene-2,5-diyl) (P3HT) and PBTTT, the anisotropy in mobility of carriers along the chain direction relative to the $\pi - \pi$ stacking is about 5 to 6.[52] Nonetheless, values as high as 20 have been observed when carriers had to cross boundaries between edge-on and face-on crystallites for P3HT. While this creates unique opportunity to enhance the electrical conductivity, the effect of anisotropy on the S is less understood. [59]

2.3 PARAMETERS THAT GOVERN THE ZT

2.3.1 *Electrical conductivity*

The electrical conductivity increases with carrier concentration n_i and carrier mobility μ_i following Equation 2.2

$$\sigma = q_i n_i \mu_i \tag{2.2}$$

where q_i is the electric charge of either holes or electrons i. For most relevant applications, n_i must be increased via electrical doping, which we will discuss further in the following sections. For inorganic semiconductors, an increment in n_i typically leads to a linear or sublinear increase of σ due to impurity scattering. [60] Alternatively, organic semiconductors show a *different* trend, i. e., a sublinear increase in σ and a superlinear increase in μ_i at low n_i which then saturates for higher values, as seen in Figure 2.6. [60, 61]

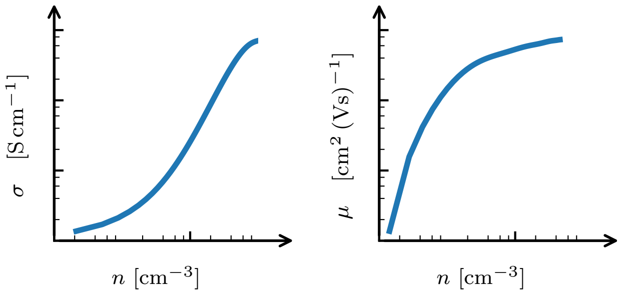

Figure 2.6: Trends often for σ and μ_i as a function of carrier concentration.

These trends are often associated to a filling of Coulomb traps caused by ionized dopants, as well as traps due to impurities, defects, and structural and energetic disorder.

Conduction in lightly doped organic semiconductors occurs through a thermally assisted hopping process, often described with an Arrhenius equation of the form $\sigma(T) \propto \exp(-E_a/K_B T)$, where E_a is an activation energy and K_B the Boltzmann constant. Alternatively, Kang et al. proposed a model that describes carrier mobility for disordered semiconducting polymers following Equation 2.3.

$$\sigma_{\mathrm{Eo}} \propto \exp\left[-\left(\frac{W_\gamma}{k_B T}\right)^{\gamma}\right] \tag{2.3}$$

Here, σ_{Eo} is thought of as an effective carrier mobility that relates to the polymer morphology W and its connectivity γ. In this model, W acts as an activation energy while γ is said to capture the dimensionality of the system. [62] Noteworthy, there are many other relevant models that are not discussed here. From Equation 2.3 and Equation 2.2 we can expect that an increase carrier concentration (q_i) or carrier mobility $\mu_i(\sigma_{\mathrm{Eo}})$ will lead to an improvement in σ. Increasing n_i is covered by doping, while μ_i is related to the connectivity and size of the percolating network between conductive grains across a non-conducting (or less-conducting) background. Consequently, processing methods that lead to enhanced structural order, long-range connectivity and orientation will improve μ_i and thereby σ, e. g., stretching of polyacetylene (PAc) [63] or the orientation of P3HT via small molecule epitaxy. [64]

the role of doping on n and σ is further detailed in Section 3.1

For the reference material PBTTT, there is a relatively good understanding of how carrier mobility increases with structural order. [55, 65–67] Delongchamp et al. observed that a thermal annealing cycle (from 25 °C to 180 °C) induces a high level of order in the $\pi - \pi$ stacking and backbone direction, and leads to an improved carrier mobility (from $0.11\,\mathrm{cm^2\,V^{-1}\,s^{-1}}$ to $0.40\,\mathrm{cm^2\,V^{-1}\,s^{-1}}$ in field-effect transistors (FETs)). [65] Subsequent experiments using shear deposition techniques and then temperature annealing, induced µm-length ordered domains of PBTTT backbones, without requiring a more complex technique. [67, 68] The versatility of this material made it attractive as a test-bed for understanding charge transport in organic semiconductors[54, 62] and to explore how improved structural order and orientation can benefit OTEs.

In a representative example, Hamidi-Sakr et al. fabricated highly oriented samples via mechanical rubbing. In brief, films of RR-P3HT were rubbed at temperatures between 100 °C to 180 °C and then doped using F4TCNQ through an orthogonal solvent. The resulting films presented high optical and electrical anisotropy ($2.5\,\mathrm{S\,cm^{-1}}\perp$ and $22\,\mathrm{S\,cm^{-1}}\parallel$). [59, 69] In other example, Patel et al. demonstrated that spin coating PBTTT onto trichloro(octadecyl)silane (OTS)-functionalized substrates leads to a large orientational correlation length (OCL) (length scale of aligned backbones). [35] Through resonant soft x-ray scattering (RSoXS), they were able to correlate the how OCL impacts σ, as seen in Figure 2.7.

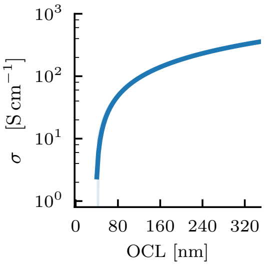

Figure 2.7: Electrical conductivity as a function of OCL

2.3.2 *Thermal conductivity*

The total thermal conductivity of a material is composed of a contribution that is due to the lattice κ_{latt}, and one that is due to the charges κ_{e}, following Equation 2.4. [70]

$$\kappa_{total} = \kappa_{\mathrm{e}} + \kappa_{\mathrm{latt}} \tag{2.4}$$

For undoped amorphous and isotropic conjugated polymers, the lattice contribution is generally low (≈$0.3\,\mathrm{W\,m^{-1}\,K^{-1}}$), primarily due to the weak van der Waals interactions between polymer chains, and inherently anisotropic (fastest along the polymer chain). [7, 35] Up o a great extent, it is possible to argue that the thermal conductivity is one of the appealing points of using organic semiconductors for thermoelectrics. Alternatively, in metals and inorganic materials with high electrical conductivity, κ_{e} is typically the dominant contribution ($\kappa_{\mathrm{e}} >> \kappa_{\mathrm{latt}}$) and follows the Wiedemann-Franz law given by Equation 2.5.

$$\kappa_e = \sigma L_0 T \tag{2.5}$$

where L_0 is the Lorenz number and typically close to Sommerfeld value of $2.44 \times 10^{-8}\,\mathrm{W\,\Omega\,K^{-2}}$. [71–73] Thus, κ_{e} is small for σ values below $10^1\,\mathrm{S\,cm^{-1}}$ but increases rapidly as σ increases, as seen in Figure 2.8.

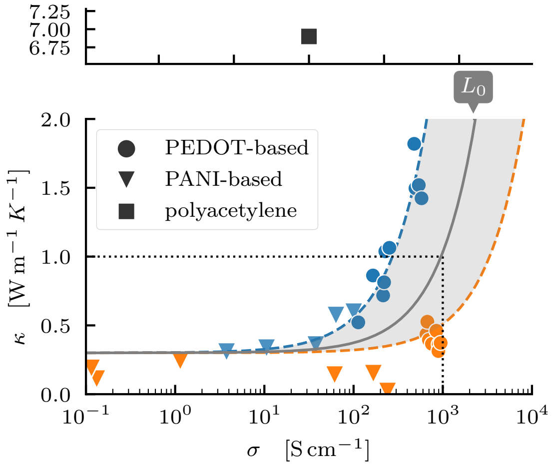

Figure 2.8: Electronic contribution to the thermal conductivity following Equation 2.4 and Equation 2.5. Values used are a $\kappa_{\mathrm{latt}} = 0.35\,\mathrm{W\,m^{-1}\,K^{-1}}$ and different Lorenz values, that is $\mathrm{L_0}$, $\mathrm{L_0} \times 3.5$ and $\mathrm{L_0}/3.5$. Circles represent data for PEDOT:Tos ● and for PEDOT:PSS ● extracted from references [17, 32]. Also included PAc from references [14, 74] and PANI from reference [75]

Whether doped conjugated polymers follow Equation 2.5 or if the values of L vary for distinct materials is still unclear and a controversial topic. [7, 32, 71] As seen from Table 2.1, the experimental data of κ for OTE materials is very limited and the reported values often vary significantly even for relatively similar compositions. For example, some experimental studies suggest an $L < L_0$ for PEDOT:PSS and $L > L_0$ for PEDOT:tosylate (Tos). Similarly, polyaniline (PANI) doped with distinct dopants also show trends above and below L_0, whereas doped PAc shows a thermal conductivity that is much higher, as seen in Figure 2.8. [17, 32, 76] Therefore, it is not clear if the size of the dopant, chemical structure of the CPs or the structural order has a role in the resulting behavior of κ_e. A recent work by Scheunemann and Kemerink indicates that such deviations are related to the degree of energetic and structural disorder in the polymer film, [71] and indicate that routes to tailor L, will be necessary for reaching a high ZT when reaching high values of σ. [71]

Previous observations indicate that thermal transport in doped conjugated polymers is not fully understood and highlights the necessity of a self-consistent methodology for measuring the same sample with different doping levels and for a significant number of samples. The latter is not trivial, as one can incur in batch-to-batch variations. Also, there can be incompatible sample geometry, holder, or electrode positioning between the methods used for characterizing σ and κ.

In Chapter 6 we explore a methodology to measure κ in a large number of samples, allowing us to stretch our current knowledge of the interplay between κ, microstructure and σ.

Another issue related to the characterization of κ is being able to measure in the same direction as σ. For most cases, the reported κ corresponds to the out-of plane thermal conductivity (κ_z) while the ZT is calculated using σ_{xy}. The latter is due to the difficulty in measuring κ_{xy} in a thin film or being able to fabricate a thick doped film with the same characteristics as the thin film. [7] As mentioned earlier, polymeric materials can possess significant anisotropy, and thus the resulting ZT can be overestimated or underestimated. For instance, anisotropic thermal conductivity has been observed in PEDOT:PSS, where κ_{xy} was up to 5 times larger than κ_z. [76, 77] Alternatively, the reported thermal anisotropy for PEDOT:PSS processed with DMSO is lower ($\kappa_z \approx 1.6\kappa_z$).

2.3.3 *Seebeck coefficient*

The magnitude of the Seebeck coefficient is defined as the voltage divided by the applied temperature gradient, $S = -\Delta V/\Delta T$. According to the work by Fritzsche, the Seebeck coefficient of semiconductors can be calculated from Equation 2.6 [78]

$$S = \frac{k_\mathrm{B}}{e} \int \frac{E - E_F}{k_\mathrm{B} T} \left(\frac{\sigma(E)}{\sigma} \right) dE \tag{2.6}$$

where k_B/e is the natural unit of the Seebeck coefficient $86.17\,\mu\mathrm{V\,K^{-1}}$, and $\sigma(E)$ is the conductivity distribution function that is related to the measurable device conductivity following Equation 2.7.

$$\sigma = \int \sigma(E)\mathrm{dE} \tag{2.7}$$

The sign of S depends on whether conduction occurs above or below E_F and can be understood as the entropy per unit charge, weighed by the contribution of that charge to the total conductivity. [78] According to the work by Zuo, Abdalla, and Kemerink assuming that $\sigma(E)$ is narrowly centered around the transport energy (E_{tr}), Equation 2.6 can be further simplified to Equation 2.8. [79]

$$S \cong \frac{E_F - E_{tr}}{T} \tag{2.8}$$

In this context, the magnitude of S and σ are said to depend in a characteristic hopping event between the E_F and the E_{tr} at a given temperature T, which can simply be expressed with the following Equation 2.3.3

$$S \propto \frac{E_F - E_{tr}}{T} \quad \text{and} \quad \sigma \propto \exp\left(\frac{E_F - E_{tr}}{T}\right) \tag{2.9}$$

[79] where E_F is dependent on the shape of the DOS and the carrier concentration (thus in the doping level), while E_{tr} depends in the part of DOS that facilitates charge transport. [79, 80]

The strong correlation between S and σ means that an increase in one parameter leads to a decrease in the other one. In this regard, tuning the E_F via doping, and the shape of the DOS via nanostructuring, has been proposed as a possible alternative to improve both properties.[7, 42, 53, 79, 81]

Chapter 7, we revisit the concept of DOS as an inspiration for using polymer-polymer blends to improve simultaneously S and σ.

DOS ENGINEERING In a particularly good example, Sun et al. fabricated films of RR-P3HT(A) mixed with varying fractionspoly(3-hexylthiothiophene) (P3HTT)(B) and doped with F4TCNQ.[42] With a composition almost exclusively A or B the thermoelectric properties resemble that of the pure fraction. However, with 8 % of P3HTT, E_{tr} shifts towards the P3HTT fraction while E_F remains in the dominant percolating network (i. e., P3HT). The resulting S is significantly higher than that of the pure fractions while also showing a simultaneous increase in σ. Moving too far from A, means that transport occurs only in the B fraction, which interacts poorly with the dopant and thus leads to a lower σ. The main conclusion was that S increased as grater proportions of σ occur farther from the E_F. While the improvement in σ was very low, this approach inspired Zuo et al. to further explore this proof of concept on a wider set of polymer-polymer blends (further detailed in Chapter 7). [41, 82]

A distinct approach is narrowing the DOS to increase the asymmetry about the E_F and E_{tr}. Experimental work by Venkateshvaran et al. demonstrated that disorder induced by the sidechains in polymers like PBTTT and N2200 significantly broadens the DOS. Using field effect measurements, they were able to measure a relatively high S for polymers with a low energetic disorder. [83] More recent findings by Abutaha et al. also found that the width of the DOS tail, broadens exponentially with paracrystallinity, further highlighting the importance of microstructure control for improving S. [54]

ENERGY FILTERING Another interesting approach is the so-called energy filtering. The goal here is to scatter low-energy carriers while allowing high-energy carriers to pass. The total number of charge carriers diminishes sigma, but since the ZT scales as S^2, a net increase in performance is possible. [84] In practice, most efforts employ interface engineering by combining materials with transport bands slightly mismatched in energy.[85] However there is no definite demonstration of this effect and the concept has only been suggested to explain certain examples. [86]

PARAMETER OPTIMIZATION Previous subsections demonstrate that improving the ZT is a far from trivial task. The parameters σ, κ and S depend on carrier concentration and are strongly correlated, such that, increasing one parameter may have a detrimental effect on the other, as seen in Figure 2.9. Instead, research in OTE is often focused on finding an optimal point where either the ZT or the $S^2\sigma$ are maximized.

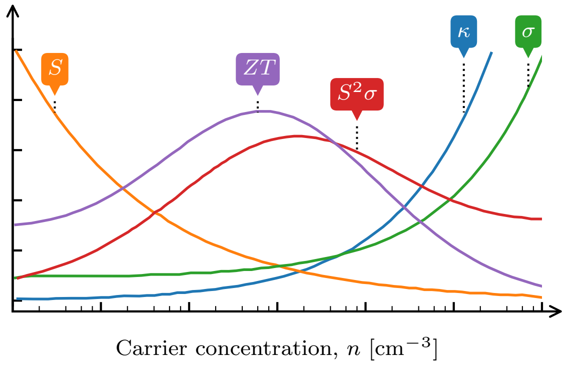

Figure 2.9: Dependence of the parameters that govern the ZT with carrier concentration.

2.4 UNIVERSAL POWER LAW

As the carrier concentration is not always known or difficult to measure, plotting S as a function of σ allows to perform a meaningful analysis of the trends followed by a particular family of materials. Doing so, Rowe and Min proposed an $S - ln\sigma$ plot as an indicator of thermoelectric performance for a series of inorganic-based TEs. [87] In a subsequent work, Kaiser made a similar approach by compiling numerous data on doped PAc and plotting S and σ in a double logarithmic scale. [88, 89] More recently, Glaudell et al. compiled data for a wide range of p-type materials (as seen in Figure 2.10) and proposed that they follow a universal trend given by Equation 2.10.

$$S = \frac{k_B}{e}\left(\frac{\sigma}{\sigma_{E0}}\right)^{-1/4} \tag{2.10}$$

where k_B/e is the natural unit of the thermopower and σ_{E0} is a fitting constant [36] The power factor follows the relation $S^2\sigma \propto \sigma^{1/2}$ which illustrates that the highest $S^2\sigma$ is achieved for the highest values of σ. This trend was found to hold also for n-type OTEs materials [90], while oriented samples like PBTTT require a different σ_{E0} fitting factor.

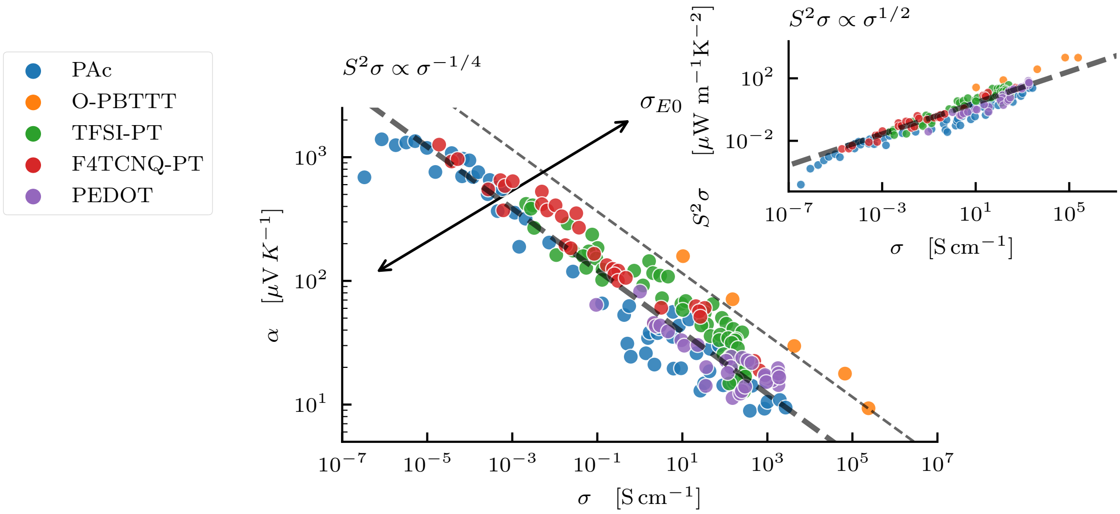

Figure 2.10: Seebeck coefficient and power factor plotted as a function of the electrical conductivity. Dashed lines represent $S \propto \sigma^{-1/4}$ and $S^2\sigma \propto \sigma^{1/2}$. Data compiled from references [12, 34, 36, 88, 89] PT represents various polythiophenes and O-PBTTT represents oriented PBTTT.

More recently, physical explanations have been to the power law. Kang et al. formulated a transport-edge model as $S \propto \sigma^{-1/s}$ and proposed that s=3 adjusts better for polymers like P3HT and PBTTT, and s=1 for materials like PEDOT:Tos. [62] Here, the authors relate s to the type of transport model and σ_{E0} to a temperature-dependent transport coefficient related to the film morphology following Equation 2.3. [62, 80] Alternatively, Abdallah et al. formulated a hopping model with a doping-affected DOS. [80, 91] Noteworthy, both models can reproduce the empirical power law represented in Figure 2.10.

3

DOPING OF CONJUGATED POLYMERS

This chapter introduces the mechanisms involved in the electrical doping of conjugated polymers, the different doping processing techniques, as well as current challenges related to stability, processing and efficiency.

3.1 DOPANTS CLASSIFICATION

The electrical conductivity of most undoped CPs lies between $10^{-8}\,\mathrm{S\,cm^{-1}}$ to $10^{-5}\,\mathrm{S\,cm^{-1}}$.[92] However, a higher electrical conductivity is needed for the development of many advanced optoelectronic and energy applications, such as light-emitting diodes, solar cells, and thermoelectrics. This is, indeed so relevant, that the discovery that conjugated polymers could be doped until they show electrical conductivities more familiar to metals led to the Nobel Prize in Chemistry in 2000 and granted to Alan Heeger, Alan MacDiarmid and Hideki Shirakawa. [63, 93, 94]. Electrical doping introduces charge carriers, n_i by forming a chemically stable material upon the addition or removal of an electron. [7, 95] Consequently it is a powerful technique to adjust the electrical conductivity and tailor the electronic properties for a specific demand. Due to the large variety of organic molecules with different properties, countless materials can have a doping effect in CPs. We briefly describe some of them classified as i. e., Redox dopants, acids/bases (H^+/H^-) and Lewis acids/bases.

REDOX DOPING Electron acceptors acting as an oxidizing agent are referred to as p-typed dopants. They remove one electron from the HOMO of the conjugated polymer and generate an ionic complex comprised of a positively charged (hole) in the polymer and a corresponding counter anion of the utilized dopant. Some of the most well-known p-type dopants in OTE research are F4TCNQ and iron(iii) chloride ($FeCl_3$). Alternatively, n-type dopants donate one electron to the LUMO of the conjugated polymer, generating a negatively charged polymer and a counter cation of the corresponding dopant. Some examples of n-type dopants are Na^+ and K^+.

ACID/BASE DOPING This type of doping process is a Brønsted acid-base reaction and consists in the transfer of a proton H^+ (for p-type) or a hydride H^- (for n-type) using materials like HCl, HBr (for p-type) and N-DMBI for n-type doping. Here, the charge neutrality is maintained by the reacted dopant molecule acting as counter-ion for the charge on the semiconductor. For p-type doping, representative examples include PANI protonated with camphorsulfonic acid (CSA), and tridecafluoro-1,1,2,2,-tetrahydrooctyl)-trichlorosilane (FTS)-doped P3HT and PBTTT. Representative n-type dopants include Poly[N,N′-bis(2-octyldodecyl)-naphthalene-1,4,5,8-bis(dicarboximide)-2,6-diyl]-alt-5,5′-(2,2′-bithioph-ene) (N2200) [43] doped with N-DMBI. Other polymers doped using the same dopant and their thermoelectric properties are depicted in Table 2.1.

LEWIS ACID-BASE This type of doping is suitable for conjugated polymers with heteroatom-containing lone electron pairs. Some examples of this type of dopants are BF_3, $AlCl_3$ and BCF. Traditionally, this doping process was explained in terms of a Lewis acid-base adduct between the dopant (Lewis acid) and the lone pairs of a heteroatom (Lewis base), and followed by a redistribution of the electron density. [39] However the details of free charge carrier formation was largely unknown. Only recently, Yurash et al. proposed a distinct mechanism based on results from nuclear magnetic resonance (NMR) and density functional theory (DFT) experiments of different Lewis acids and proposed the following: First, formation of a Brønsted BCF$-H_2O$ complex. Second, the complex protonates the weak Lewis acid base of the CP generating the species [polymer-H]$^+$ and a counter ion of [BCF$-$OH]$^-$. Third, an electron transfers from a neutral polymer segment to [polymer-H]$^+$, generating the species [polymerH]$^{\bullet+}$, [polymerH]$^\bullet$ and [BCF$-$OH]$^-$. [96, 97] Key findings from this work was that Lewis acid-base adducts in fact, inhibit the doping process and that trace levels of water are essential for the process. Figure 3.1 illustrates this process for the case of doping with tris(pentafluorophenyl)borane (BCF).

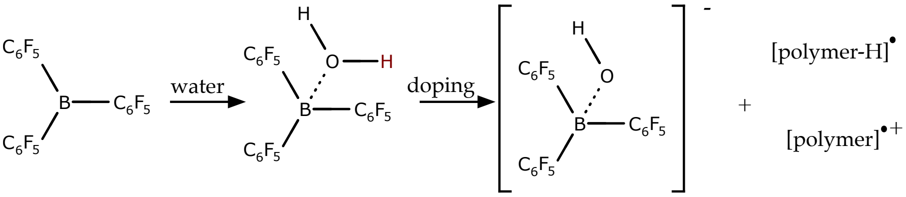

Figure 3.1: Doping process depicted for BCF.

3.2 POLARON AND BIPOLARON FORMATION

The addition or removal of an electron leads to a localized charge on the chain coupled to local lattice distortion. The sum of these effects is referred to as a polaron and is the manifestation of a strong electron-phonon coupling.[98] A bipolaron is formed after removing a second electron from the conjugated polymer, and thus is defined as a pair of charges associated to a strong lattice distortion in the conjugated polymer (see Figure 3.2 left). To date, there are two theories that interpret polaron band theory. A traditional model introduced by Bredas and Street and which has been used extensively to describe polaron formation [99]. And a revised model, proposed by Zozoulenko et al. and then by Png et al. which employs modern DFT calculations to further understand experimental observations.[100, 101]

STANDARD MODEL A distinctive feature of the pre-DFT band structure models is the appearance of a pair of spin-degenerate levels that lie inside the $\pi - \pi^\star$ gap. The polaron level is occupied by one electron, whereas the bipolaron levels are empty (see Figure 3.2 center).

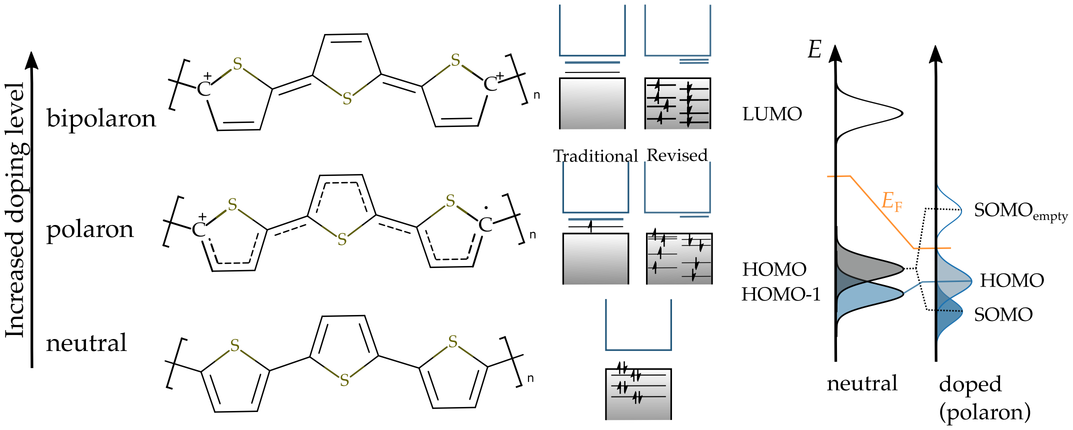

Figure 3.2: Chemical structures of a neutral polythiophene, one carrying a polaron and one a bipolaron. Also, DOS model of a p-doped material in the polaron state.

REVISED MODEL For p-type doping, polaron formation causes the HOMO to split into a singly-occupied molecular orbital (SOMO) and an empty SOMO$_e$. The SOMO shifts below the HOMO-1, which becomes the new HOMO$_n$, with the empty SOMO$_e$ both of them flanking the E_F, as seen in Figure 3.2. The remaining unpaired electron lies energetically below the valence band edge, which is consistent with the prevailing observation that the IE of p-doped semiconductors increases compared to the neat film. This process repeats for long chains, producing multiple polarons until reaching the onset of bipolaron formation. [95, 100, 101]

3.3 DOPING EFFICIENCY

The doping efficiency describes the fraction of generated carriers per dopant molecule added into the host material. Such a process occurs in two steps; (i) the formation of a polaron bound to a counterion, (ii) followed by the dissociation of said polaron to account as a free charge carrier. The doping efficiency can then be described by the product of the polaron formation (η_{pf}) and the dissociation efficiency (η_{diss}) following Equation 3.1

$$\eta = \eta_{\mathrm{pf}} \times \eta_{\mathrm{diss}} = \frac{N_{\mathrm{free}}}{N_{\mathrm{dopant}}} \tag{3.1}$$

OBSTACLES FOR HIGH DOPING EFFICIENCY Several factors can hinder a high doping efficiency, for instance, redox doping is characterized by the formation of intermediate charge transfer states before generating free carriers.[102] In this regard the neutral dopant can interact with the organic semiconductors via two mechanisms, integer charge transfer (ICT) formation or fractional charge transfer (FCT) formation. [95]

INTEGER CHARGE TRANSFER This process is characterized by the formation of an ion pair (IPA) that readily dissociates at room temperature. [102] p-type doping occurs if the LUMO of the dopant is deeper than the HOMO of the organic semiconductor, commonly referred to as 'host', as seen in Figure 3.3. In this case, an electron is transferred from the host to the p-type dopant, leading to the formation of an IPA, i. e., a radical anion in the dopant, a cation in the polymer host, and a downward shift of the E_F. [61, 95] For n-type doping, if the LUMO of the host is deeper than the HOMO of the dopant, then an electron is transferred from the dopant to the host. Host:dopant systems that follow the ICT mechanism are thought to have a dissociation efficiency of $\eta_{diss} = 100\%$. Nonetheless the amount of carriers that eventually contribute to σ may be less due to the presence of traps. [60]

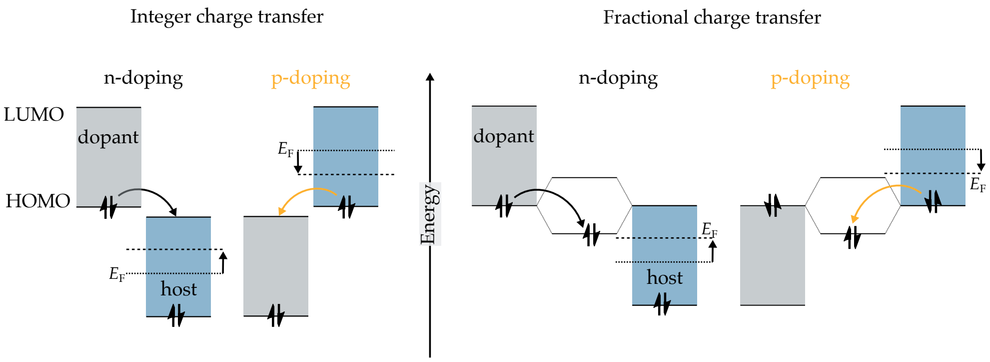

Figure 3.3: Schematic illustration of the ICT or FCT mechanisms. Illustration shows the migration of electrons after using p- and n-type dopants, as well as the shift of the E_F for each case.

FRACTIONAL CHARGE TRANSFER This process is characterized by the formation of a neutral charge transfer complex (CTC) that does not immediately contribute as a carrier. In essence, the frontier orbitals of the dopant and the host hybridize to form a new HOMO and LUMO. The CTC can then take the role of the dopant to donate or withdraw electrons from the host, *only* if the energy levels fulfill the conditions described in the ICT process, albeit less efficient given the extra step required.[61]

Even though FCT formation has been reported for a fair amount of conjugated small organic semiconductors [56, 95, 103], it is not a common doping route for CPs, which appear to proceed dominantly through ICT. For the benchmark material RR-P3HT, doping with the p-type dopant F4TCNQ usually proceeds via ICT, [104–106] while interestingly, the oligomer quarterthiophene (4T) proceeds via CTC. The latter was surprising, given the fact that the energy levels and chemical structures between 4T, and RR-P3HT are relatively similar. Méndez et al. ascribed these observations to differences in the crystalline structure between these two materials.[107] Only recently, Jacobs et al. demonstrated further that the crystalline structure plays a significant role on whether doping proceeds through CTC or ICT. By fabricating films of RR-P3HT:F4TCNQ using specific deposition conditions, they were able to obtain a polymorph that exhibited only CTCs.

Also recently, Neelamraju et al. demonstrated that different charge transfer states can coexist in films of F4TCNQ-doped films of RR-P3HT and regiorandom poly(3-hexylthiophene) (RRa-P3HT). They suggested that for high doping levels CTC is favored once the easier-to-oxidize DOS are saturated. In conclusion, the authors were able to identify that the dopant content, microstructure and energetic local environment defined the charge transfer mechanism.[109]

Additional work by Thomas et al. suggests that interaction between the π-faces of the dopant and the polymer plays a significant role in determining the charge transfer mechanism. They observed that F4TCNQ-doped films of RR-P3HT and poly(3-(2′-ethyl)hexylthiophene) (P3EHT) proceed through ICT and CTC, respectively. They ascribed the differences to F4TCNQ being forced to allocate between the π-faces of the P3EHT crystallite, due to the steric hindrance imposed by the branched sidechains (cf. chemical structure of P3HT and P3EHT in Figure 3.4). Their results were quite surprising as both polymers have similar chemical structures and energy levels. [110]

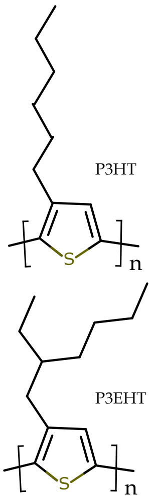

Figure 3.4: Chemical structures of P3HT and P3EHT

A shared view from previous publications was that CTC formation is a barrier to efficient doping in organic semiconductors and highlighted that the conditions leading to a particular doping mechanism are not fully understood. Whether CTCs is entirely detrimental for OTE applications had not been investigated. We, therefore, address this topic in Chapter 5.

3.3.1 *Improving doping efficiency*

DOUBLE DOPING More recently, Kiefer et al. demonstrated that proper selection of the energy levels can lead to the formation of dopant dianions and efficiencies of up to $\eta = 170\%$. Here, each dopant is able to participate in two doping events, significantly reducing the amount of dopant required to increase σ. [29] Moreover, they found dianion formation to occur in four distinct p-dopants suggesting the process could be extended to different host:dopant systems.

SHIELDING Aubry et al. reached near $\eta = 100\%$ when doping RR-P3HT using boron clusters. A comparison between F4TCNQ- and boron-doped RR-P3HT, reveled that identical equimolar dopant concentrations lead to distinct carrier densities i. e., $4.3 \times 10^{20}\,\text{cm}^{-1}$ and $7.9 \times 10^{20}\,\text{cm}^{-1}$ for F4TCNQ and the boron cluster, respectively. They ascribed their results to efficiently shielding formed polarons from the counterions, thus reducing Coulombinc interactions with the anion. [111]

MISCIBILITY Kroon et al. demonstrated that tailoring polar sidechians into CPs enhanced the compatibility between the polymer and p-dopants like F4TCNQ. Using this approach they achieved near $\eta = 100\%$ efficiencies. [27] Kiefer et al. then extended this concept for a naphthalenediimide -bithiophene copolymer doped with the n-dopant N-DMBI, resulting in efficiencies of up to $\eta = 13\%$. The latter was a significant improvement taking into account that typical doping efficiencies for n-dopants are lower. [45]

ANION EXCHANGE Only recently, Yamashita et al. explored an anion exchange technique that is not limited to the redox potential limitations. Here, F4TCNQ-doped PBTTT is immersed into an orthogonal solution of bis(trifluoromethane)sulfonimide lithium salt (Li-TFSI) which prompts an instantaneous exchange with TFSI^- anions. [37] Employing UV-Vis-Nir spectroscopy, they observed a complete quenching of the bands corresponding to the neutral polymer, indicating a very high doping level. More recently, the same approach was extended to other semicrystalline polymers and revealed that this method is suitable for achieving very high doping levels, and that at such levels, the rapping effect by ions is negligible. [112]

3.4 STABILITY OF THE DOPED STATE

Ideal power-generators should have a long operating lifetime, or, in other words, be able to keep a near 'as-new' performance as they age. In reality, this is very hard to accomplish: the doped species in the OTE material responsible for enhancing σ may return to their neutral state, the dopant may diffuse out of the material, interact with the environment, or degrade due to thermal oxidation. Thus, the doped state's stability is directly related to the thermoelectric performance stability and realization of commercially successful OTE devices. Consequently, the material's chemical and thermal stability will determine the operating range/conditions of the OTE material and the final application.

CHEMICAL STABILITY The material's energy levels largely determine the chemical stability. For example, a shallow LUMO can lead to undesired reactions with water and oxygen. In n-type OTEs, the HOMO(LUMO) levels tend to lie above the reduction potential of oxygen(water), which poses a challenge for prolonged and unencapsulated applications. [7, 30, 51] Due to the latter, there are markedly more known air-stable p-type than n-type OTE materials, and research on the n-type OTE materials has lagged compared to p-type materials. A straightforward approach is employing barrier layers (e. g., glass, resins, or polymers) provided that they do not compromise other aspects (e. g., weight and flexibility). [91] A distinct approach is the chemical design and relies on the appropriate selection of chemical moieties to adjust the energy levels. [30, 51] Alternatively, new classes of stable n-dopants are emerging based hydride transfer like N-DMBI and triaminomethane (TAM). Only recently, Yang et al. used a computer-assisted screening approach to design a TAM derivative. The best candidate was synthesized and used to dope two polymers, which featured nearly unchanged thermoelectric properties for up to a 16 h under air exposure. [113] In a different example, Paterson et al. presented films of an air and water stable NDI-bithiophene copolymer doped with the Lewis salt tetra-n-butylammonium fluoride salt (TBAF). [30]

THERMAL STABILITY The size, chemical, and physical interactions between the conjugated material and the dopant largely determine the thermal stability. For instance I_2-doped RR-P3HT readily dedopes out of the film at room temperature, while blends of F4TCNQ-doped RR-P3HT begins to dedope at temperatures above 90 °C [114] over a relatively short period of time. One approach is improving the compatibility between the dopant and the polymer. For example, tailoring polar side chains in NDI, polythiophene, and fullerene derivatives has provided satisfactory results when using dopants like F4TCNQ and N-DMBI. [27, 45, 48] Through this approach, Kroon et al. presented a polythiophene derivative doped with F4TCNQ that when exposed to a temperature ramp of $\approx 10\,°\mathrm{C\,s^{-1}}$ featured an almost constant electrical conductivity up to 150 °C. [27] Using bulkier dopants is also possible. Liu et al. presented films of a conjugated small molecule (CSM) doped with a fullerene derivative, which showed that thermal annealing at temperatures up to 200 °C promoted mixing between the fullerene and the host instead of diffusion out of the polymer layer. [76] However, bulkier dopants might disrupt the crystalline structure and require complex deposition techniques. A novel approach by Xu et al. employed all-polymer donor-acceptor heterojunctions. Instead of a highly diffusive molecular dopant, they mixed two semiconducting polymers. In this case, both materials generated mobile charge carriers and thus, the amount of non-conducting material in the film was limited. S varied depending on the composition ratio, and the electrical conductivity decreased by less than one order of magnitude after 20 h at 200 °C. The repercussions of this concept are significant: as this approach offers the possibility of a "one-pot" OTE generator containing both the n- and p-type materials, and that is less likely to suffer phase segregation and morphology perturbation after deposition. [26].

From this section, one can observe two main routes towards optimizing the thermoelectric stability:

1. Selecting a known dopant (or host) that performs relatively well and then modifying fragments from its chemical structure to improve dopant-host compatibility or lower its tendency to react with the environment.

2. Permutation of known dopants and hosts to find a better match.

However, there is evidence that changes in morphology alone can lead to differences in thermal and ambient stability. Jacobs et al. presented a case in which F4TCNQ-doped RR-P3HT can proceed through either ICT or FCT depending on film deposition temperature. Wide-angle X-ray diffraction (GIXD) revealed that films doped through FCT displayed an unusually dense and well-ordered crystal structure and a different stability behavior under air and temperature than the ICT case. The latter opens the question of whether it is possible to enhance the thermoelectric stability by adequate microstructure control. [108]

3.5 DOPING OF THIN FILMS

Doping can strongly affect and be affected by the organic semiconductors' solid-state order. For example, changes in paracrystallinity can modify the energy landscape (e. g., trap density and shape of the DOS) and, in turn, the doping efficiency. The amount of crystalline and amorphous fractions, as well as co-facial $\pi - \pi$ interactions between the dopant and the organic semiconductor, appear to influence the degree of charge transfer (CTC and IPA). Simultaneously, doping can induce changes in the microstructure due to a space-filling effect and charge delocalization.

While it is difficult to predict host:dopant interactions, we can partially control the amount of dopant introduced and the microstructure of the undoped materials via processing. We can classify the processing methods in two categories: Co-processing and sequential processing: the choice of a particular method largely depends on the materials' chemical and physical properties as well as the intended application.

3.5.1 *Co-processing*

SOLUTION MIXING In this method, the dopant and host are mixed in a solvent and then deposited onto a substrate via spin-coating, shear coating, or printing. Naturally, a prerequisite is that both materials have good compatibility between them and miscibility with the chosen solvent system. A clear advantage of this approach is that one can modulate the dopant concentration by regulating the relative amount of each material. However, if charge transfer already occurs in the solution-state, it may render the materials insoluble even when mixing at high temperatures or low concentrations, thus leading to a suboptimal nanostructure. For example, Jacobs et al. demonstrated that solutions of RR-P3HT with 2 % to 4 % were almost insoluble in a wide range of solvents. [115] Similarly, Patel et al. observed gelation and precipitation of the charged polymer in mixtures of F4TCNQ with PBTTT, as indicative of a charge transfer process. They partially solved this issue by heating the host:dopant solution at a temperature of 120 °C. Nonetheless, the resulting films still showed less structural order than those of neat PBTTT.[35]

Another aspect to consider is that doping in organic semiconductors typically requires large amounts of dopant (in the order of mole percent) compared to their inorganic counterparts (in the order of ppm). The latter can lead to significant microstructure changes that may or may not resemble the neat organic semiconductor. For example, Jacobs et al. demonstrated that using co-deposition methods in combination with large amounts of dopant, may lead to suboptimal nanostructure and lower σ compared to other doping methods. [115]. Similar observations were done by Patel et al. when comparing doped films of PBTTT doped via the co-deposition and vapor doping methods. It is challenging to generalize if the resulting film will have a suboptimal microstructure, in fact, recent publications indicate this is not always the case. For example, Paterson et al. presented films of an NDI-bithiophene copolymer doped with TBAF and processed via solution mixing. The films with higher dopant contents presented better charge transport characteristics, which they ascribed to TBAF acting as a morphology additive.[30] Similar results were observed in solution mixtures utilizing Lewis acid dopants.[116, 117]

THERMAL EVAPORATION It consists of the simultaneous thermal deposition of the organic semiconductor (generally a CSM) and the dopant. [60, 61] This type of fabrication method is suitable for bulkier compounds or those with reduced solubility e. g., pentacene and the fullerene derivative $C_{60}F_{36}$.[118] This method often requires complex evaporation setups but allows precise control of the deposition rate and, consequently, in the amount of deposited dopant. Noteworthy, this method can also be employed in a sequential doping manner, albeit not in CPs.

3.5.2 *Sequential doping*

Sequential processing methods rely on adding the dopant onto a preexisting CP or CSM film. This method is advantageous if the goal is to preserve the structural order of the neat film (e. g., for highly ordered CPs, oriented or stretched). Common techniques to add the dopant are via thermal evaporation, aka vapor doping, solution processing and electrochemical doping. We briefly address those methods below.

VAPOR DOPING Alternatively, smaller dopants like I_2 may sublimate at room temperature and thus require simple setups. Similarly, dopants like F4TCNQ may be evaporated at lower temperatures and in simpler setups (e. g., a hotplate and a beaker) — in which case quantifying the added dopant becomes a problem. Another factor to keep in mind is dopant diffusion: molecules like F4TCNQ can spontaneously diffuse in materials like RR-P3HT and PBTTT, while bulkier dopants like $C_{60}F_{36}$ may require thermal annealing after deposition. [35, 118] Fabrication of thick films is also a challenge: µm-scale OTEs are required to generate a significant absolute power output. However, dopant accumulated onto the surface can hamper dopant diffusion through the entire depth of the film. [119] For instance, outstanding results have been obtained using vapor doping, but on films that range between 25 nm to 60 nm. [36, 62, 120] Finally, a common preconception is that vapor doping preserves the crystalline structure of the neat film, albeit recent publications indicate that charge delocalization effects may induce order and long-range connectivity in disordered regions of the film. [121, 122] If the latter is a general rule or applies to certain polymers is still unknown but might prompt further research.

SOLUTION PROCESSING The dopant is infiltrated into a preexisting film via immersion, spin-coating or dip-coating using dopant dissolved in an orthogonal solvent. The dopant content is modulated by controlling the concentration of the dopant solution and immersion time, but the precise dopant content residing within the film must be calculated using other means, e. g., absorption spectroscopy. A key element from this method is that solvents that partially swell but do not dissolve the film appear to improve dopant diffusion. [59] Using this method, Jacobs et al. demonstrated that it was possible to dope films of RR-P3HT uniformly and without significantly disturbing the crystalline structure. [115] Very high σ have been attained using $FeCl_3$ and oriented films PBTTT. [34] Fabrication of thick films using this methodology is also an issue, although some authors have partially overcome the problem. For instance, Hwang et al. managed to dope µm-scale films by submerging the polymer film into the dopant solution using periods of over 1 h.[123] In a different example, Zuo et al. fabricated µm-scale films of RR-P3HT using a multilayer approach.[119] A distinct approach is through the fabrication of foams, which can reach millimeter-thick layers and permit rapid and uniform doping due to their porous nature. [124]

ELECTROCHEMICAL In this method, the electrodes are coated with the polymer via spin coating or using in-situ polymerization. The electrode's potential can then be adjusted so that a charge transfer process occurs between the polymer film and the electrode, prompting an oxidation or reduction process. Modulation of the doping level is also possible in a transistor geometry. Such a device consists of an organic semiconductor as the active layer and an ionic liquid as the gate dielectric. Applying a positive (negative) gate voltage generates positive(negative) carriers in the semiconductor channel upon electrochemical or electrostatic doping. [125] Noteworthy, a common way to synthesize PEDOT-based materials is via electrochemical polymerization, in which the resulting material possess counter charging ions such as PSS and Tos. In this regard, the doping level of PEDOT is partially determined during the polymerization process. Adequate control of the doping level, morphology, and choice of the counterion has allowed PEDOT-based materials to be among the best performing p-type OTEs. [126, 127].

3.6 THESIS STRUCTURE AND AIM OF THE THESIS

Throughout the Part i of this work, we have explained why OTEs have a unique opportunity in the developing IoT market. We presented state-of-the-art materials, essential concepts that influence the thermoelectric performance, and at the same time, the challenges hampering further development.

In this thesis we aim to explore the interplay between microstructure and doping, and how they affect the parameters that govern the merit figure as well as the thermoelectric stability. To address this task, we develop a high-throughput fabrication and characterization methodology for evaluating a large number of samples. We employ such methodology to different extents in the three chapters covering the results.

Part ii of this work contains details of the fabrication and characterization methods used and developed throughout this work, as well as pictures or schematic illustrations of the samples and setups.

Part iii of this thesis contains the results and is structured into three chapters. Chapter 5 introduces the our motivation for developing a high-throughput methodology for fabricating films with doping gradients. We exploit this approach to study different charge transfer states in doped films of PBTTT and how they affect the thermoelectric properties. Chapter 6 extends the doping gradient approach for studying the dependence of the thermal conductivity on the crystalline structure and electrical conductivity. Our main goal is to stretch the current knowledge of how doping affects the thermal conductivity in polymers, and propose a methodology that may accelerate such process. Chapter 7 contains a study of the thermoelectric properties of doped polymer:polymer blends. The main goal is to explore microstructure changes due to the addition of a guest polymer, and how they impact the thermoelectric properties.

Part iv Wraps up the results of this thesis and highlights how they may impact OTE research.

Part II

EXPERIMENTAL SECTION

4

METHODS

ABSTRACT *A large extent of this thesis deals with the optimization of thermoelectrics via processing. In this regard, the fabrication methods and characterization techniques are an essential part of this work and will be revisited in the results chapters ahead.*

4.1 MATERIALS

POLYMER HOSTS AND DOPANTS The polymer hosts and dopants used throughout this work, along with their molecular weight and providers are presented in Table 4.1 . Additionally, their chemical structures are shown in Figure 4.1.

NAME	M_w [kg mol^{-1}]	PROVIDER
regioregular poly(3-hexylthiophene) (RR-P3HT)	50-100	Sigma-Aldrich
regiorandom poly(3-hexylthiophene) (RRa-P3HT)	77	Sigma-Aldrich
poly(2,5-bis(3-tetradecylthiophen-2-yl)-thieno[3,2-b]thiophene) (PBTTT)	70	1-Materials
poly([2,6′-4,8-di(5-ethylhexylthienyl)benzo[1,2-b;3,3-b]dithiophene]3-fluoro-2[(2-ethylhexyl)carbonyl]thieno[3,4-b]thiophenediyl) (PTB7-Th)	141	Ossila
poly[2,6-(4,4-bis-(2-ethylhexyl)-4H-cyclopenta[2,1-b;3,4-b′]dithiophene)-alt-4,7(2,1,3-benzo-thiadiazole)] (PCPDTBT)	30	Sigma-Aldrich
poly[N-9′-heptadecanyl-2,7-carbazole-alt-5,5-(4′,7′-di-2-thienyl-2′,1′,3′-benzothiadiazole)] (PCDTBT)	34	Sigma-Aldrich
poly(9,9-di-n-octylfluorenyl-2,7-diyl) (PFO)	-	Ossila
2,3,5,6-Tetrafluoro-7,7,8,8-tetracyanoquinodimethane (F4TCNQ)	0.276	1-Materials
bis(trifluoromethane)sulfonimide lithium salt (Li-TFSI)	0.287	Sigma-Aldrich

Table 4.1: Polymer hosts and dopants used through out this work.

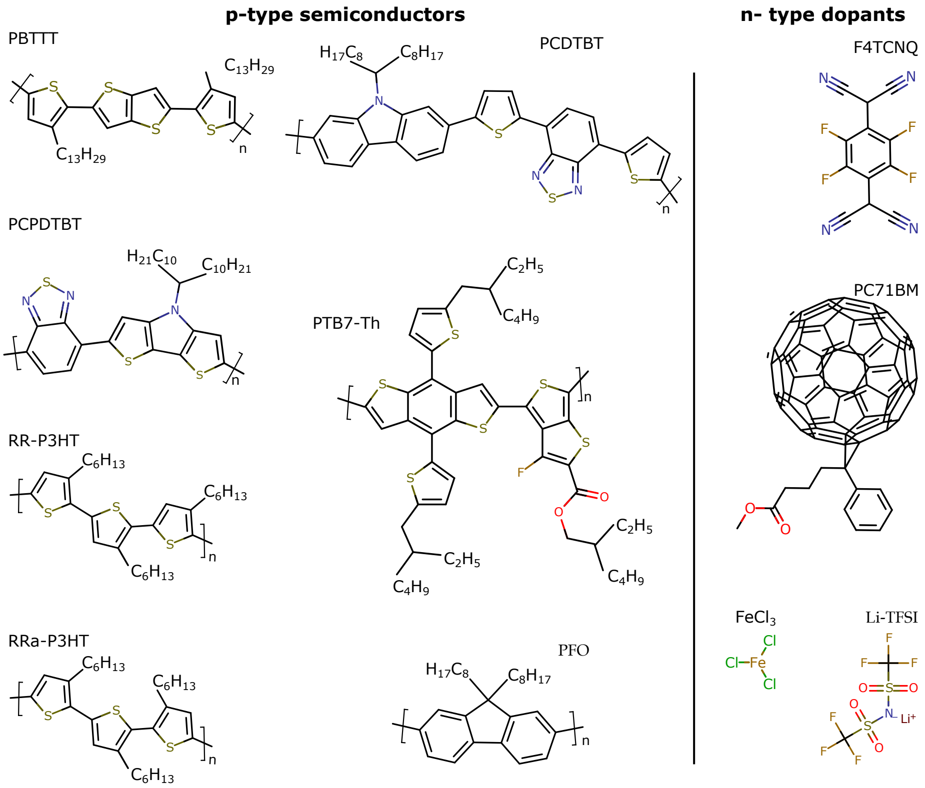

Figure 4.1: Chemical structures for the materials described in Table 4.1

SOLVENTS chlorobenzene (CB) 99.9 % ReagentPlus and 1,2-orthodichlorobenzene (DCB) 99 % ReagentPlus were acquired from Sigma Aldrich. Analytic grade acetone, 2-propanol and ethanol were acquired from Labbox.

4.2 SAMPLE FABRICATION

POLYMER SOLUTIONS RR-P3HT and PBTTT were dissolved in CB at a concentration of 20 mg ml^{-1} inside small vials. The closed vials were placed on a hotplate under continuous stirring at 85 °C for RR-P3HT and 110 °C for PBTTT for a period of 3 h and used at these temperatures before deposition. Other polymer solutions used throughout this work were prepared using the same conditions as RR-P3HT and polymer blends were typically prepared from dilutions of the stock polymer solutions.

4.2.1 *Film deposition*

As substrates, we used microscope glass slides from Labbox. Before deposition, they were cleaned using consecutive sonication baths of 10 min in a Hellmanex solution diluted at 10 % in water and then in isopropanol. Finally, they were dried using an air-flow and processed in a UVO-cleaner for a duration of 5 min.

SPIN COATING Polymer solutions were spin-coated onto cut 20 mm × 20 mm microscope slides in ambient atmosphere, using consecutive steps of 1000 rpm and 3000 rpm for 15 s and 45 s, respectively. Finally, the freshly deposited film was removed from the spin coater and left to dry in ambient atmosphere before annealing. The resultant film thickness ranged from 100 nm to 115 nm both, for RR-P3HT and PBTTT. Figure 4.2 shows a picture of representatives film of RR-P3HT deposited using this technique and Figure 4.4a shows an schematic illustration of the process.

Figure 4.2: Films of RR-P3HT obtained via spin coating RR-P3HT.

BLADE COATING Polymer solutions were blade coated onto 75 mm × 25 mm glass substrates, using a Zehntner ZAA 2300 motorized stage at 110 °C, a blade height of 200 µm and a speed of 30 mm s^{-1}. After deposition, the films were thermally annealed for 15 min using a preheated hotplate at 150 °C and 180 °C for RR-P3HT and PBTTT, respectively, and allowed to cool slowly to room temperature. The resultant film thickness was about 100 nm and 160 nm for RR-P3HT and PBTTT, respectively. Alternatively, films with a thickness gradient were fabricated with a custom-built voltage source constructed by Dr. Bernhard Dörling, which allows to progressively decelerate the blade coating speed during deposition across the length of the glass substrate. [128] Figure 4.3 shows a picture of representatives film of RR-P3HT deposited using this technique and Figure 4.4b shows an schematic illustration of the process.

Figure 4.3: Film of RR-P3HT deposited using the blade coating technique

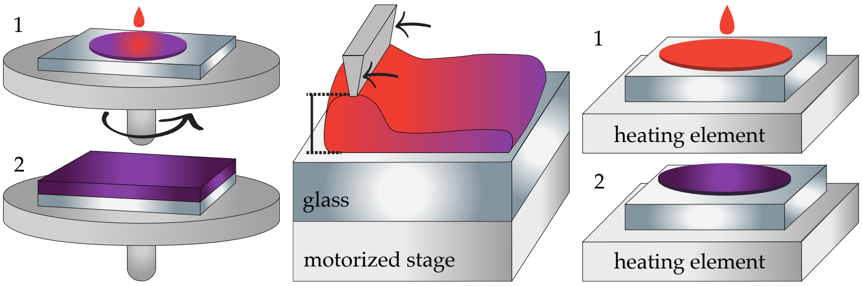

(a) spin casting (b) blade coating (c) drop-casting

Figure 4.4: Schematic illustration of the different film deposition methods. Orange color represents a liquid phase and purple color represents a solid phase.

DROP-CASTING Approximately 70 µl of a polymer solution was cast onto a substrate that was preheated to 80 °C on a custom-built heater placed inside a reactor beaker. The beaker was closed and quickly placed under a reduced pressure, which allowed an almost instantaneous removal of the solvent. Figure 4.5 shows a picture of

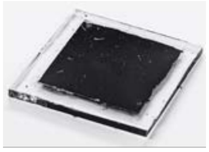

Figure 4.5: Film of PBTTT obtained via drop-casting

representatives film of RR-P3HT deposited using this technique and Figure 4.4c shows an schematic illustration of the process.

ORIENTED POLYMER FILMS Blade coated polymer films were heated on a hotplate at 180 °C and rubbed one time with a thin PTFE membrane attached to a steel blade at a speed of $\approx 1\,\mathrm{cm\,s^{-1}}$.[69] The rubbed polymer films were kept at 180 °C for 15 min and then allowed to cool down to room temperature. In order to avoid polymer degradation, both rubbing and the annealing processes, were done under nitrogen atmosphere in a glovebox. The thermoelectric properties of films fabricated by this method form part of a collaboration published in reference [129]. They are not included in the main text, but rather in the Appendix A, as they do not fully align with the scope of this thesis. However, they comprehend a part of my work that I enjoyed and also showed interesting stability properties that might be interesting to study in the future.

4.2.2 *Temperature annealing and gradients in cristallinity*

Polymer films were thermally annealed (heated→cooled) for 15 min using a preheated hotplate at 150 °C and 180 °C for RR-P3HT and PBTTT, respectively, and allowed to slowly cool to room temperature. Alternatively, gradients in crystallinity were produced by thermally cycling 75 mm × 25 mm polymer films using a Kofler bench, which generates a temperature gradient of $7\,^{\circ}\mathrm{C\,cm^{-1}}$. The resulting film contained varied degrees in crystallinity in the direction of the gradient. Thermal annealing processes were done in nitrogen atmosphere to avoid possible degradation.

4.2.3 *Doping of polymer films*

We chose vapor-phase infiltration with F4TCNQ as our primary doping technique, due to the relatively low sublimation temperature of this dopant (100 °C) and given that this method preserves the crystalline quality of the pre-casted film. [35, 36, 62] We explored two methodologies to control the doping mechanism. First, the conventional one reported in the literature, [35, 130] and then an improved method, which was developed during this thesis and referred to in the following chapters as temperature assisted vapor doping (TAVD).

CONVENTIONAL VAPOR DOPING We employed a 200 mL crystallization beaker as a doping chamber and attached a polymer film face-down onto the lid. Then, we placed approximately 5 mg of F4TCNQ into the bottom of the crystallization beaker and heated the bottom of the doping chamber to 180 °C using a hotplate for a duration of

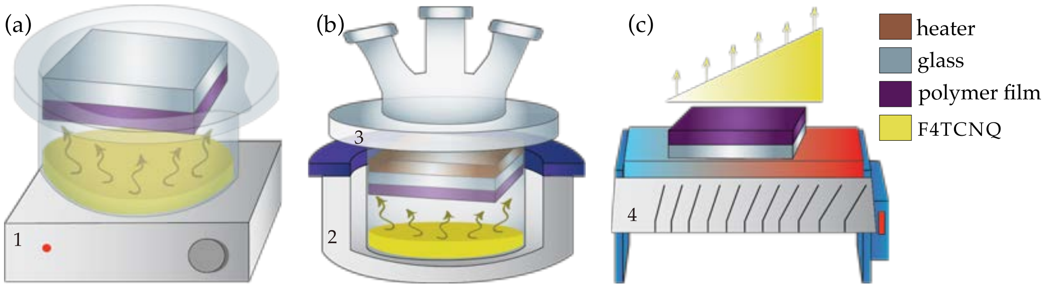

Figure 4.6: Schematic illustration for the setups used for doping and dedoping. (a) Conventional vapor doping, (b) TAVD and (c) dopant gradients by dedoping. Numbers indicate the (1) hotplate, (2) heating mantle, (3) reactor beaker and (4) Kofler bench.

10 min, as seen in Figure 4.6a. During the process of doping, the lid and therefore the sample, heats up slightly in an uncontrolled fashion.

TEMPERATURE ASSISTED VAPOR DOPING To be able to better control the temperature and atmosphere parameters, we modified a 200 mL reactor beaker by inserting a custom-built sample-holder, with an inbuilt heating element and two thermocouples to measure both the sample temperature, as well as the dopant temperature. The sample heating element was controlled via a rheostat, whereas the dopant was heated from the outside through a heating mantle, as seen in Figure Figure 4.6b. A vacuum pump could be connected to the reactor beaker, to decrease the atmospheric pressure before the evaporation was started.

DOPANT GRADIENTS BY DEDOPING Polymer films doped with F4TCNQ are susceptible to dedoping when heated. Kang et al. exploited this concept to control the doping level in films of PBTTT doped with this same dopant. [62] In this thesis work, we elaborate on the same principle by exposing 75 mm long doped polymer films to a temperature gradient using a Kofler bench. As seen in Figure 4.6c, this creates a difference in the sublimation rates across the length of the polymer film. We used this type of samples in Chapter 5 and Chapter 6 to study their properties as a function of dopant content. Figure 4.7 shows a representative picture of a neat and doped film of PBTTT along a section of a film with a doping gradient for comparison.

Figure 4.7: Neat and doped films of PBTTT. Inset is a section of a PBTTT film with a dopant gradient.

ANION EXCHANGE DOPING Rubbed polymer films were doped using a sequential anion exchange method according to the work of Yamashita et al. This method has been recently shown to produce highly conductive samples. For this, films were immersed for 10 min in a 40 °C co-dissolution of F4TCNQ and Li-TFSI 0.3 wt:wt % and 3 wt:wt % in ethyl acetate as the solvent. Finally, the doped films were dried under an air flow to remove the excess solution.

4.3 CHARACTERIZATION

Hereafter we present the qualitative and quantitative techniques used to study doped polymer films i. e., optical absorption spectroscopy for estimating the dopant content and degree of crystallinity, fourier transform infrared spectroscopy (FTIR) to evaluate the degree of charge transfer, Raman spectroscopy for estimating the local electrical conductivity, frequency domain thermoreflectance (FDTR) for determining the thermal conductivity, current-voltage measurements for calculating the electrical conductivity and Seebeck coefficient, Grazing Incidence Wide-Angle X-ray Scattering (GIWAXS) for studying the microstructure and finally Atomic Force Microscopy (AFM) and confocal microscopy for visualization of the morphology.

4.3.1 *Absorption spectroscopy*

For our experiments, optical absorption measurements were taken using a Bruker HYPERION FTIR microscope connected to a VERTEX 70 spectrometer.

CONJUGATION LENGTH AND ORDER The structural order in PBTTT can be controlled through the choice of solvent and post-processing conditions e. g., solvent- and temperature-annealing.[131–133] Analysis of the spectral features assigned to the crystalline regions of PBTTT, allows us to estimate the degree of intrachain order and conjugation length. For our work, we fitted the spectra following a method first described by Spano. [134, 135]

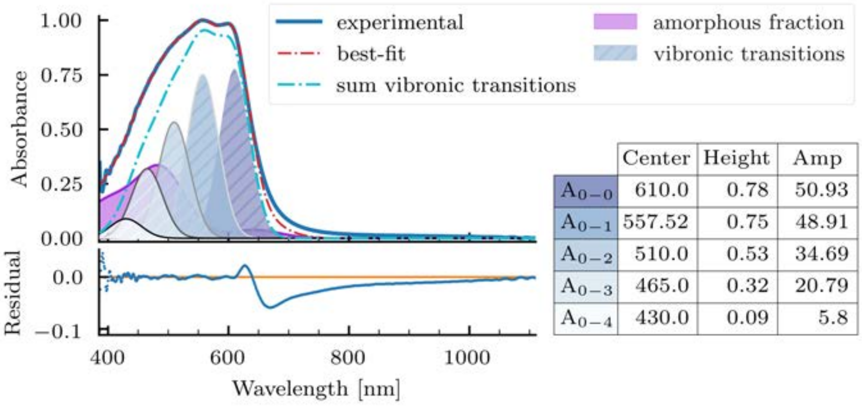

	Center	Height	Amp
A_{0-0}	610.0	0.78	50.93
A_{0-1}	557.52	0.75	48.91
A_{0-2}	510.0	0.53	34.69
A_{0-3}	465.0	0.32	20.79
A_{0-4}	430.0	0.09	5.8

Figure 4.8: UV-Vis absorbance spectra for a film of neat PBTTT. The spectral features were subjected to peak fitting and used for calculating the free exciton bandwidth.

The spectra were deconvoluted into several Gaussian contributions and fitted using a least-square routine implemented in Python with the LMFIT library. [136] Then, the free exciton bandwidth (W) was calculated using the the intensity ratio between the A_{0-0} and the A_{0-1} transitions according to Equation 4.1.

$$\frac{A_{0-0}}{A_{0-1}} \approx \left(\frac{1 - \frac{0.24\,W}{E_p}}{1 + \frac{0.073\,W}{E_p}} \right)^2 \tag{4.1}$$

Where E_p is the intramolecular vibration of the C=C bond of the thiophene ring with an energy of 0.18 eV. Here, a decrease in W indicates an increase in the conjugation length and order. An example of the peak deconvolution is shown in Figure 4.8. Noteworthy, this method has been successfully employed in RR-P3HT and RRa-P3HT. For PBTTT we use it as an approximation. [122, 131, 133, 135, 137]

DOPING LEVEL CTC and IPA formation typically show strong absorption features in the UV-VIS-NIR region, as seen in Figure 4.9. [138, 139] This allows us to identify the formed charge-transfer species and quantify the doping level from their corresponding spectral signatures. [35, 59]

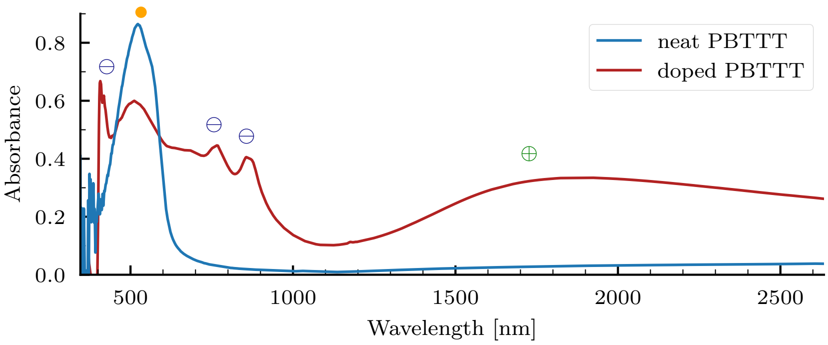

Figure 4.9: UV-Vis-NIR absorbance spectrum for a film of PBTTT, in its pristine state (blue line), and doped with F4TCNQ (red line). Symbols in the plot indicate the characteristic bands of the F4TCNQ$^{\bullet-}$(⊖), the neutral polymer (●), and the polaron (⊕).

First, the absorption spectra were deconvoluted into several Gaussian contributions corresponding to the main species; i. e. neutral polymer, F4TCNQ$^{\bullet-}$ anion and polaron, as seen in Figure 4.10. Fitting was done using a least-square routine implemented in Python using the LMFIT library. [136] Then, the F4TCNQ anion concentration was calculated using the intensity of the anion and a molar extinction coefficient (50 000 mol^{-1} L cm^{-1} for F4TCNQ at 790 nm) [35, 59] along with Beer-Lambert's law following Equation 4.2.

$$\text{O.D} = l\,\epsilon\,c \tag{4.2}$$

Where O.D is the optical density, l is the film thickness, ϵ is the molar extinction coefficients and c is the concentration. The estimated molar ratio of the F4TCNQ anion per PBTTT monomer was estimated using a volume concentration for PBTTT extracted from literature. The latter is typically calculated from the mass of monomer repeating units per unit cell. We note that this method has been used in different publications that employ both PBTTT and P3HT doped with F4TCNQ. [35, 59, 140]

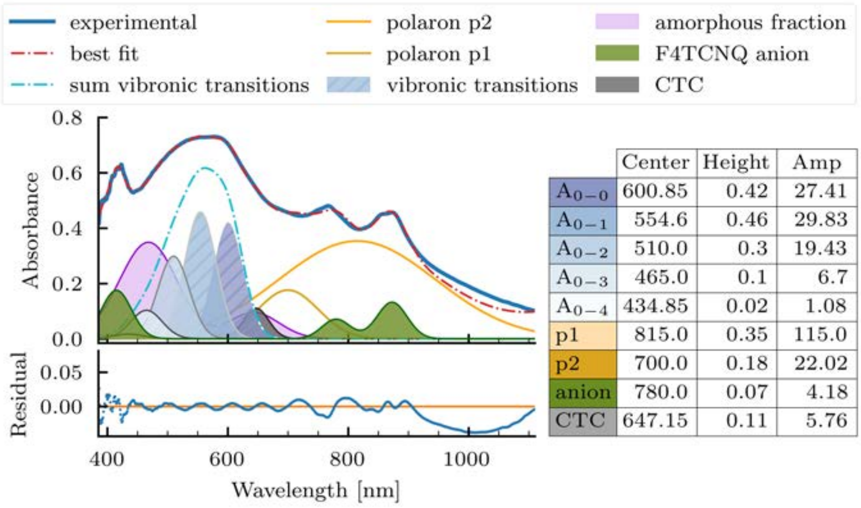

	Center	Height	Amp
A_{0-0}	600.85	0.42	27.41
A_{0-1}	554.6	0.46	29.83
A_{0-2}	510.0	0.3	19.43
A_{0-3}	465.0	0.1	6.7
A_{0-4}	434.85	0.02	1.08
p1	815.0	0.35	115.0
p2	700.0	0.18	22.02
anion	780.0	0.07	4.18
CTC	647.15	0.11	5.76

Figure 4.10: UV-Vis-NIR absorbance spectrum for a film of F4TCNQ-doped PBTTT. The spectral features were subjected to peak fitting and used for calculating the doping level.

4.3.2 *IR spectroscopy*

Fourier transform infrared spectroscopy (FTIR) spectroscopy is a sensitive technique for the characterization of charge-transfer processes. [56, 107, 141] For several polythiophenes, such as 4T, RR-P3HT, RRa-P3HT, and PBTTT, an ICT is denoted by the emergence a broad polaron band centered at ≈3500 cm^{-1} with a tail that extends across the NIR and MIR range. [95, 102, 107] On the other hand, organic semiconductors doped with tetracyanoquinodimethane (TCNQ) derivatives can be studied by measuring the frequency-shift in their characteristic C≡N vibrational mode, which scales with the degree of charge transferred (δ) between the host and the dopant. [107]

For our experiments, measurements were taken with a PerkinElmer Spectrum One spectrometer using the ATR mode. All measurements were done in the solid-sate, on glass substrates and in ambient atmosphere. Figure 4.11 shows a representative spectra for neat and F4TCNQ-doped PBTTT. The observed peaks are assigned to the different $-CH_n$ groups in the polymer and to the C≡N vibrational stretching mode in F4TCNQ.

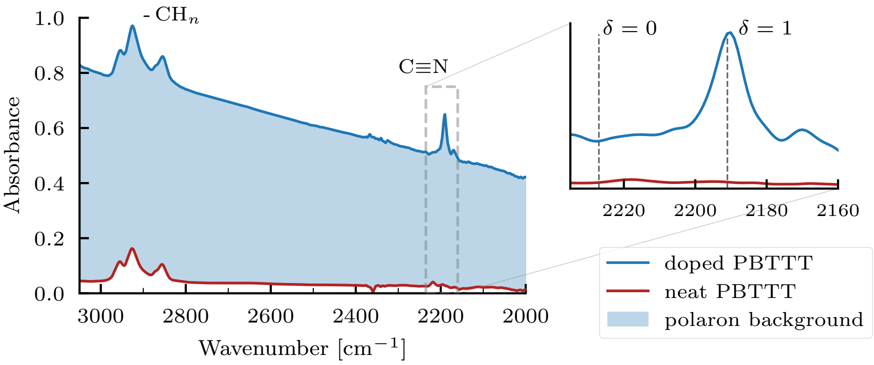

Figure 4.11: FTIR spectra for a neat film of PBTTT and doped with F4TCNQ. Inset corresponds to the region of the C≡N vibrational stretching mode. $\delta = 0$ indicates the position of neutral F4TCNQ (here absent)

DEGREE OF CHARGE TRANSFER The degree of charge transferred was calculated using the frequency shift ($\Delta\nu$) of the C≡N stretching mode in F4TCNQ and following Equation 4.3.

$$\delta = \frac{2\Delta\nu}{\nu_0}\left(1 - \frac{\nu_1^2}{\nu_0^2}\right) \tag{4.3}$$

Where ν_0 corresponds to the C≡N peak in neutral F4TCNQ (at 2227 cm^{-1}) and ν_1 corresponds to the F4TCNQ$^{\bullet-}$ anion (at 2194 cm^{-1}). [107, 141] Here, a $\delta = 1$ is characteristic of an ICT process and a ($\delta < 1$) indicates a FCT process.

4.3.3 *Raman spectroscopy*

Spectra were acquired with a WITec alpha 300 RA confocal microscope, coupled to an Olympus objective with 10 × magnification at the wavelengths of 488 nm and 785 nm.[1] Figure 4.12 present the measured spectra for the neat materials and F4TCNQ-doped PBTTT. The Raman peaks were assigned according to literature[142, 143] and also with the help of DFT calculations (cf. Figure 4.12, Figure 4.13 and Table 4.2).

DENSITY FUNCTIONAL THEORY (DFT) Calculations were done using the ORCA ab-initio, DFT and semi-empirical molecular orbital theory package. [144] Geometry optimization for the polymer was done on two monomer units and the side chains were reduced to ethyl groups in order to reduce computation time. Both, geometry optimization and Raman calculations were done using the long-range separated ωB97X-D3 DFT functional together with an Ahlrichs' triple-split-valence basis set augmented by polarization functions TZVP along an auxiliary def2-TZVP basis set. This level of theory has been found

---

[1] Raman spectroscopy measurements and data processing were done by Dr. Aleksandr Perevedentsev (ICMAB-CSIC).

to be in good agreement for organic compounds, as demonstrated in references [142, 145]. Table 4.2 presents the Raman mode assignment.

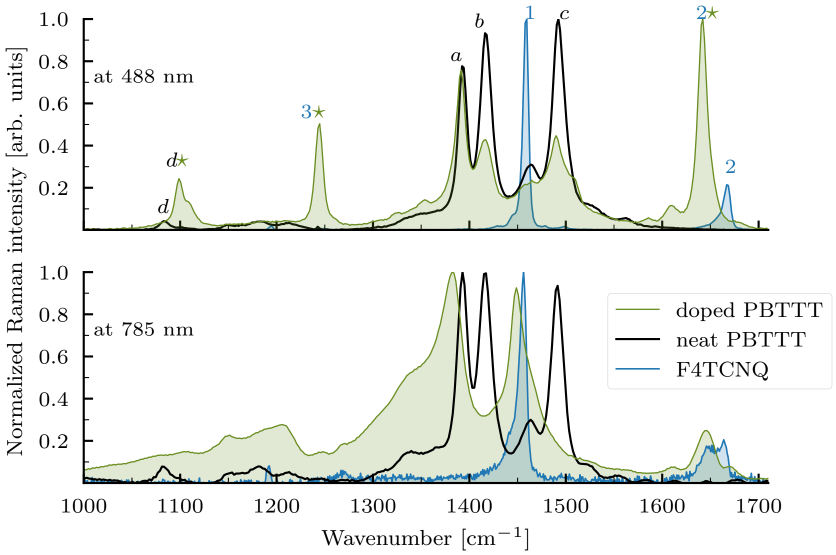

Figure 4.12: Experimental normalized Raman spectra for neat PBTTT, neat F4TCNQ and F4TCNQ-doped PBTTT.

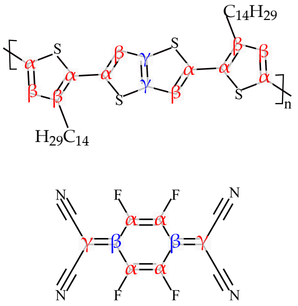

Figure 4.13: Chemical structure of PBTTT and F4TCNQ.

MODE	λ_{exp} [cm^{-1}]	λ_{calc} [cm^{-1}]	DESCRIPTION
a	1393	1346	$C\gamma{=}C\gamma$, stretching
b	1417	1423	$C\alpha{=}C\beta$, stretching
c	1493	1483	$C\gamma{-}C\beta$, stretching, shrinking
d	1098	1156	$C{-}H_n$, bending
1	1457	1468	$C\alpha{=}C\alpha$, stretching
2	1665 → 1645⋆	1659 → 1651⋆	$C\beta{=}C\gamma$, stretching
3	1244⋆	1222⋆	$C\beta{=}C\gamma$, stretching

Table 4.2: Raman mode assignment for PBTTT, F4TCNQ and F4TCNQ-doped PBTTT⋆.

For further reference, our GitHub repository will contain unprocessed data about the Raman measurements and DFT calculations.

CONTACT-LESS ELECTRICAL CONDUCTIVITY The electrical conductivity was calculated according to the work from Perevedentsev and Campoy-Quiles, [146] which, correlates the ratio of a given Raman peaks to a known degree of doping and electrical conductivity. A calibration curve is then obtained, from which the local conductivity can be extracted by measuring local Raman. For PBTTT, this was done with the Raman peaks *a*, *b*, and *c* measured at 488 nm, which change due to the polaron delocalization. The calibration curve was fabricated by consecutively dedoping a sample in different time intervals and measuring the Raman spectra and the electrical conductivity in a four-probe configuration. The intensity ratio, r_{R} and electrical conductivity were fitted to Equation 4.4

$$r_{\mathrm{R}} = A\sigma^{b} + C \tag{4.4}$$

Where $A = 0.40$, $b = 0.21$, and $C = 0.77$ are fit parameters. Figure 4.14 presents the series of experimental measurements utilized for fabricating the calibration curve.

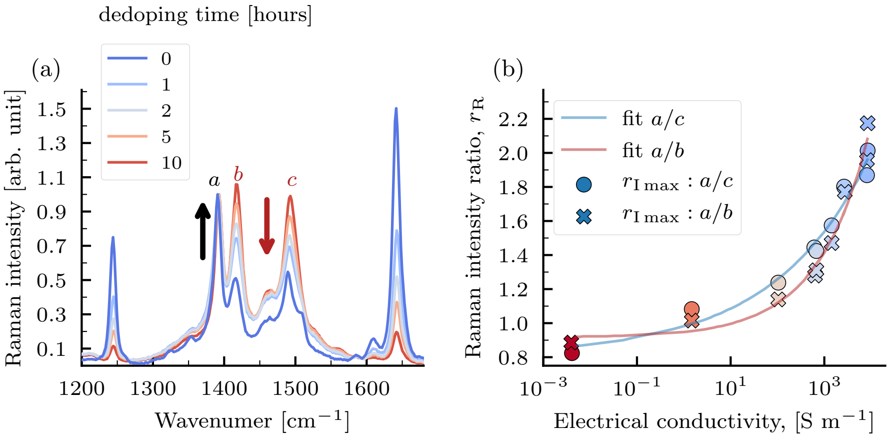

Figure 4.14: (a) Raman spectra used for fabricating the calibration curve. Data corresponds to a series of measurements that will be presented in Chapter 5. Arrows in panel (a) indicate the evolution of the respective modes with increased doping. (b) Calibration curve obtained from the Raman spectra.

4.3.4 *Thermoelectric characterization*

All measurements were conducted using a custom-built setup made by Dr. Bernhard Dörling (see Figure 4.15 and the following schematic illustrations). The setup allowed measuring both, the electrical conductivity and the Seebeck coefficient in a two-probe and a four-probe configuration. Electrodes were deposited by applying a layer of RS pro Silver Conductive Adhesive Paint paste from RS Components using a brush, in order to improve the electrical contact between the polymer film and the probes. All measurements were done under ambient conditions.

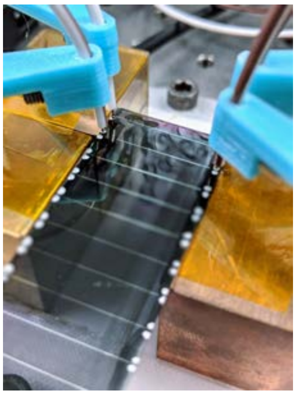

Figure 4.15: Picture of the two probe configuration setup.

ELECTRICAL CONDUCTIVITY In this thesis work, we measured the electrical conductivity using a two- or four-probe configuration. For rectangular samples with a gradient in dopant, we employed a two-probe configuration, directly calculating it from the resistance R and their volume, given by the length l, width w and thickness t as given by Equation 4.5.

$$\sigma = \frac{l}{wt}\frac{1}{R} \tag{4.5}$$

Alternatively, for homogeneous samples we employed the the four-probe configuration. Here, the sheet resistance R_s was calculated using the van der Pauw method, [147] which consist in applying a current on two electrodes and measuring the voltage drop on the other two. This process is repeated for the four orthogonal permutations (see Figure 4.16) and then calculated according the reference Equation 4.6.

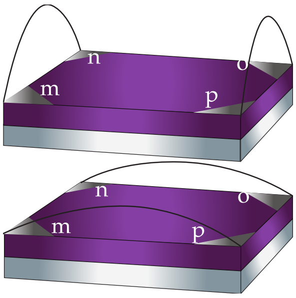

Figure 4.16: Four-probe characterization geometry.

$$e^{\pi \frac{R_{mn,op}}{R_s}} + e^{-\pi \frac{R_{no,pm}}{R_s}} = 1 \tag{4.6}$$

Then, the electrical conductivity is calculated using a known thickness.

$$\sigma = \frac{1}{t}\frac{1}{R_s} \tag{4.7}$$

SEEBECK COEFFICIENT For the two-probe configuration, the samples were fixed on two copper blocks while one of them was slowly heated from room temperature up to a temperature difference of 25 K. The temperature and voltage were recorded on both ends with two T-type thermocouples. Finally, the Seebeck coefficient was extracted from the slope of the heating and cooling cycle. In the four-probe configuration both sides had two contacts, and the Seebeck voltage was also recorded across the diagonals. Figure 4.17 shows the schematic representation for setups used in this work and the experimental output.

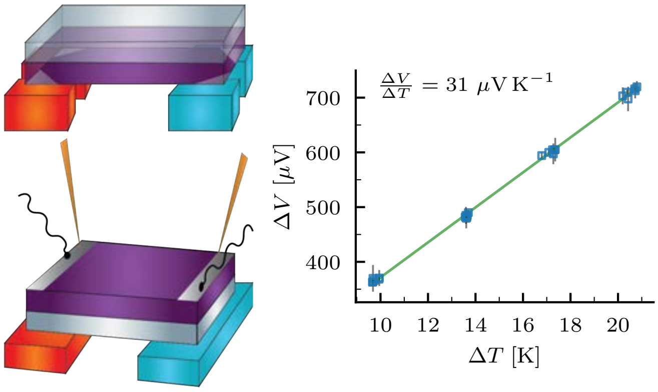

(a) Setups

(b) Experimental

Figure 4.17: Schematics of the Seebeck coefficient setup (a), and example of the determination of the Seebeck coefficient from the slope of the voltage/temperature graph.

4.3.5 *Thermal conductivity*

Frequency domain thermoreflectance (FDTR) was used to measure the thermal conductivity of selected samples fabricated in this thesis. It consists in heating the surface of a polymer film deposited on glass substrate with a pump laser (pump, at 405 nm) and then measuring the change in reflectivity related to the temperature raise with a probe laser (probe, at 532 nm). A lock-in amplifier records the amplitude and phase-response of the heat wave generated by the pump laser and the harmonic response sensed by the probe.

A schematics of the setup is shown in Figure 4.19 and a picture of representative samples used for these type of measurements are showin in Figure 4.18. For our experiments,[2] a gold transducer of ≈60 nm was thermally evaporated onto the surface of the polymer films with an ECOVAP MBraum evaporator to enhance the thermal sensitivity of the method, and to limit the optical penetration depth. Both lasers were focused using an achromatic ≈30 mm lens to a spot size of 10 µm. The pump laser was modulated from 1 kHz to 100 kHz which leads to a modulation of the reflected power of the wave probe laser.

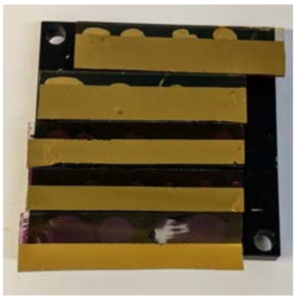

Figure 4.18: Representative picture of films with a doping gradient placed in a holder used for FDTR measurements

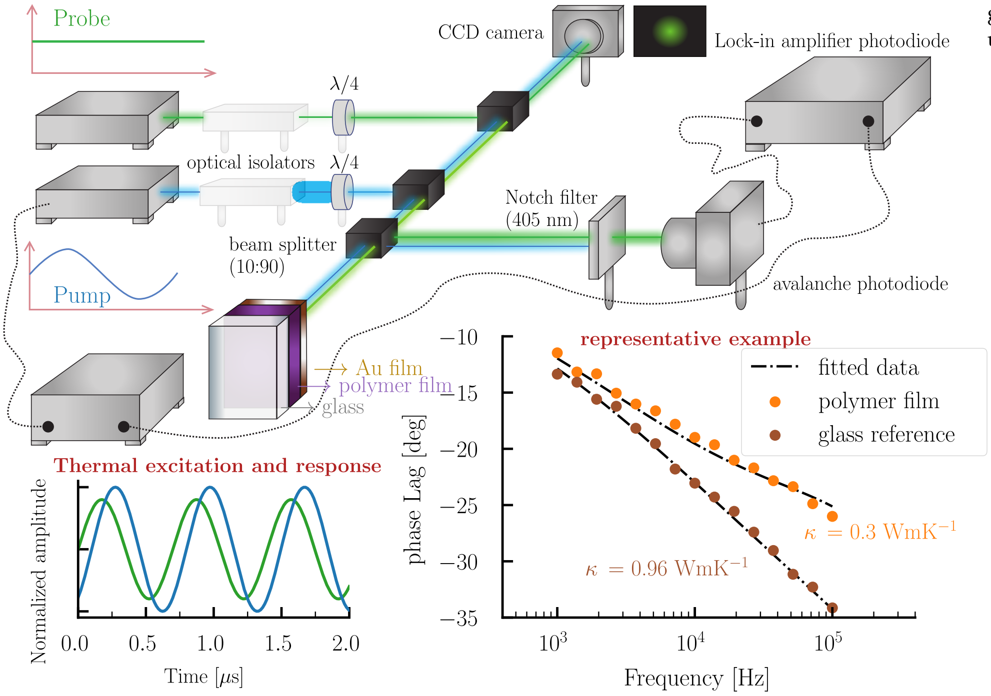

Figure 4.19: Schematic illustration the frequency domain thermoreflectance (FDTR) setup and a representative phase lag response obtained from a reference glass sample and a PBTTT thin film.

The frequency dependent phase lag is modelled numerically solving the parabolic heat equation, given by Equation 4.8 for the described multi-layered geometry, composed of the gold transducer, the polymer thin film, the glass substrate and a thermal boundary resistance at each interface.

$$\frac{\kappa}{\rho C_p}\nabla^2 T - \frac{\partial T}{\partial t} = \frac{1}{\rho C_p} S(r,t) \tag{4.8}$$

---

[2] Measurements were acquired using a custom-built setup and with the support of Dr. Juan Sebastián Reparaz. (ICMAB-CSIC)

Where κ is the thermal conductivity, ρ is the density, C_p is the specific heat, $S(r,t)$ the heat source and, and T the temperature. The cross-plane thermal conductivity ($\kappa \perp$) and the specific heat capacity C_p of the thin films were fitted using a least-squares routine. The obtained data was fitted following the work by Schmidt, Cheaito, and Chiesa[148].

4.3.6 *Morphology*

AFM experiments were done with a Keysight 5500 LS system.[3] Optical micrographs were taken with an Olympus BX51 and a DP20 microscope digital camera. Thickness profiles were acquired with an Alpha-Step D-500 Stylus Profiler. GIWAXS experiments were conducted at the NCD-SWEET beamline at the ALBA synchrotron (Spain).[4] The thin films were exposed for 1 s to 5 s to an X-ray beam with a wavelength of 0.998 Å at an incidence angle of 0.12°. 2D scattering patterns were collected by employing a WAXS LX255-HS detector from Rayonix (pixel size = 40 µm). Noteworthy, the samples used for GIWAXS measurements were deposited on silicon substrates.

4.3.7 *Kinetic Monte Carlo calculations*

kinetic Monte Carlo calculations were done by Dr. Guangzheng Zuo and Dr. Martijn Kemerink (Linköping University, Complex Materials and Devices) using the following parameters: Box size: $10 \times 10 \times 10$, inter-site distance 1.8 nm, Energetic disorder: 0.05 eV, localization radius: 1 nm, Dopant concentration: 8×10^2, Attempt to hop frequency Host: $1 \times 10^{13}\,\mathrm{s}^{-1}$, between:$1 \times 10^{12}\,\mathrm{s}^{-1}$, $1 \times 10^{11}\,\mathrm{s}^{-1}$, Energy offset Host-guest : 0.1 eV, Temperature: 300 K, External field: $1 \times 10^{7}\,\mathrm{V\,m}^{-1}$ (Z direction), DOS type: Gaussian.

---

[3] Measurements were conducted by the Scanning Probe Microscopy laboratory group at the Institut de Ciència de Materials de Barcelona (ICMAB-CSIC).

[4] Measurements were done by Dr. Jaime Martín, Sara Marino and Dr. Edgar Gutierrez. POLYMAT, UPV/EHU

Part III

RESULTS

“*Lucy*: You learn more when you lose
Charlie Brown: Well then I must be the smartest person in world!!!”
— Charles M. Schulz, Peanuts Treasury

5

INTERPLAY BETWEEN DOPING MECHANISM, STABILITY AND THERMOELECTRIC PERFORMANCE

ABSTRACT *Molecular doping is a crucial technique for tuning the thermoelectric properties in conjugated semiconductors. Here we use a precise control of the doping mechanisms to improve the thermoelectric stability of the materials under thermal stress.* [1]

5.1 MOTIVATION

CURRENT TRENDS Early experiments on doping of conjugated semiconductors involved the use of halides and alkali metals. These combinations exhibit a high electron conductivity, but the dopant tends to sublimate quickly, or react with the environment. [120]. To date, improving the thermoelectric stability is commonly approached via three methods;

CHEMICAL STRUCTURE The chemical structure can be tailored to improve the interaction between a particular host:dopant pair. [27, 29, 150] In this regard, Kroon et al. synthesized a polythiophene derivative (Figure 5.1 top) with modified sidechains that enhanced the compatibility and processability when mixed with F4TCNQ. [27] Their results showed improved thermal stability (stable up to 150 °C) compared to a film of F4TCNQ-doped RR-P3HT processed identically (stable up to 100 °C).

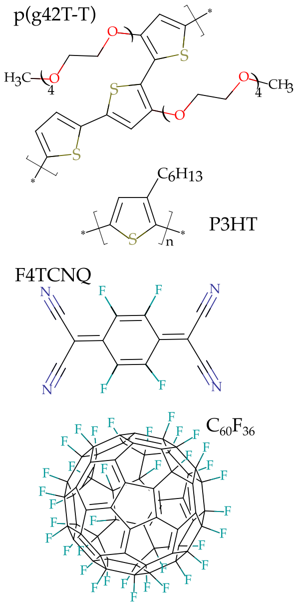

Figure 5.1: Chemical structures for the materials utilized in references [27] and [28].

SIZE Bulkier dopants are less prone to sublimate out of the layer. Li et al. explored this approach using a strong electron-acceptor fullerene derivative (see Figure 5.1) which, showed a good thermal stability (up to 210 °C) compared with other blends employing F4TCNQ. [28] However, a bigger dopant can disrupt the intrinsic polymer's intermolecular packing and thus, affect other properties of interest such as carrier-mobility. Also, bulkier dopants are usually not solution-processable and may require more elaborate techniques for deposition. Finally, a larger dopant size can result in lower doping density.

ENCAPSULATION A more indirect approach is the addition of encapsulation layers to avoid contact with water or oxygen. This can be done by placing barrier-layers on top of the film of interest,

---

[1] A large part of this chapter has been published in "Closing the Stability–Performance Gap in Organic Thermoelectrics by Adjusting the Partial to Integer Charge Transfer Ratio." In: *Macromolecules* (Jan.2020), pp. 609-620 Zapata-Arteaga, Dörling, Perevedentsev, Martín, Reparaz, and Campoy-Quiles [149]

e. g., glass or polymer resins. Abdallah et al. used this approach in films of CNT doped with polyethylenimine (PEI), nonetheless, rigid barrier-layers can compromise the mechanical properties of the device. [91]

A DISTINCT APPROACH Doping can proceed via two doping mechanisms, i. e., an integer charge-transfer process (δ=1) generates an IPA, and a fractional charge-transfer (δ<1) produces a CTC. [95, 102, 107] The conditions that lead to any given species are not fully understood. However, the type of molecular interactions between the host and the dopant is deemed as one of them.[56, 103, 151, 152] For example, Hu et al. demonstrated that in binary crystals bearing 1,3,4,5,7,8-hexafluoro-11,11,12,12-tetracyanonaph-tho-2,6-quinodimethane (F6TNAP) with naphtho[1,2-b:5,6-b′]dithiophene (NDT), the type of interactions dictate the degree of charge transfer, δ (see Figure 5.2). [56] Remarkably, we can hypothesize that each case possesses a different binding strength, that may impact its stability. Nevertheless, limited studies address this approach, due to the difficulty in controlling the doping mechanism and to the less efficient charge generation process in CTCs. [95, 108, 151]

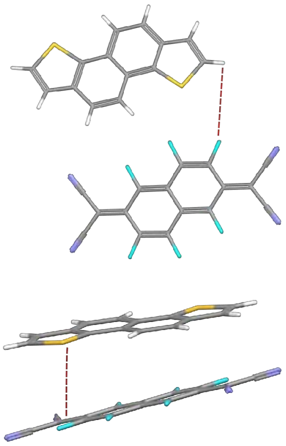

Figure 5.2: Example of C−H···F and $\pi-\pi$ interactions in binary crystals of F6TNAP and NDT according the reference [56].

This chapter introduces a method to accelerate the screening of generated charge-transfer species and thermoelectric properties of doped conjugated polymers, and then we elaborate on a method to systematically control the generated charge-transfer species. We demonstrate that the thermoelectric performance and stability are strongly affected by the specific doping mechanisms. Finally, we perform a broad morphological characterization of the films to understand the origin of the improved thermal stability.

5.2 SCREENING OF CHARGE-TRANSFER STATES

As a starting point it is necessary to identify materials capable of forming CTCs and IPAs. For this, a straightforward, yet laborious plan is to fabricate a large number of samples using distinct dopant concentrations [109] or processing conditions, [108] and characterize them. This is arguably the best approach if the intent is to also study the thermoelectric properties of each case. In this thesis work, we introduce a fast screening approach employing gradients, that significantly decreases the necessary work and makes it more feasible. It consists of maximally doping a polymer film, followed by a progressive *dedoping* along one direction. This provides numerous advantages such as:

1. A large number of different host:dopant ratios are contained within a single self-consistent sample, limited only by the resolution of the dedoping method and the measuring technique.

2. A fast screening of the charge transfer-states existing in the polymer film.

3. Additional information can be extracted depending on the employed dedoping technique. e. g., the thermal stability when using a temperature-induced dedoping method [62, 114]

4. High-throughput study of the thermoelectric properties as a function of the IPA, CTC or the total dopant content.

In this context, we will focus on samples of F4TCNQ-doped PBTTT fabricated through vapor doping. In particular, PBTTT is a well-studied material in the field of organic thermoelectrics due to its high hole mobility, crystallinity, and processability. [35, 55, 68] At the same time, F4TCNQ is compatible with several dedoping techniques [60, 62, 153] and has been previously studied with the former polymer. In brief, sample fabrication consisted in doping pre-deposited polymer films through vapor infiltration. The films then are exposed to a spatial temperature gradient that induces different sublimation rates across the gradient direction. The resulting film possesses a spectrum of host: dopant ratios that vary across one dimension.

In Figure 5.3, we present the IR spectra of a single film of PBTTT with a dopant gradient. This characterization technique can provide information of the charge transfer states in TCNQ derivatives by following the changes in the C≡N vibrational stretching mode. [95, 107]

Further details can be found in Chapter 4.

Section 4.2.3 and Section 4.3.2 present the methodologies for fabricating polymer films with a dopant gradient and for calculating δ

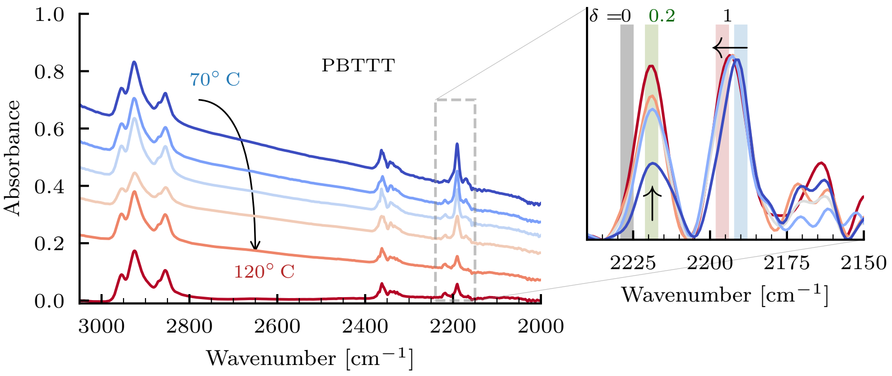

Figure 5.3: IR spectra for a film of PBTTT with a dopant gradient. Inset shows the region of the C≡N stretching mode normalized at 2187 cm^{-1}. Vertical lines are a guide to the eye for the characteristic peaks, 2187 cm^{-1} blue, 2194 cm^{-1} red, 2218 cm^{-1} green, and 2229 cm^{-1} gray. δ indicates the degree of charge transfer at each position.

Here, a dedoping process is observed by the disappearance in the absorbance of the polaron background and the peaks that belong to the F4TCNQ$^{\bullet -}$ ($\delta = 1$), at 2187 cm^{-1} and 2194 cm^{-1}. In *co-deposited* films of RR-P3HT with F4TCNQ, these peaks are ascribed to dopant residing in the polymer's side chain- and backbone-region, respectively.

[114] Additionally, we observe a peak at $2218\,\mathrm{cm}^{-1}$ that belongs to a CTC with a $\delta = 0.2$. [107] This peak becomes more evident with further de-doping, possibly due to (i) an overlap with the polaron background or to a (ii) temperature-induced reorganization of inactive dopant. Nonetheless, we can interpret that the peaks at $2218\,\mathrm{cm}^{-1}$ and $2194\,\mathrm{cm}^{-1}$ represent the more thermally-stable species, given that they have been exposed to a higher temperature for the same amount of time. Also noteworthy, the UV-Vis absorbance spectra for the same sample (Figure 5.4), shows only the bands of the anion and the neutral polymer, but not an additional band that can be assigned to the CTC, presumably due to the small fraction of CTC that is overlapped with the other contributions.

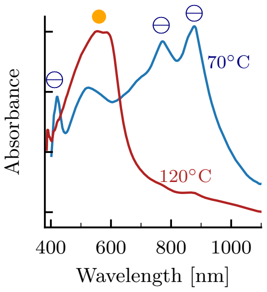

Figure 5.4: UV-Vis absorbance spectra for the film depicted in Figure 5.3. Symbols in the plot indicate the characteristic bands of the F4TCNQ$^{\bullet-}$(⊖) and the neutral polymer (●).

The previous results demonstrate that PBTTT naturally forms a mixture of a CTC and IPAs states. Remarkably, our IR analysis suggest the existence of three populations, specifically, one from the CTC at $2218\,\mathrm{cm}^{-1}$ and two from the IPA at $2194\,\mathrm{cm}^{-1}$ and $2187\,\mathrm{cm}^{-1}$. From the temperature induced-dedoping gradient, we can deduce a higher thermal stability for the species at $2218\,\mathrm{cm}^{-1}$ and $2194\,\mathrm{cm}^{-1}$. In this regard, we expect that a polymer film containing predominantly these species will be more thermally stable.

5.3 CONTROLLING THE DOPING MECHANISM

5.3.1 *Thermoelectric properties as a function of the charge-transfer state*

The next step is to promote a higher content of the CTC and the IPA at $2194\,\mathrm{cm}^{-1}$. To our knowledge, there is no crystallographic data that identifies the CTC's position within the PBTTT microstructure. Nonetheless, several authors place these species closer to the conjugated core of the host material. [56, 103, 151, 152, 154] To this end, we elaborate on a concept introduced by Lim et al., who used an elevated substrate temperature during the doping process. This induces an expansion in the lamellar- and in the $\pi - \pi$-stacking direction, which improves the diffusion of F4TCNQ. [130, 149] To properly control the doping conditions, we employ a custom-built vessel that allows to independently control the temperature on the polymer's substrate (T_{subs}) as well as of the dopant (see Section 4.2.3 for further details).

In the following sections, we distinguish between two doping methods; (1) A *conventional* one, where only the temperature of the dopant source is controlled, and (2) *temperature assisted vapor doping*, TAVD, which uses the vessel described above.

SUBSTRATE TEMPERATURE First, we analyze the effect that T_{subs} has on the doping process while using a fixed doping time (t_d) of 10 min.

Figure 5.5a, shows the absorbance of doped PBTTT using distinct T_{subs}: 70 °C, 110 °C and 130 °C. Here, the bands of the anion increase in intensity, compared to the neutral polymer when using a higher T_{subs}. Moreover, when reaching a T_{subs} of 130 °C a new band appears at 630 nm, which corresponds to the CTC presented in Figure 5.3. We highlight that this band is *not* present in the film doped through the *conventional* method (see Figure 5.4).

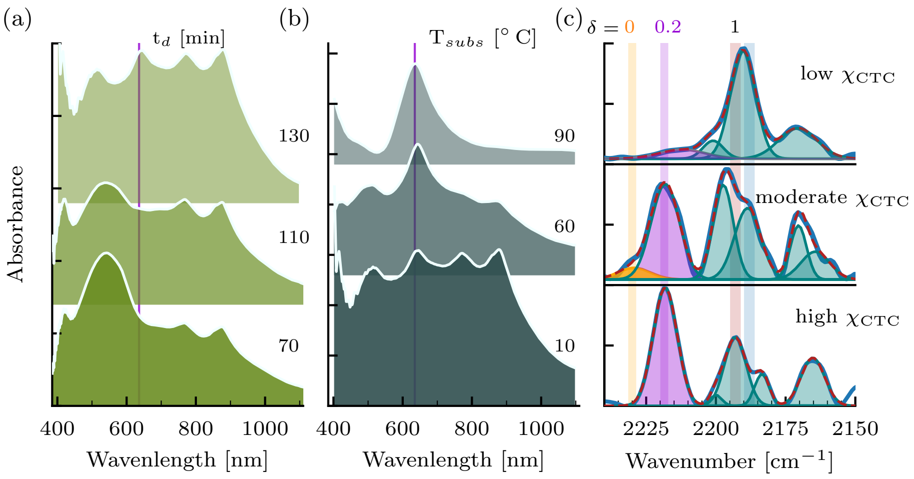

Figure 5.5: Screening of the doping conditions. UV-Vis absorbance for doped PBTTT with different (a) substrate temperatures and (b) doping time. (c) IR spectra for selected samples. Spectra were subjected to peak fitting according the reference [109] to estimate the CTC fraction.

DOPING TIME After identifying the temperature that promotes the formation of CTCs, a natural continuation is to increase its quantity by extending the doping time. For this we fix the T_{subs} at 130 °C and evaluate different t_ds, 10 min, 60 min and 90 min. As seen in Figure 5.5b, the bands ascribed to the neutral polymer and the anion decrease in intensity with a longer t_d, until at 90 min the only visible spectroscopic signature is that of the CTC.

CTC CONTENT With IR spectroscopy (see Figure 5.5c), we can classify the doped polymer films according to their respective CTC/IPA fraction (χ_{CTC}). For this, we subject the spectra to peak fitting, and compare the integrated intensity between the peaks of the CTC and the IPA (Table 5.1 presents a summary of the conditions and thermoelectric properties for each classification.).

Here we observe that the peaks at 2194 cm^{-1} and 2187 cm^{-1} are better resolved for the moderate and high χ_{CTC} samples when compared with the low χ_{CTC} case. Also noteworthy, the electrical conductivity scales inversely with the χ_{CTC}, e. g., it drops by approximately one order of magnitude when moving from the low to the max χ_{CTC} scenario (cf. χ_{CTC} and σ in Table 5.1). This is in line with the observations

χ_{CTC}	T_{subs} [°C]	t_d [min]	σ [S cm^{-1}]	S [µV K^{-1}]
– (low)	not-heated	10	92	60 ± 3
0.34 (moderate)	130	10	85	62 ± 4
0.54 (high)	130	60	9	121 ± 14
– (max)	130	90	3	175 ± 31

Table 5.1: Summary of the doping conditions and their thermoelectric properties

by Jacobs et al. and Méndez et al., indicating a less efficient carrier generation process in films containing CTCs. [107, 108] The Seebeck coefficient, on the other hand, increases with increasing χ_{CTC}, as one may expect from a reduced charge carrier density.

These results demonstrate that for films of PBTTT, it is possible to adjust the CTC content using the TAVD method. Notably, there is an inverse correlation between the χ_{CTC} and the electrical conductivity. However, introducing a moderate χ_{CTC} has a tolerable penalty in the electrical conductivity, especially if the Seebeck increase partially compensates the lower σ values and (as we will see) the long-term stability out-performs a film with a low χ_{CTC}.

5.3.2 *Stability as a function of the charge-transfer state*

Now we focus on evaluating the long-term stability for three selected samples. For this we subject each film to a thermal stress, and correlate the evolution of the spectral features and thermoelectric properties as a function of the annealing time. As dedoping conditions we chose a fixed temperature of 100 °C, which promotes dedoping both from the backbone- and sidechain-region. [114] For the annealing time (t_a) we examine two regimes, (i) from as-doped to 60 min in small time-intervals and (ii) from 1 h to 10 h in long time-intervals.

ABSORPTION FEATURES Figure 5.6 presents the absorbance spectra for the dedoping experiment described above. After 10 h, the bands corresponding to the anion in the sample with a low χ_{CTC} are very subtle. Alternatively, the moderate χ_{CTC} case still shows the characteristic bands of the anion and a shoulder at 633 nm that belong to the CTC. Strikingly, in the film with a high χ_{CTC}, the same spectral features show little change, and band of the CTC even increase in intensity after a t_a of 60 min, possibly due to a temperature-induced reorganization of inactive F4TCNQ.

ELECTRICAL CONDUCTIVITY Figure 5.7a presents the electrical conductivity for the samples measured earlier. As-doped samples ($t_a = 0$) show values that are in agreement with those presented in Table 5.1. After 10 h, σ drops to 0.01 S cm^{-1}, 6 S cm^{-1} and 0.87 S cm^{-1} for

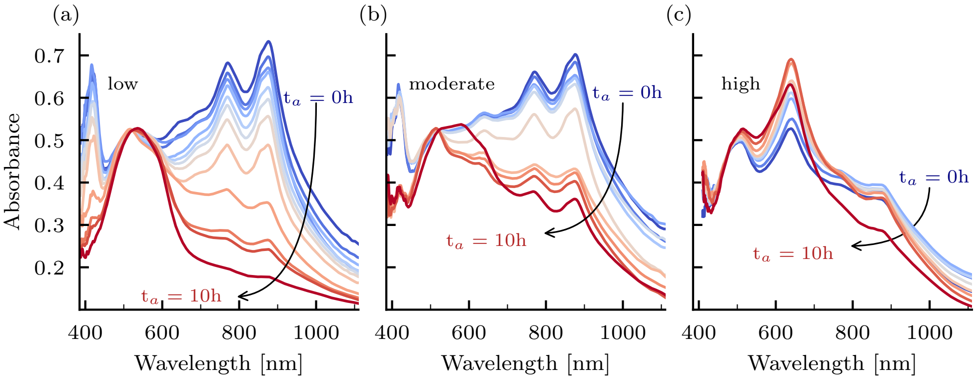

Figure 5.6: UV-Vis absorbance spectra for dedoped films of PBTTT with (a) low, (b) moderate and (c) high χ_{CTC}.

the films a with low, moderate and high χ_{CTC}, respectively. Noteworthy, the decline in σ resembles the trend observed in the absorbance spectra for the the anion band (Figure 5.6), further suggesting a faster dedoping rate for the IPA species.

SEEBECK COEFFICIENT The Seebeck coefficient S follows an opposite trend to that of σ (Figure 5.7b). The films with a low and a moderate χ_{CTC} start at $\sim$60 µV K^{-1} which then increases to 173 µV K^{-1} and 110 µV K^{-1}, respectively. The sample with a high χ_{CTC} increases marginally, in agreement with its measured electrical conductivity.

THERMAL CONDUCTIVITY In Figure 5.7c we present the measured thermal conductivity κ for the samples with a low and moderate χ_{CTC}. First we note that κ in the as-doped samples is lower than the intrinsic value for neat PBTTT. However, we highlight that doped organic semiconductors operate in the so called *'impurity reserve regime'* [155], which is expected to affect the thermal transport in the polymer's network. Then, after two hours, κ increases considerably with a trend that moves towards the values of neat PBTTT, indicating a more similar structure to the reference sample. However, we stress that the increase in κ above 1 W m^{-1} K^{-1} is *not* due to a higher electronic contribution in the thermal conductivity. In fact, as we will see later, it is instead due to dopant crystals accumulated on the surface, which introduce an additional parallel channel that conducts heat, and therefore increases the apparent thermal conductivity. In this regard, we can suggest that the changes observed in κ are due to the dopant-induced disorder and its subsequent desorption.

Further analysis of the thermal conductivity as a function of doping is presented in Chapter 6.

FIGURE OF MERIT Figure 5.7d presents the ZT for the films with a low and a moderate χ_{CTC}. Notably, the optimal value is observed around 0.08 after 30 min of annealing in both samples. After 10 h, this value drops between 1×10^{-5} and 4×10^{-4}. Nonetheless, we

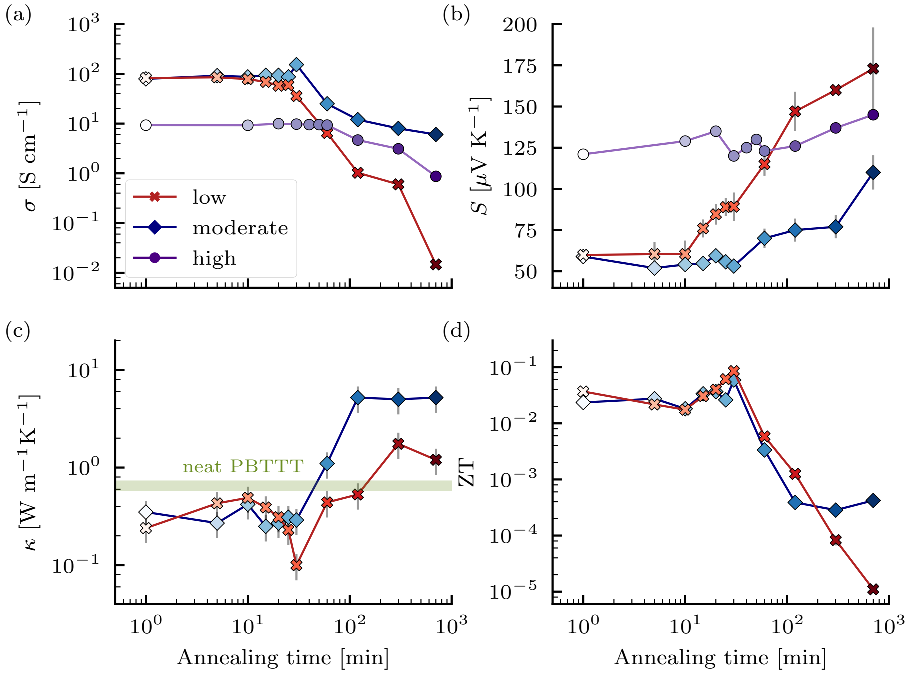

Figure 5.7: (a) Electrical conductivity, (b) Seebeck coefficient, (c) thermal conductivity and (d) ZT for dedoped films of PBTTT as a function of the annealing time. Color gradient is to improve clarity between different points

emphasize that the value for the moderate χ_{CTC} case is likely higher, due to the overestimation in κ.

OPTICAL MICROSCOPY Non-polarized micrographs in Figure 5.8 further support the stability differences seen seen between the low and moderate χ_{CTC} series. Here, films with a lower doping level show a characteristic pink color of neat PBTTT. Notably, this effect is more pronounced in the low χ_{CTC} series (cf. first and third row of Figure 5.8). On the other hand, during the dedoping process, F4TCNQ diffuses out of the film and aggregates onto its surface. Notably, we can track this event using cross-polarized microscopy as a function of the annealing time and infer how long the dopant was residing within the microstructure.

Figure 5.8 shows the micrographs for the low and moderate cases. Notably, even after 2 h, there is a noticeable amount of crystals in the moderate χ_{CTC} series indicating dopant is still residing in the film up to that moment. In contrast, there are no crystals in the low χ_{CTC} series already after 1 h of annealing, suggesting that a large portion of the dopant left the polymer microstructure before that annealing time. Finally, we highlight that dopant crystals in the 'as-doped' micrographs are *not* related to a dedoping effect, but rather to an excessive condensation of F4TCNQ during the *conventional* vapor doping process. This is not observed in samples processed with the

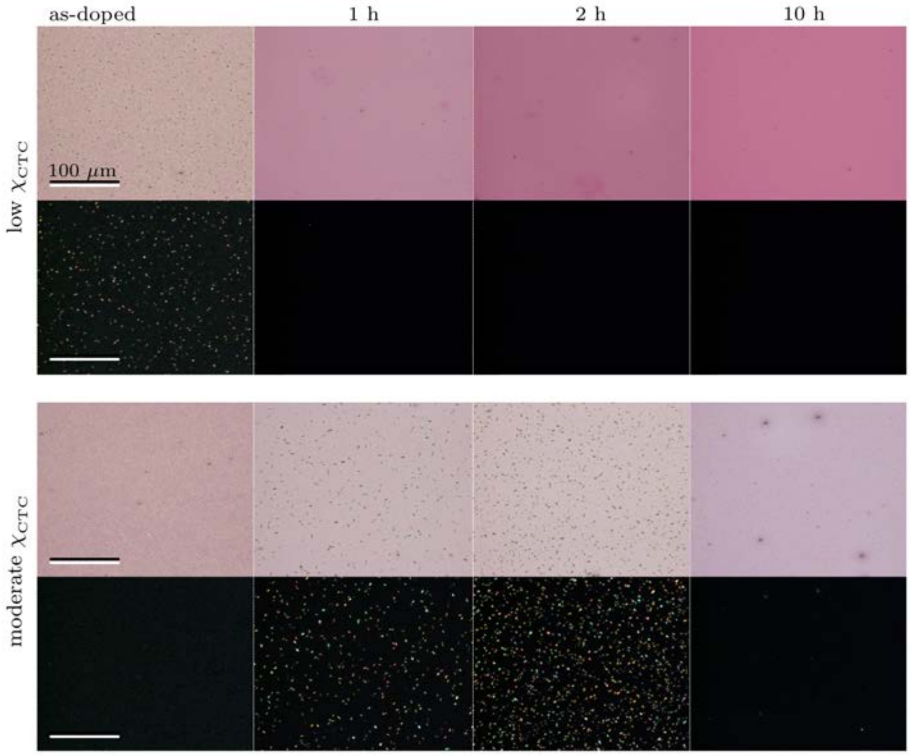

Figure 5.8: Micrographs taken under non-polarized (first and third rows) and cross-polarized (second and fourth rows) light for the films with a low and a moderate χ_{CTC} as a function of the dedoping time. [a]

---

[a] Micrgrpahs taken by Dr. Aleksandr Perevedentsev

TAVD method, likely due to the higher substrate temperature which prevents a drastic temperature change between the vapor phase and the polymer's surface.

These results demonstrate various key aspects. On one side, the optical and thermoelectric characterization corroborate superior thermal stability for CTC compared with the IPA. On the other hand, films with a higher CTC content show lower thermoelectric performance, presumably from the inefficient carrier generation process reported for this charge-transfer species. Remarkably, a relatively low χ_{CTC} ($\sim$ 30%) appears to improve the long-term stability without compromising the thermoelectric properties. In the following section, we try to assess whether dopant contributing to the CTC and the IPA reside in distinct places within the microstructure. This way, we expect to answer if the differences in the thermal stability are due to a stronger molecular interaction between the host and the dopant or due to the dopant residing in places less prone to dedoping.

5.4 INTERPLAY BETWEEN MICROSTRUCTURE AND STABILITY

Here we determine if the improved thermal stability comes from differences in the dopant's localization. For this, we employ two characterization techniques; (1) Raman Spectroscopy, which provides a picture of the vibrational changes caused by the polaron, (2) and GIWAXS, which gives information about the distortions introduced by the dopant in the polymer's lattice.

5.4.1 *Raman spectroscopy*

Figure 5.9 shows the Raman spectra for the films with a low, moderate, and maximum χ_{CTC} using an excitation wavelength of $\lambda_{ex} = 785\,\mathrm{nm}$. First, we take a look at the spectra's central region. Here we see three peaks at $1393\,\mathrm{cm}^{-1}$, $1417\,\mathrm{cm}^{-1}$ and $1493\,\mathrm{cm}^{-1}$, that belong to the C=C symmetric and anti-symmetric stretching modes in the thienothiophene and thiophene rings. (see Section 4.3.3 for further details) [142, 143, 156]

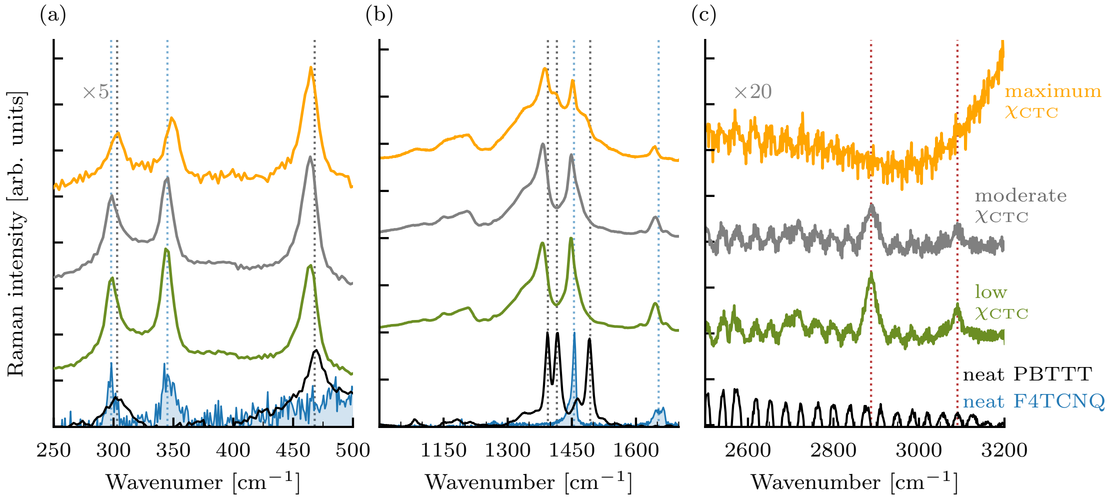

Figure 5.9: Raman spectra as a function of the χ_{CTC} using a λ_{ex} of 785 nm. Vertical dashed lines are a guide to the eye for the characteristic peaks in neat PBTTT and neat F4TCNQ. Data in panels (a) and (b) is scaled by ×5 and ×20 for clarity.

In PBTTT, these modes change with doping due to the polaron's delocalization across the conjugated core, which leads to a structural relaxation and a change of the corresponding vibrational modes. [142, 157] This effect is denoted by a gradual quenching of the peaks at $1417\,\mathrm{cm}^{-1}$ and $1493\,\mathrm{cm}^{-1}$ and accompanied by a shift of the peak at $1393\,\mathrm{cm}^{-1}$ towards lower energy vibrations (see Section 4.3.3). In this regard, the changes in this region are proportional to the polaron concentration and, therefore, to the changes in the electrical conductivity.

Additionally, we note that the intensity of the peak ascribed to the F4TCNQ anion at 1417 cm^{-1} decreases with a higher CTC content.

In the range of high energy vibrations (Figure 5.9c) we observe two peaks at 2888 cm^{-1} and 3100 cm^{-1} for the low and a moderate χ_{CTC} case but *not* for the film with a maximum χ_{CTC}. This region is typically related to the C$-$H$_n$ stretching vibrations, and thus, we ascribe it to the side chains in PBTTT. This is indicative of (i) a higher interaction between the side chains and the F4TCNQ anion [114] (ii) and to an absence of the CTC in the same vicinity.

In the range of low energy vibrations, we observe two peaks at 298 cm^{-1} and 344 cm^{-1}. By comparison with the neat spectra of F4TCNQ and with the help DFT calculations we ascribe this peak to the C$-$F bending mode. Interestingly, the peak at 345 cm^{-1} shifts towards higher energies but only for the sample with a maximum χ_{CTC}. The latter suggests two distinct charge-transfer populations, i. e., at 345 cm^{-1}, those with a higher IPA content, and at 350 cm^{-1} with a majority of CTC states.

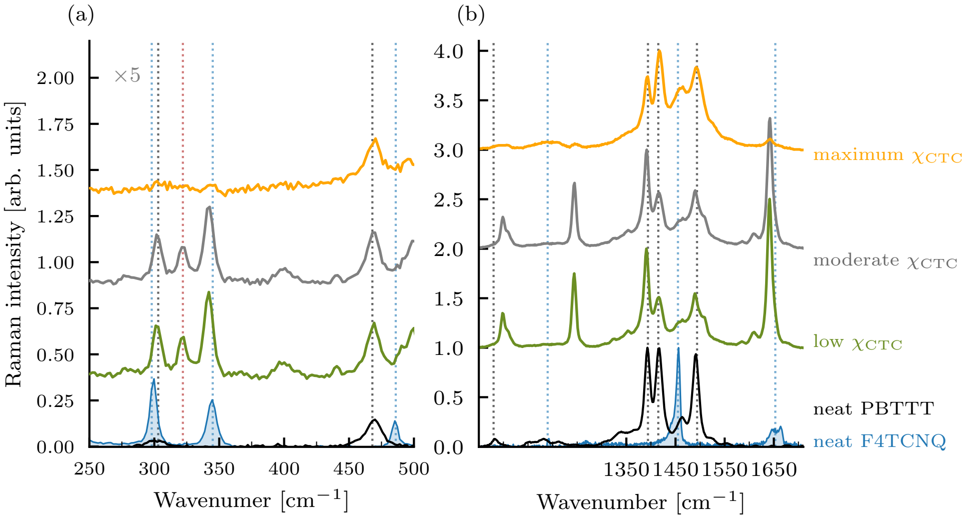

Figure 5.10: Raman spectra as a function of χ_{CTC} using a λ_{ex} of 488 nm. Vertical dashed lines are a guide to the eye for the characteristic peaks in neat PBTTT and neat F4TCNQ, red guideline corresponds to an unassigned feature. Data in panel (a) is scaled by ×5 for clarity.

Now we analyze the Raman spectra measured with a λ_{ex} of 488 nm (Figure 5.10). Contrary to the measurements at 785 nm, this wavelength preferentially excites the amorphous regions in PBTTT. Here we see two peaks at 1244 cm^{-1} and 1645 cm^{-1} that belong to the C=C stretching mode in the F4TCNQ anion. As in Figure 5.5 these peaks are also *absent* for the maximum χ_{CTC} case (t_d=90 min). Additionally, we see a peak at 1098 cm^{-1} that we ascribe to the C$-$H$_n$ bending mode in the sidechains and the conjugated core. This peak increases in intensity with doping, presumably due to the presence of dopant allocated in the sidechain-region. Notably, this peak is also absent for the maximum χ_{CTC} case. These observations indicate a lower dopant content generating IPA states in the maximum χ_{CTC} and also, an unlikely presence of the CTC in the amorphous region.

On the other hand, in the range of low energy vibrations, we observe two peaks at $303\,\mathrm{cm}^{-1}$ and $345\,\mathrm{cm}^{-1}$ for the films with a low and moderate χ_{CTC}. Notably, these peaks are *absent* for the maximum χ_{CTC} case at this wavelength but not for $\lambda_{ex} = 785\,\mathrm{nm}$, suggesting the CTC its absent in the amorphous region.

5.4.2 *Microstructure*

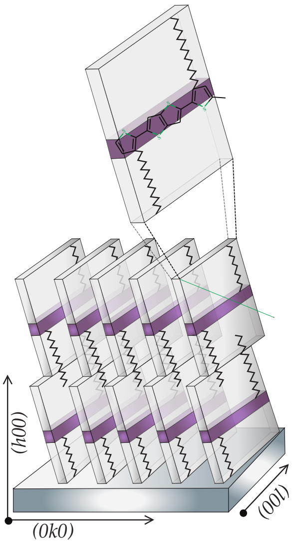

Figure 5.11: Schematic illustration for the microstructure in neat PBTTT.

To further understand the interactions of the dopant in the polymer's crystalline region, we performed GIWAXS. Fortunately, the structure of PBTTT is relatively well-known and has been reported in several publications. Neat PBTTT orients in an edge-on, tilted configuration with respect to the substrate, with sidechains that are interdigitated, as seen in Figure 5.11. [55, 59, 62, 67, 68, 132]

When co-deposited from solution with F4TCNQ, the films possess two noticeable differences in the $(h00)$ and the $(0k0)$ crystalline planes when compared with neat PBTTT. (i) The (100) and (200) peaks shift towards a lower scattering vector, indicating an expansion in the lamella stacking-distance and (ii) the (010) peak shifts towards a higher scattering vector, indicating a contraction in the $\pi - \pi$ stacking direction [158]. Cochran et al. accredited the latter to (i) F4TCNQ residing in the sidechain-region and (ii) to dopant units intercalated with the aromatic core, creating voids along the backbone that are then filled with adjacent backbone units (as seen in Figure 5.12a and Figure 5.12b). [158]

On the other hand, using *conventional* vapor doping is typically considered that does not alter the in-plane scattering features. This has been attributed to F4TCNQ residing *only* in the sidechain (see Figure 5.12c) region based on two considerations; (1) The (010) spacing in pre-deposited films does not allow the infiltration of F4TCNQ molecules. (2) An intercalation of dopant between the polymer backbone, would result in a considerable lattice expansion in order to compensate for the volume occupied by the dopant. [35, 62] Strikingly, in our experiments using the TAVD method, we do observe an alteration in the (010) crystalline plane.

Figure 5.13 presents the GIWAXS scattering patterns for the samples with a low, moderate and maximum χ_{CTC} and the summarized data is presented in Table 5.2. In agreement with literature, we observe a shift towards lower scattering vectors for the out-of-plane peaks. Noteworthy, the (100) peak shifts proportionally to the χ_{CTC} and consequently, the larger expansion is seen on the maximum χ_{CTC} case (cf. low, moderate and max in χ_{CTC} Table 5.2).

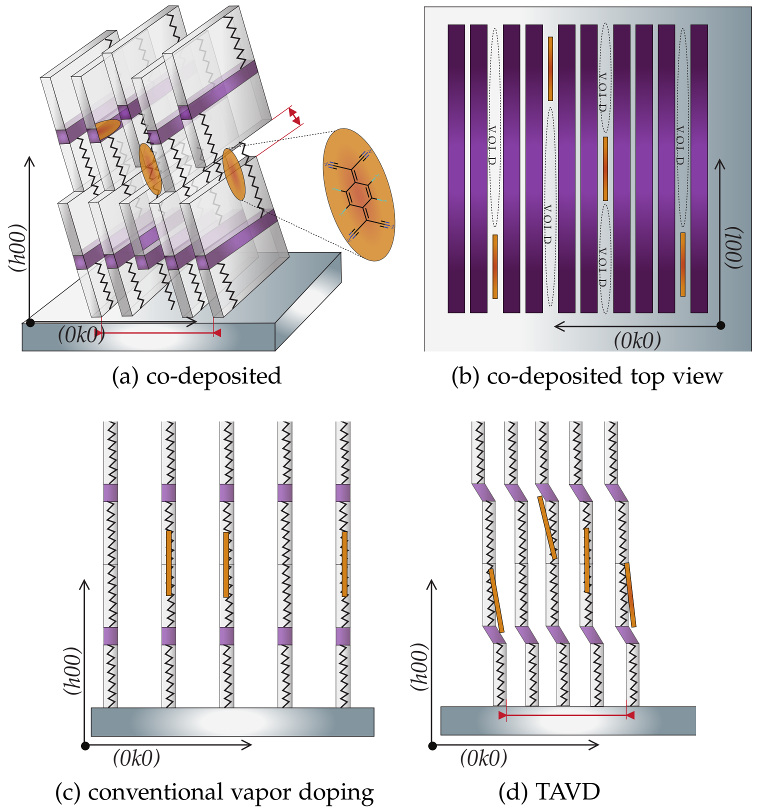

(a) co-deposited (b) co-deposited top view

(c) conventional vapor doping (d) TAVD

Figure 5.12: Microstructure illustrations for films of F4TCNQ-doped PBTTT processed via (a), (b) co-deposition, (c) conventional vapor doping and TAVD. Red arrows indicate an expansion or contraction in the corresponding direction

On the other hand, and in contrast with the work by Kang et al., in-plane features show a contraction of the $\pi - \pi$ stacking distance (Figure 5.13). Such a change could be explained by a tilting in the polymer backbone, as seen for co-crystals of PBTTT and [6,6]-phenyl-C71-butyric acid methyl ester ($PC_{71}BM$), as suggested in Figure 5.12d. [35, 159] Moreover, at a maximum χ_{CTC}, new scattering peaks appear at 11 nm^{-1} and 16.2 nm^{-1}, indicating a stronger lattice distortion in this crystalline plane. While these features are partially masked due to F4TCNQ crystals on the surface, we can suggest they are caused by dopant residing closer to the backbone, likely by the units forming a

χ_{CTC}	Q, (100) [nm^{-1}]	d-spacing [nm]	Q, (010) [nm^{-1}]	d-spacing [nm]
neat	3.1	2.03	17.4	0.36
low	2.84	2.12	18	0.35
moderate	2.8	2.24	17.9	0.35
max	2.76	2.28	17.9	0.35

Table 5.2: Summary of the GIWAXS patterns as a function of the χ_{CTC}

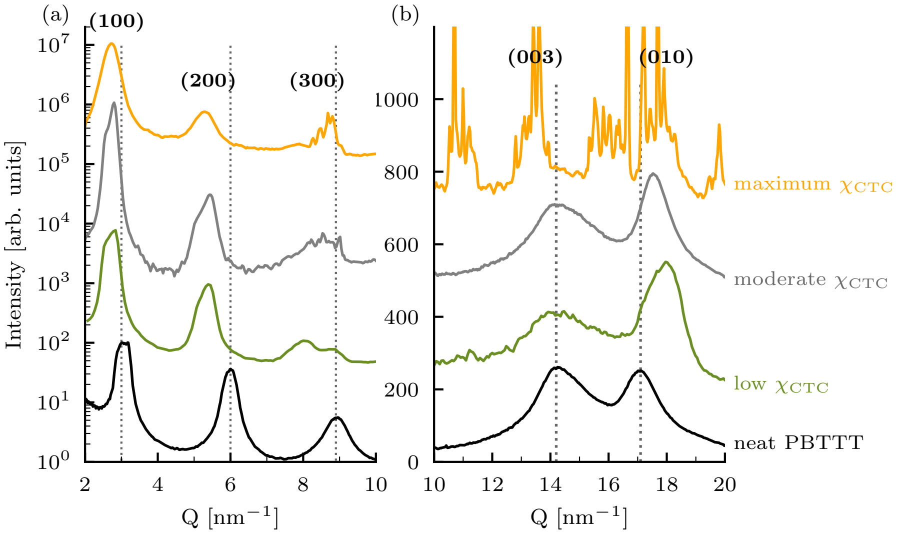

Figure 5.13: (a) Out-of-plane and (b) in-plane GIWAXS scattering patterns as a function of the CTC content. Data is scaled for clarity and vertical dashed lines are a guide to the eye for the diffraction peaks of the neat film.

CTC. Finally with these observations and the results presented with Raman and IR spectroscopy, we can suggest that the CTC resides predominantly in the crystalline region and closer to the backbone, which is further supported by two key aspects.

1. GIWAXS provides information about the microstructural changes in the *crystalline* domains. Here, we see clear signs of dopant residing in the side-chain and in a closer contact with the polymer backbone. Notably, the contraction seen in the (010) direction could indicate a slightly tilted polymer backbone which could be responsible for enhancing the $\pi - \pi$ interactions between the polymer and the dopant, and thus in promoting CTCs. Figure 5.10).

2. Raman measurements probing the crystalline region (at 785 nm) confirm the presence of dopant at all χ_{CTC} cases. However, they show a distinct vibration mode for F4TCNQ in the maximum χ_{CTC} case, that is *not* present in the other samples, likely from the CTC. (Figure 5.9a, at 350 cm^{-1}).

5.5 EXTENSION TO OTHER MATERIALS

Here we demonstrate that the TAVD method is not only confined to PBTTT but can also work in other polythiophenes hosts with similar energy levels. We selected RRa-P3HT also in combination with F4TCNQ, and then exposed the doped film to a temperature gradient for a period of 4 h. This particular host:dopant combination is known to produce modest doping levels that contain mostly IPAs,[109, 122, 131] both when processed via co-deposition and vapor doping.

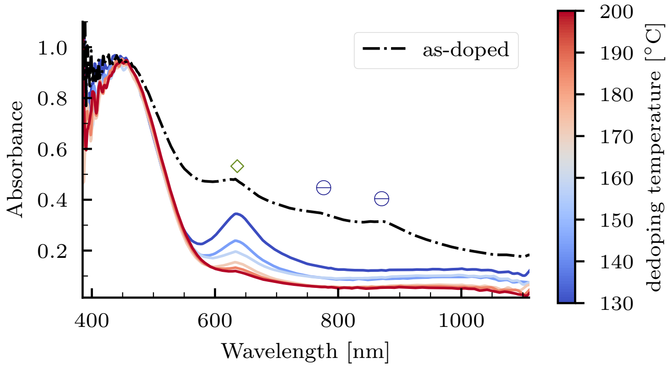

Figure 5.14: UV-Vis absorbance spectra for doped RRa-P3HT dedoped in a temperature gradient from 130 °C to 200 °C. Symbols indicate the bands for the F4TCNQ anion (⊖) and the CTC (◇)

As seen in Figure 5.14, using the conditions that lead to a moderate χ_{CTC}, we can produce a film with a clear spectroscopic signature of the CTC. Moreover, after dedoping the film we see further evidence of the greater stability in CTC state, which in this case persists until ≈170 °C.

5.6 CONCLUSIONS

In this chapter, we have presented a strategy to improve the long-term stability of doped conjugated semiconductors. We exploit the improved thermal stability of the CTCs that naturally coexists with IPAs states, but in an arbitrary composition. For this, we develop a doping method that introduces the desired amount of either charge-transfer state. We use this method to evaluate the long-term stability of samples with different contents of CTC. We demonstrate that the substantially long-term stability can outweigh the penalty in the thermoelectric properties caused by introducing a CTC. Moreover, we demonstrate that it is possible to benefit from this effect even with small CTC fractions. To further understand the origin in the enhanced thermal stability, we make a thorough characterization using Raman spectroscopy and GIWAXS. Our results suggest that expanding the polymer's lattice facilitates the diffusion of the dopant closer to the backbone and preferentially into the crystalline region.

6

DEPENDENCE OF THE THERMAL CONDUCTIVITY ON FILM MORPHOLOGY AND ELECTRICAL CONDUCTIVITY

ABSTRACT *Understanding the nature of thermal-electrical transport is crucial for the development of organic thermoelectric and electronic applications. In this section, we use a fast-screening approach to unravel the effect of crystallinity and dopant content in the thermal-electrical properties of PBTTT.*[1]

6.1 MOTIVATION

THERMAL TRANSPORT IN ORGANIC SEMICONDUCTORS Doping of organic semiconductors is crucial for developing thermoelectric and electronic applications. Different publications have addressed the effect of doping and microstructure quality on the electrical conductivity and Seebeck coefficient.[16, 35, 95] However, only a few of them have studied their effect on the thermal transport properties for the same materials. [7, 71, 160] In most inorganic materials, the inter-relationship between the electrical and thermal conductivity is better understood and, for most cases,[70] is the sum of an electronic, κ_{e} and a phonon-lattice contribution, κ_{latt} given by Equation 6.1.

$$\kappa_{total} = \kappa_{\mathrm{e}} + \kappa_{\mathrm{latt}} \tag{6.1}$$

For metals and highly doped inorganic semiconductors, κ_{e} is typically the dominant contribution ($\kappa_{\mathrm{e}} >> \kappa_{\mathrm{latt}}$) following the Wiedemann-Franz law given by Equation 6.2.

$$\kappa_e = \sigma L_0 T \tag{6.2}$$

where L_0 is the Lorenz number and typically close to Sommerfeld value of $2.44 \times 10^{-8}\,\mathrm{W\,\Omega\,K^{-2}}$. [71–73] However, it is not clear that organic semiconductors follow the same trend, given the different and sometimes contradicting results between the experimental and theoretical results reported in the literature. [16, 17, 32, 71, 72, 74, 76] Part of this problem lies in the limited experimental data where both properties are measured within a single sample.[14, 32, 74] Notably, this is a challenging task considering that each characterization technique may require incompatible sample preparation and electrode

---

[1] A large part of this chapter has been published in "Reduction of the Lattice Thermal Conductivity of Polymer Semiconductors by Molecular Doping" in *ACS Energy Letters* Zapata-Arteaga, Dörling, Perevedentsev, Martín, Reparaz, and Campoy-Quiles [149]

geometry. Moreover, fabricating different samples with varied doping levels or crystalline quality is not a straightforward process and may introduce reproducibility problems.

A GRADIENT APPROACH In Section 5.2, we introduced a methodology based on dopant gradients. Here we extend the same concept to fabricate a gradient in crystallinity. In brief, samples with a gradient in crystallinity were fabricated by annealing as-deposited films of PBTTT in a temperature gradient. The latter induces a microstructure change within the distinct phases in PBTTT.[68] Then we extract the degree of crystallinity and dopant content from the UV-Vis-NIR absorbance spectral features and calculate the thermal and electrical conductivity with local and contactless techniques i. e., FDTR and Raman spectroscopy. As seen in Figure 6.1, using this methodology offers the possibility of measuring a gamut of values for σ and κ as a function of the degree in crystallinity or dopant content.

Chapter 4 presents the methodology followed for sample processing and analysis.

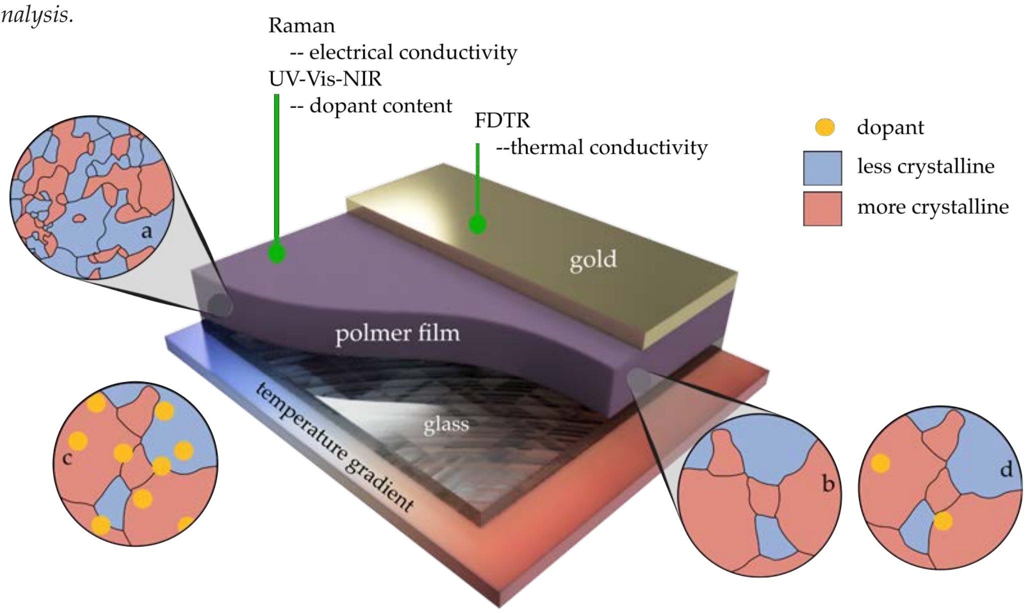

Figure 6.1: Schematic illustration of a film used for measuring the thermal and electric conductivity in films of PBTTT. Illustration depicts differences in the degree of crystallinity (a→b) or in dopant content (c→d) in the direction of the temperature gradient. Noteworthy, the annealing process used to generate gradients was done *before* the deposition of the gold transducer.

This section presents a comprehensive thermal, electrical, and microstructural characterization for two sets of samples: (i) Films of neat PBTTT with a gradient in crystallinity, and (ii) films of F4TCNQ-doped PBTTT with a gradient in dopant content, but homogeneously pre-crystallized at 180 °C. Half of the sample's surface was covered along the gradient direction with a gold transducer to measure the thermal conductivity, and the optically-accessible half used to measure the electrical conductivity and calculate the dopant content. First, we evaluated the effect of crystallinity and dopant content on the thermal conductivity by measuring both properties along the samples' gradient direction. Then we analyzed the impact of doping and annealing on the thin film's microstructure through GIWAXS analysis and AFM. Finally, we extend our study to a different material.

6.2 EFFECT OF THE CRYSTALLINITY AND DOPING ON THE THERMAL CONDUCTIVITY

As a starting point we analyze the effect of the annealing temperature on the crystallinity. Figure 6.2 presents the absorbance spectra for (a) the neat film annealed from 70 °C to 200 °C and (c) the doped one annealed from 130 °C to 200 °C. The spectra of both samples display two bands at approximately 530 nm and 600 nm. The low energy transition A_{0-0}, dominate in more the ordered and crystalline regions indicating a longer conjugation length, whereas the high energy band A_{0-1}, dominate as the material becomes more amorphous indicating. [122, 135].

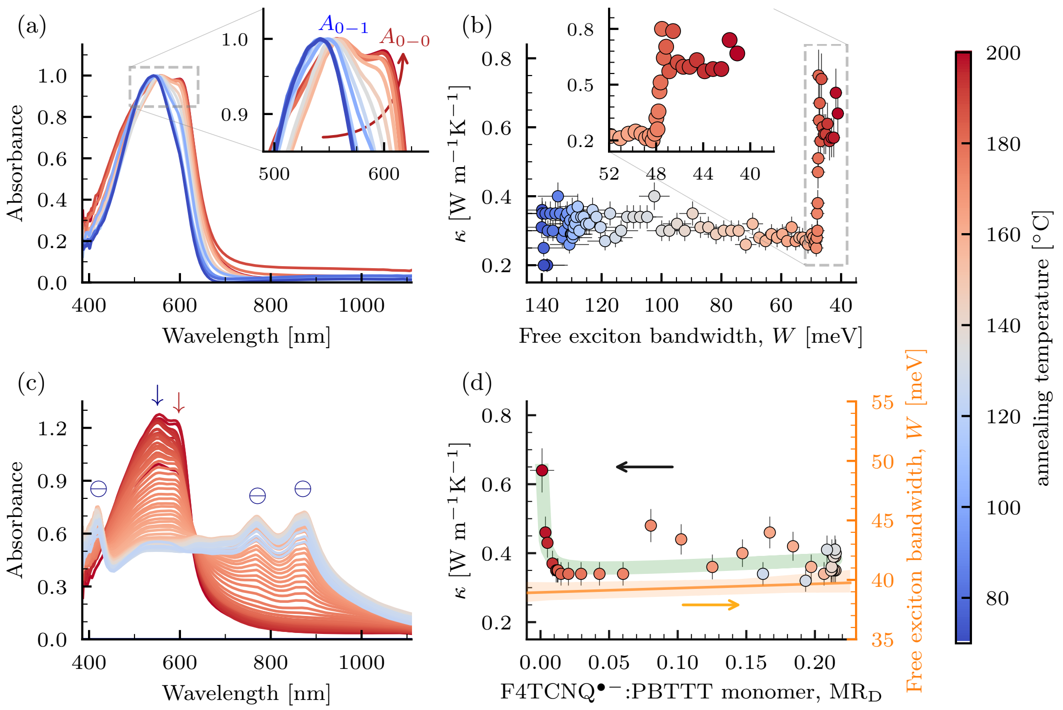

Figure 6.2: UV-Vis absorbance spectra for films of neat (a)PBTTT and (c) F4TCNQ-doped PBTTT as a function of the annealing temperature. Data in (a) is normalized to the A_{0-1} transition. (b) Thermal conductivity as a function of the free exciton bandwidth for neat PBTTT, (d) Thermal conductivity as a function of the Molar ratio of F4TCNQ (left ordinate, green line is a fit to the same data) and free exciton bandwidth as a function of the Molar ratio of F4TCNQ (right, orange ordinate).

The ratio of these peaks is related to the free exciton bandwidth, W, and has been used as a measurement for the degree of crystallinity.

[131, 133, 161] In brief, a decrease in W indicates an increase in the conjugation length and interchain order.

In Figure 6.2b we present the thermal conductivity plotted as a function the free exciton bandwidth W for the neat sample. The thermal conductivity seems to converge to around $0.3\,\mathrm{W\,m^{-1}\,K^{-1}}$ at 48 meV before drastically increasing up to $\sim 0.70\,\mathrm{W\,m^{-1}\,K^{-1}}$ within a small change in W. The latter corresponds to annealing temperatures between 160 °C to 170 °C, where PBTTT transitions into the '*terraced*' phase, characterized by larger and more ordered crystallites. [55, 65] In this scenario, we propose that the thermal transport depends on the resistance of the available percolation paths; for W values above 48 meV, there is a high density of paths with domains that vary in order and size, as in a 'series resistance model'. Then, for W below 48 meV the crystallites grow in size and share a more similar crystalline quality and start to percolate, allowing a parallel-like thermal transport, as seen in Figure 6.3. In this case, the higher conductive crystallites can effectively short-circuit the amorphous areas.

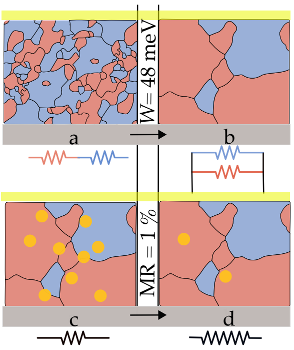

Figure 6.3: Cross-section illustration for the microstructure change in samples with a gradient in crystallinity (a-b) and dopant content (b-c).

Now we analyze the evolution of the thermal conductivity in the sample with a (ii) dopant gradient (Figure 6.2d). Here, a dopant molar ratio ($\mathrm{MR_D}$) as low as $\approx 1\%$ reduces the thermal conductivity from $0.65\,\mathrm{W\,m^{-1}\,K^{-1}}$ to $0.35\,\mathrm{W\,m^{-1}\,K^{-1}}$. For $\mathrm{MR_D} > 1\%$, κ remains around $0.35\,\mathrm{W\,m^{-1}\,K^{-1}}$ with only a few values out of the trend which we attribute to dopant crystals on the surface, as seen in Figure 6.4. Notably, W in this sample stays constant around $\sim$40 meV, indicating that the crystalline quality does not deteriorate when doping through the vapor-phase, as suggested by Kang et al. [62]

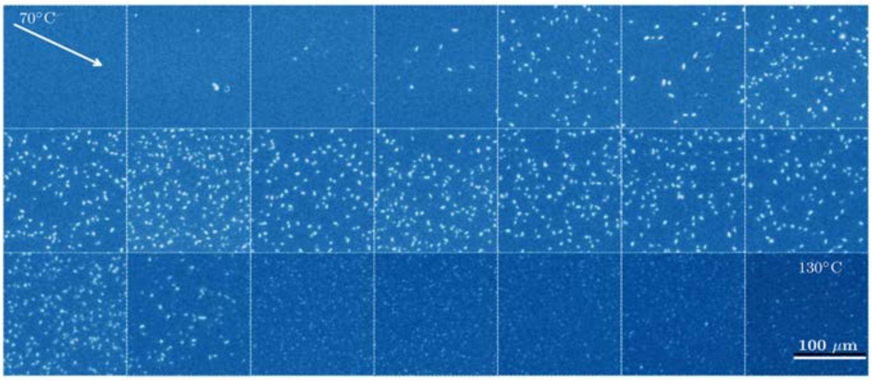

Figure 6.4: Micrographs taken under transmitted-light for the dedoped sample depicted in Figure 6.2. Darker tones of blue indicate a higher temperature used for dedoping. A pseudocolor was applied to enhance the contrast of the crystals. Temperature difference between each micrograph is ≈3 °C

We highlight that films with a dopant gradient are pre-crystallized at 180 °C, and should not change drastically as a consequence of the secondary annealing used for dedoping. Therefore, we expect that the observed changes in κ are due to the presence of dopant and not from a temperature-induced crystallization as in Figure 6.2b. One could expect, that in the present case, the thermal resistance should decrease, due to the additional electronic contribution to the thermal conductivity, as represented in Equation 6.2. Instead, doping increases the thermal resistance within the crystalline domains, resulting in a lower total thermal conductivity. Remarkably, a similar effect denoted as *alloy-scattering* has been observed in inorganic materials, where a small amount of a secondary material lowers the thermal conductivity of the bulk due to increased disorder. [162, 163]

These observations would suggest that dopant is located within PBTTT crystallites, thus not drastically altering the crystalline quality but inducing a partial disorder in the lattice. Moreover, we can suggest that for the doping level achieved in the previous sample, κ_{latt} is the dominant contribution.

6.3 MICROSTRUCTURE ANALYSIS

Grazing Incidence Wide-Angle X-ray Scattering (GIWAXS) allowed us to investigate the impact of annealing and doping on the solid-state nanostructure. Figure 6.5 presents the out-of-plane and in-plane scattering patterns for the (i) neat and (ii) doped sample for selected processing conditions.

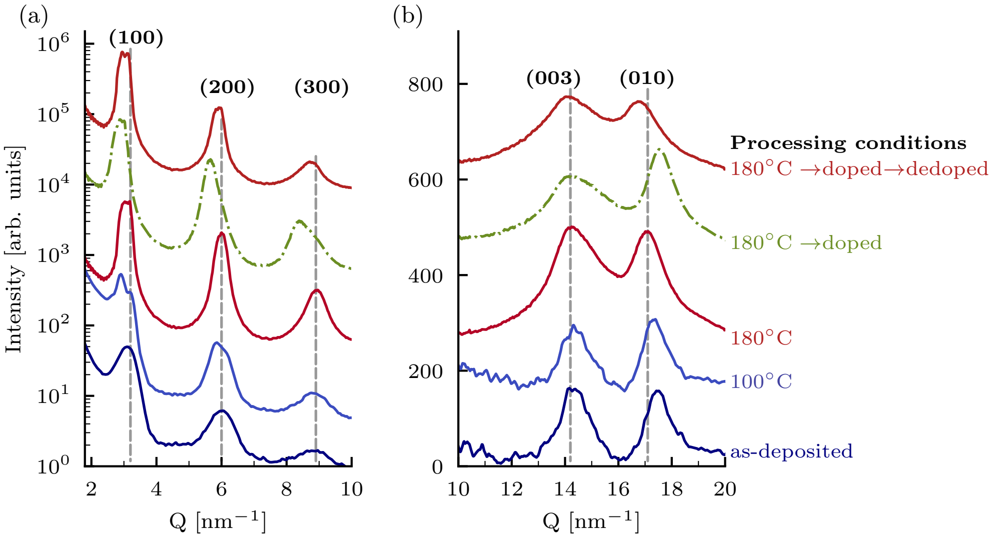

Figure 6.5: (a) out-of-plane and (b) in-plane GIWAXS scattering patterns for; the neat as-deposited film, neat annealed at 100 °C, neat annealed at 180 °C, annealed at 180 °C and doped, and annealed at 180 °C doped and then dedoped. Data is scaled for clarity and vertical dashed lines are a guide to the eye for the diffraction peaks in neat film annealed at 180 °C the .

First we analyze the evolution of the neat film with thermal annealing. Here we highlight a shift of the (100) and (010) diffraction peaks towards lower scattering vectors, thus indicating an expansion of the lattice in the lamellar- and $\pi - \pi$ stacking direction. Additionally, we observe a progressive narrowing of the (100) peak, indicating an improved ordering in the lamellar packing. The latter is due to the melting and cooling of the sidechains, allowing them to adopt a more extended vertical and interdigitated configuration. [65, 68] These observations are in agreement with the evolution of the free exciton bandwidth and thermal conductivity presented in Figure 6.2, further supporting a phase transition i. e., as-deposited→*terraces*.

On the other hand, and as presented in Section 5.4.2, doping through the TAVD method induces two significant changes i. e., an expansion in the (100) direction and a contraction in the (010) direction. We ascribed these changes to the placement of dopant within the lamellar region and a tilt in the conjugated core, that allows a closer packing. Here, additional analysis of the rocking curves for the (100) reflection (see Figure 6.6), demonstrates a larger FWHM for the doped sample, thus less ordered when compared with the neat film processed at the same temperature. Finally, dedoping induces a recovery of the characteristic peak positions observed in a neat film annealed at 180 °C, and thus suggests a reversible process. This trend is also observed in the evolution of the FWHM for the rocking curves presented earlier.

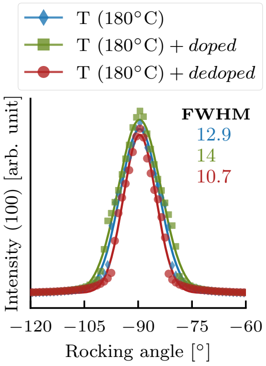

Figure 6.6: Rocking curves for the (010) reflection. A lower FWHM indicates a larger population of crystals parallel to the substrate.

Additional analysis using AFM illustrates that annealing thin films of PBTTT changes the morphology from a nodule-like structure and into relatively large and highly ordered domains typically referred to as *terraces*. [55, 65] These terraces grow vertically due to sidechains melting, extending, and adopting a fully extended conformation with relatively few gauche defects. [65] The latter also allows the backbone to adopt a more vertical layer structure and grow in lateral size. [55, 65, 68] These changes have been correlated with an increase in carrier mobility due to an improved $\pi - \pi$ stacking and backbone orientation relative to the as-deposited films. [55, 65, 67, 68] Previous observations also agree with the shift of the (100) scattering peak shown in Figure 6.6a.

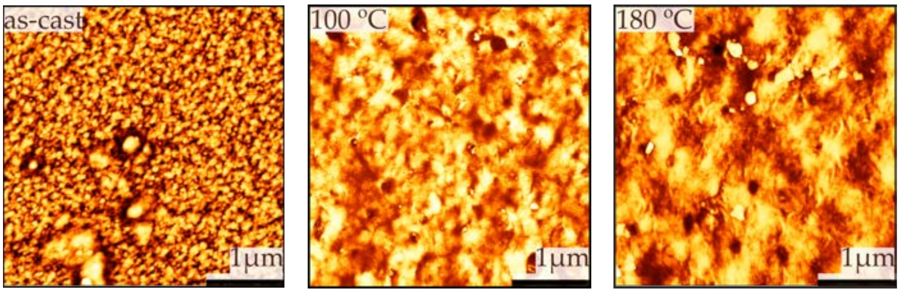

Figure 6.7: AFM topography images of PBTTT. Images were acquired at distinct positions of the gradient of sample (i).

The results in this section indicate that κ increases for a $\mathrm{MR_d} < 0.01$ due to a recovery of the neat-state of PBTTT. Additionally, they further suggest that doping does not deteriorate the degree of crystallinity of the film, i. e., no new diffraction peaks appear. Instead, induces a slight disorder in (100) direction when compared with the neat film.

6.4 EFFECT OF THE ELECTRICAL CONDUCTIVITY ON THE THERMAL CONDUCTIVITY

Herein we study the relationship between the electrical and thermal conductivity for the doped sample depicted in Figure 6.2. This will allow us to understand the weight of the electronic contributions and assess the applicability of the Wiedemann-Franz law. To calculate the electrical conductivity, we employed a contactless analysis based on Raman spectroscopy, which was first introduced for calculating σ in films of PBTTT doped with the Lewis acid BCF. [146] In brief, this method utilizes the known relationship between the intensity ratio r_R of given Raman peaks and the electrical conductivity at a given doping level. Figure 6.8 demonstrates that applying this method in combination with gradients, can provide a gamut of '*samples*' within a single film.

Further details for the calculation of σ from the Raman spectrum are in Section 4.3.3

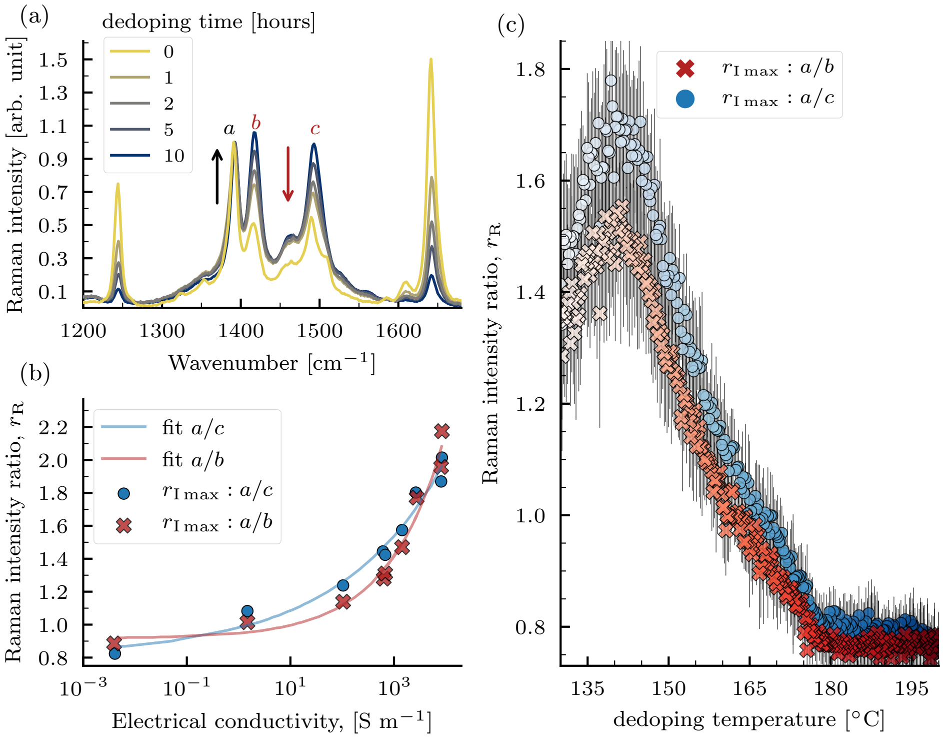

Figure 6.8: (a) Reference Raman spectra used for calibration. Data corresponds to a series of dedoped films presented in Chapter 5. (b) Calibration curve obtained from the reference measurements. (c) r_R Raman map for the dedoped film depicted in Figure 6.2.

Figure 6.9a presents the electrical conductivity as a function of the dopant content. We observe a superlinear increase in σ with small

$MR_d < 0.03$, which then reach values as high as 6800 S m^{-1}. This trend and the range of values are within reasonable agreement with those reported for similar materials and processing techniques. [35, 130, 155] Additionally, we observe two data branches in σ for $MR_d > 0.15$. We attribute this change to an improved dopant diffusion between 130 °C to 145 °C, which is also observed in Figure 6.8c.

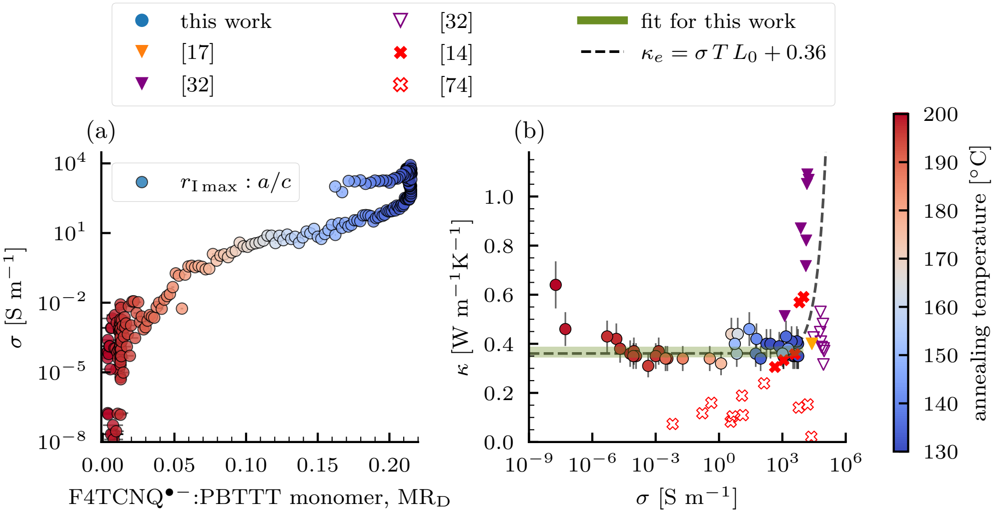

.

Figure 6.9: (a) Electrical conductivity as a function of the dopant Molar ratio. (b) Thermal conductivity as a function of the electrical conductivity. Green line is a fit on the experimental data using Equation 6.1 and Equation 6.2. Dashed line is a model using $\kappa_{total} = \sigma L_0 T + 0.36$. For comparison, doped films of PEDOT (inverted triangles) and PANI (crosses).

In Figure 6.9b, we present the thermal conductivity as a function of the electrical conductivity. In order to compare our data, we include measurements from the literature for doped poly(3,4-ethylenedioxythiophene) (PEDOT) [32] and polyaniline (PANI) [14, 74]. We also include a model using Equation 6.1 and Equation 6.2 with the Sommerfeld value as an approximation for the Lorenz number and a lattice contribution of 0.36 W m^{-1} K^{-1}. First we highlight the differences in κ for doped PEDOT and PANI reported in literature. For most of these examples, σ and κ were measured from different samples or processed differently depending on the characterization technique. Arguably, the latter can lead to some uncertainty in the values measured.

For our experiments, we observe that after an initial decrease at low σ values, κ stays rather constant from 10×10^{-5} S m^{-1} to 10×10^{3} S m^{-1} which is somewhat unexpected. However, our films don't reach values of σ capable of introducing a significant electronic contribution. Nonetheless, fitting the experimental values to Equation 6.1 indicate a lattice contribution of 0.36 W m^{-1} K^{-1}, and therefore lower to what was measured for highly crystalline neat PBTTT.

The latter suggest a strong scattering effect introduced by the dopant, even though the degree of induced disorder is relatively small (cf. Figure 4.14). Another rationalization for our results is the fact that observations doped organic semiconductors operate in the so-called *'impurity reserve regime'* [155] where dopant content is typically in the order of several weight %, but only a fraction actually contributes to charge carrier generation.

6.5 EXTENSION TO OTHER MATERIALS

To inquire more about our findings, we exposed films of PTB7-Th to the same doping process as PBTTT and then to a temperature gradient. We measured the evolution of the UV-Vis-NIR spectral features and the thermal conductivity as a function of the dedoping-temperature, as seen in Figure 6.10. In this scenario, there is no charge-transfer between the polymer and the dopant, due to the mismatch of their HOMO and LUMO energy levels, and reflected by the absent bands associated to the F4TCNQ anion at 416 nm, 790 nm and 890 nm. Nevertheless, we presume that dopant is still able to infiltrate within the material, given that at low dedoping temperatures the thermal conductivity (higher dopant content) is lower than those values corresponding to higher temperatures (lower dopant content)). This results indicate that charge-transfer is not a parameter leading to a decreased thermal conductivity but the presence of foreign molecules that act as scattering centers.

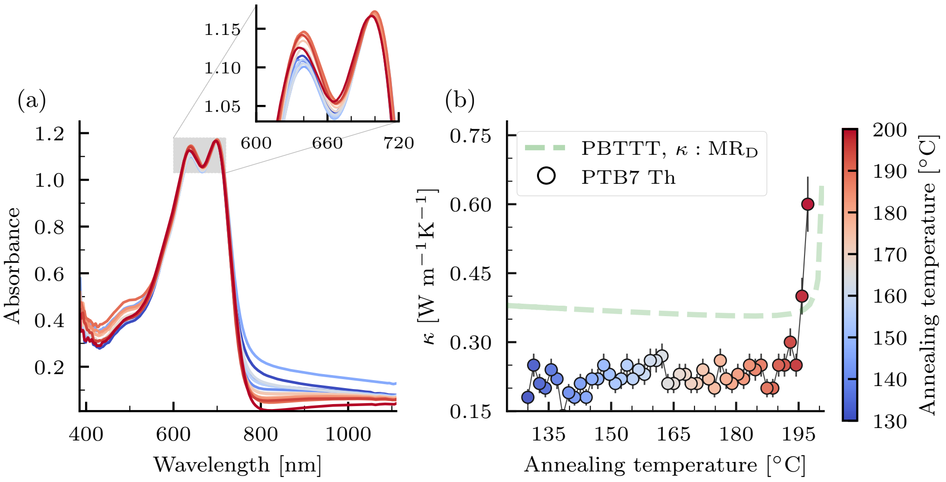

Figure 6.10: (a) UV-Vis-NIR absorbance spectra for films of PTB7-Th exposed to F4TCNQ (b) Thermal conductivity for the same sample after exposure to a temperature gradient.

6.6 CONCLUSIONS

From the presented results, we rationalize that the differences observed in κ between the doped and neat polymers are due to the following; κ benefits from a high degree of crystallinity, likely due to an increase in the phonon mean-free path. Then, doping the polymer film results in a significant decrease in the thermal conductivity. Noteworthy, even when doping from the vapor-phase induces a slight disorder when compared with the neat film (as seen in Figure 6.6). Finally, these observations suggest that thermal transport, at least for the studied material is dominated by disorder, comparable to what is commonly referred to as *'alloy scattering'* in inorganic materials.

7

DEPENDENCE OF THE THERMOELECTRIC PROPERTIES ON THE MORPHOLOGY OF POLYMER BLENDS

ABSTRACT *This chapter explores techniques to enhance the electrical conductivity and Seebeck coefficient simultaneously. In particular, our approach employs polymer-polymer mixtures to enhance the film's order and microstructure quality, thus improving the charge transport characteristics in the film.*

7.1 MOTIVATION

CURRENT TRENDS Chapters three and four describe organic thermoelectric materials in terms of a polymer host and a small-molecule dopant. Novel, alternative approaches employ polymer-polymer mixtures to improve the thermoelectric stability and performance. In this chapter, we document two successful examples.

DOS ENGINEERING This concept, which was first introduced by Mahan and Sofo and then developed by Sun et al., is based on the idea that that the Seebeck coefficient increases as greater proportions of the electrical conductivity occur at energetic levels away from the E_F. [42, 81] In a Gaussian-shaped DOS describing the HOMO and LUMO, charge transport occurs through a characteristic hopping event between the E_F and the E_{tr}. In such case, the Seebeck coefficient is given by $S = (E_F - E_{tr})/T$. E_F is located between the HOMO and LUMO and shifts towards the DOS upon doping, thus depends on the charge concentration and dopant concentration. [61] The E_{tr} is the critical energy for a carrier to contribute to the conductivity starting from E_F, and depends on a trade-off between the cost of hopping in real space and hopping in energy space. Consequently, increasing the gap between E_F and E_{tr} directly affects the Seebeck coefficient. [41, 80] Within this framework, Zuo et al. utilized F4TCNQ-doped RR-P3HT mixed with varied fractions of a 'guest' polymer of deeper HOMO energy, namely, poly[[2,3-bis(3-octyloxyphenyl)-5,8-quinoxalinediyl]-2,5-thiophenediyl] (TQ1). As a result, at an optimal composition ratio, the binary mixture possesses a double peak DOS (as illustrated in Figure 7.1) with E_F located in RR-P3HT but E_{tr} shifted towards the TQ1 due to a change of the percolating path. The resulting Seebeck coefficient is a local maximum that exceeds that of both pristine materials.[41] Nevertheless, the unfavorable alignment between the HOMO of TQ1 and the LUMO in F4TCNQ limited charge carrier formation.

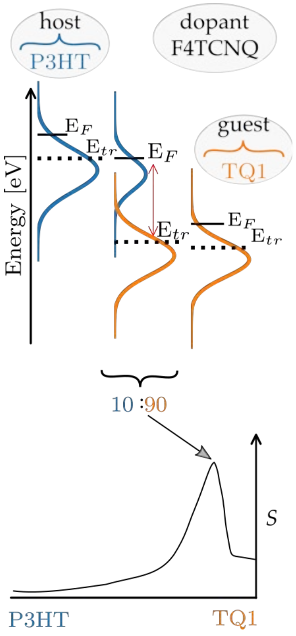

Figure 7.1: Illustration of the DOS engineering method from reference [41].

Thus, the increase in S went hand in hand with a considerable drop in electrical conductivity, compared to the single-component host analog.

GROUND-STATE ELECTRON TRANSFER A typical n- and p-type doping process generates only one mobile charge carrier. The remaining immobile counter charges often lead to a detrimental effect on microstructure and carrier mobility. As an alternative, Xu et al. showed all-polymer donor-acceptor heterojunctions, comprised of polymer semiconductors where the EA of the acceptor matched the IE of the donor (the materials are shown in Figure 7.2 for reference). The resulting films generated both p- and n-type polarons induced by the charge transfer within the material's interfaces. The combined hole and electron distributions allowed for a high charge concentration and electrical conductivity of up to five orders of magnitude higher than that of the pure components. On the other hand, the Seebeck coefficient varied from negative to positive with the composition's weight ratio. [26] Their films also possessed high thermoelectric stability under continuous thermal stress, given that they contained no small-molecule dopants prone to sublimation.

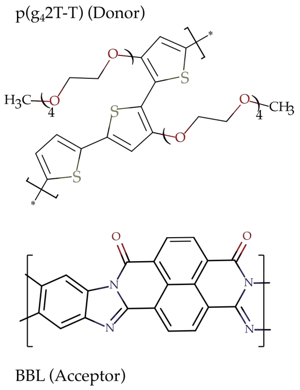

Figure 7.2: Chemical structures for the materials utilized in reference [26]

Inspired by the DOS approach and current interest towards polymer-polymer mixtures, [26, 41, 82, 164–166] we explored mixtures of PBTTT with RR-P3HT as the guest. Thus, providing two materials with a similar affinity towards the LUMO level of the dopant (F4TCNQ), as seen in Figure 7.3. Here we present a study of the thermoelectric and structural properties of pure PBTTT (hereafter the 'reference') and PBTTT mixed with varying weight fractions (χ) of RR-P3HT(hereafter P3HT). All films were annealed at 180 °C and doped with F4TCNQ using the TAVD 'moderate' method detailed in Chapter 5 and in Section 4.2.3

To speed up the preparation, and have a larger pool of comparable samples, films were fabricated with a gradient in thickness. Thus, providing additional 'samples' and information about thickness-dependent effects, e. g., improved dopant diffusion or induced-ordering at the substrate interface. We used UV-Vis-NIR spectroscopy to quantify the generated charge-transfer species in the film, then, AFM and GIWAXS to analyze the changes in the microstructure as a function of χ_{P3HT}. As key findings, we identify a combined induced-ordering effect in the crystalline domains, driven by the added P3HT and by doping. After hypothesizing the reason behind the induced-ordering effect, we extend our study to a set of different polymer:polymer systems.

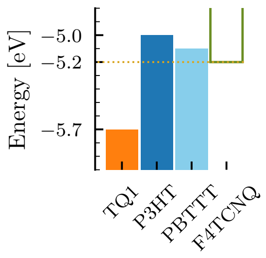

Figure 7.3: Energy levels for TQ1, P3HT, PBTTT and F4TCNQ.

7.2 THERMOELECTRIC CHARACTERIZATION

Figure 7.4 presents the thermoelectric properties dependent on the active layer composition, measured at different points within the thickness gradient. First we highlight two apparent regimes observed in the electrical conductivity; between (i) 5 % and 15 % and above 15 % (Figure 7.4a). In the first case (i), sigma starts at a lower value compared with the reference (r) , that is, $\sim$14 S cm^{-1} at 5 % and then increases up to $\sim$100 S cm^{-1} for χ =15 %. Within the same regime, we observe a

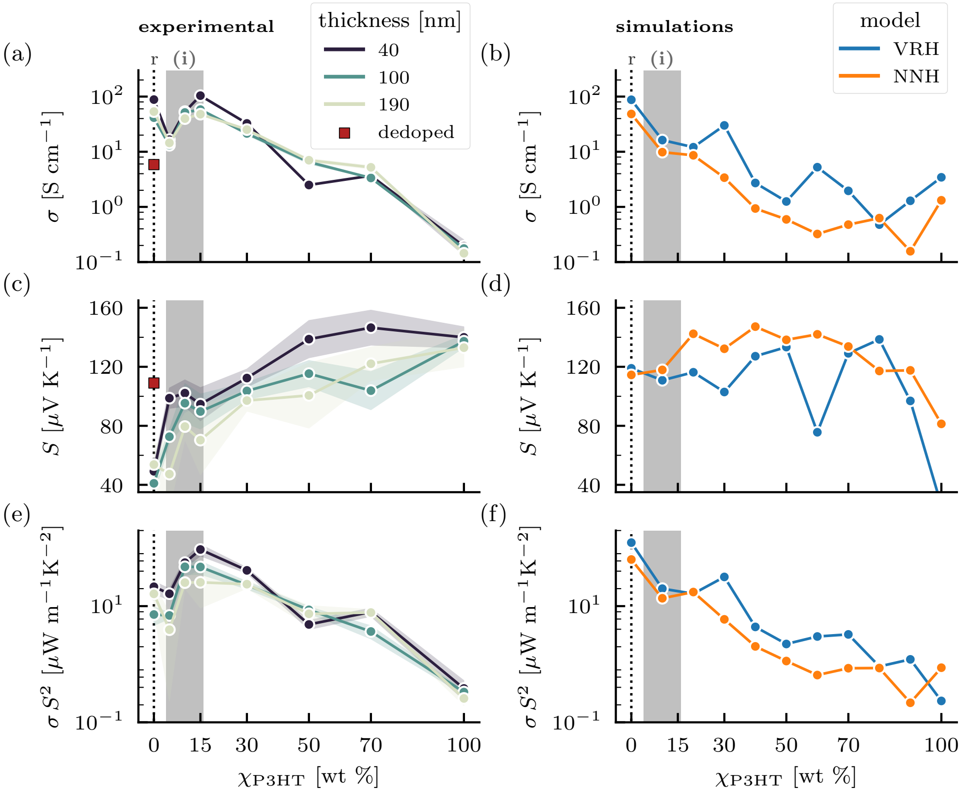

Figure 7.4: Experimental and simulated thermoelectric properties of F4TCNQ-doped PBTTT as a function of distinct loads of P3HT. (a,b) Electrical conductivity, (b,c) Seebeck coefficient and (c,d) power factor. Experimental data represents the mean value of four measurements taken along the thickness gradient and the shaded band the standard deviation of those values. The simulated thermoelectric properties utilized numeric kinetic Monte Carlo with a variable range hopping (VRH) and nearest neighbor hopping (NNH) model[a]. Dedoped marker belongs to the data presented in Chapter 5

two-fold increase in the Seebeck coefficient. These values are typically not reached by the PBTTT reference unless it is dedoped, and thus, characterized by a significant loss in σ. In the second regime, further addition of the guest decreases the electrical conductivity by almost three orders of magnitude and increases the Seebeck coefficient by

---

[a] kinetic Monte Carlo simulations were done by Dr. Guangzheng Zuo and Dr. Martijn Kemerink. (Linköping University, Complex Materials and Devices).

approximately a factor of three compared to the reference. Although σ at χ =15 % is not significantly different from that of the reference's value, the squared relationship with S leads to a higher power factor in the 15 % composition than in the reference.

Arguably, the peak performance found at χ =15 % mimics to a lesser degree the effect seen by Zuo et al. [41] Yet, we highlight that the nearby lying energy levels in P3HT and PBTTT are non ideal for creating a double-peak DOS, as seen in Figure 7.3. Nonetheless, to further evaluate such a scenario, we performed kinetic Monte Carlo simulations, which adequately capture the fundamental physics governing the thermoelectric properties in doped conjugated polymers. [41] Monte Carlo simulations (see Figure 7.4) using a NNH and VRH models evidence a monotonous decrease in conductivity with increasing P3HT content and a relatively insensitive thermopower. In other words, the simulations cannot reproduce the experimental results, suggesting that the improved thermoelectric performance has a distinct origin.

Notably, the observed trends do *not* resemble either a pure blending effect, i. e., a linear combination of the Seebeck coefficient of the constituents weighted by their electrical conductivity. [41, 160] A possible way to rationalize our results is by invoking structural changes associated with blending. We want to highlight that our observations appear to be thickness-independent in such a case (cf. experimental values for different thicknesses), suggesting that the guest material drives this change and not, e. g., a thickness-induced ordering effect, as previously seen for thin films of PBTTT. [167] In the context of microstructure, the two regimes could derive from the combination of several effects.

1. For the first regime, a simultaneous increase of the σ and S values can be a product of a decrease in the anion concentration and an increase in carrier mobility when introducing small amounts of P3HT. Upcoming sections aim to answer if these conditions take place.

2. The second regime might be explained as a transition of two different percolating networks. For instance, between 15 % and 50 % we can imagine that charge transport is dominated by doped PBTTT due to the large mobility difference between the two materials. Above 50 % the system transitions from the less interconnected clusters of doped PBTTT, and into the less conductive doped P3HT network.

7.3 INTERPLAY BETWEEN GUEST LOAD AND CHARGE-TRANSFER SPECIES

To evaluate potential differences in doping level or mechanism upon polymer:polymer blending, and to clarify the significance of the generated charge-transfer species in the doped films, we measured the UV-Vis-NIR absorbance spectra (Figure 7.5a) and fitted the characteristic bands for the F4TCNQ anion and the CTC.

Figure 7.5b,c present the analysis obtained from the fitted spectra, and Figure 7.5d the thermoelectric properties introduced earlier reproduced here for comparison. First, we point towards the band's intensity analysis and the electrical conductivity. The first noteworthy observation is that I_{CTC} is higher than the reference for the polymer mixtures. Additionally, the highest I_{CTC} fitted values, (at χ =5 % and 50 %) coincide with a drop in σ, likely to the less efficient free-carrier generation from CTCs, as discussed in the literature [108] and in Chapter 5.

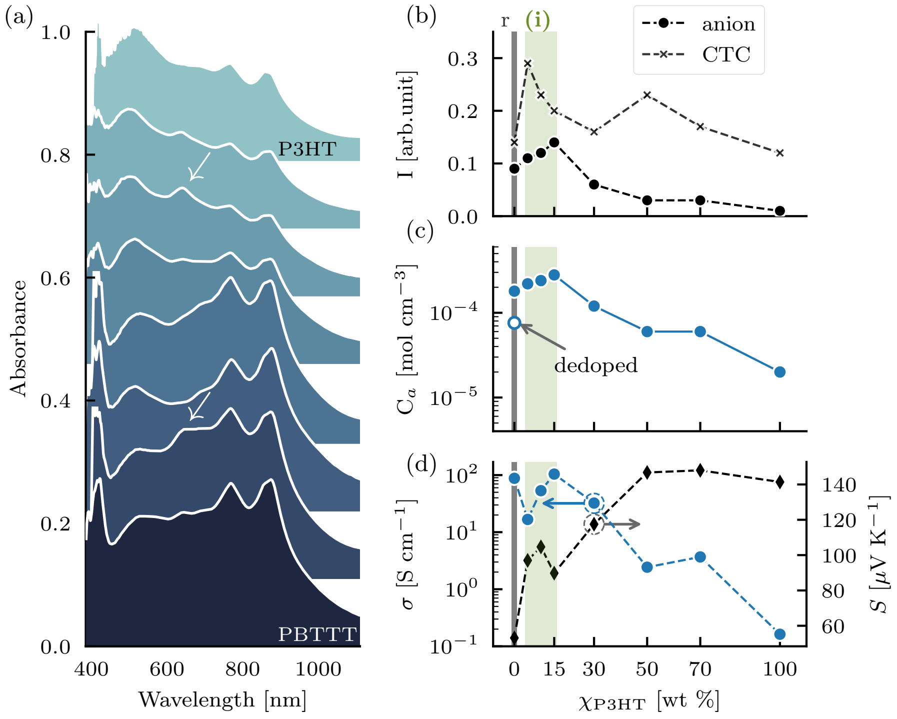

Figure 7.5: (a)Evolution of the UV-Vis-NIR absorbance spectra of doped PBTTT with distinct loads of P3HT. (b) band intensity for for the F4TCNQ anion (790 nm) and the CTC (630 nm). (c) Calculated F4TCNQ anion concentration and (d) measured electrical conductivity for the 40 nm films introduced in Figure 7.4.

Alternatively, I_{anion} increases linearly for fractions between 5 % and 15 %, which corresponds to a $\sim$50 % increase in the anion concentration (C_a) compared with the reference material, and ~ 3.5 times higher than the dedoped-reference. In principle, this would suggest that the charge carrier density in the film is higher for the blends compared to the pristine PBTTT. However, at this stage, we cannot say if charges are located in the polymer that dominates charge transport at these loadings (PBTTT) or also within P3HT domains.

Estimating the C_a from the absorbance spectra indicates anions distributed within the entire blend, but this method lacks the sensitivity to distinguish which percentage is contained in a specific polymer fraction due to the spectral overlap between the features associated to the two polymers. Thus, it is possible that a portion of the generated charge-transfer species originates from P3HT and that we overestimate the *effective doping level* in the dominant percolating network (PBTTT). We can speculate that P3HT is easier to dope based on numerous evidence. The first one is that when using the current doping conditions, P3HT generates a larger fraction of CTC than PBTTT, and a large increase in CTC is precisely what is observed upon blending. An additional argument is the following: amorphous domains have a more abundant, easier-to-oxidize distribution of states for an integer charge transfer (ICT) process than the crystalline domains.[104, 109] As these easier-to-oxidize states saturate with dopant, F4TCNQ proceeds to populate the remaining sites primarily through CTC formation. [104, 109] In this sense, we could expect doped fractions of P3HT in the fitted anion concentration. The second regime can be explained with the observed decrease in the total charge carrier density for larger fractions of P3HT, which naturally reduces the electrical conductivity and increases the Seebeck coefficient.

7.4 MORPHOLOGY AND MICROSTRUCTURE ANALYSIS

There is a strong dependence of the electrical transport on the structural order in doped films of PBTTT. In particular, σ changes drastically with the crystalline domain size, their interconnectivity, and the correlation length of the $\pi - \pi$ conjugated core. [35, 67, 132, 167] At the same time, the previous parameters can vary significantly with processing, e. g., with the deposition and annealing temperatures, substrate functionalization, or rubbing. [35, 59, 65] The next two sections aim to identify changes in the morphology and microstructure between the reference and the polymer blends. For this, we employ two characterization techniques. (1) Bimodal AFM, which provides a simultaneous outlook of the topography, mechanical and current-conductive characteristics —while (2) GIWAXS will be used to assess changes in the polymer's lattice.

7.4.1 *Morphology analysis*

Bimodal AFM is a useful technique for simultaneously mapping the topography and nanomechanical properties of polymer surfaces. For instance, Garcia and Proksch used this technique to identify phase segregation in films comprised of polypropylene (PP), polyethylene (PET) and polystyrene (PS) based on their distinct tensile strength values. [168] For our experiments, we additionally couple a current amplifier to obtain a current map within the same measurement.

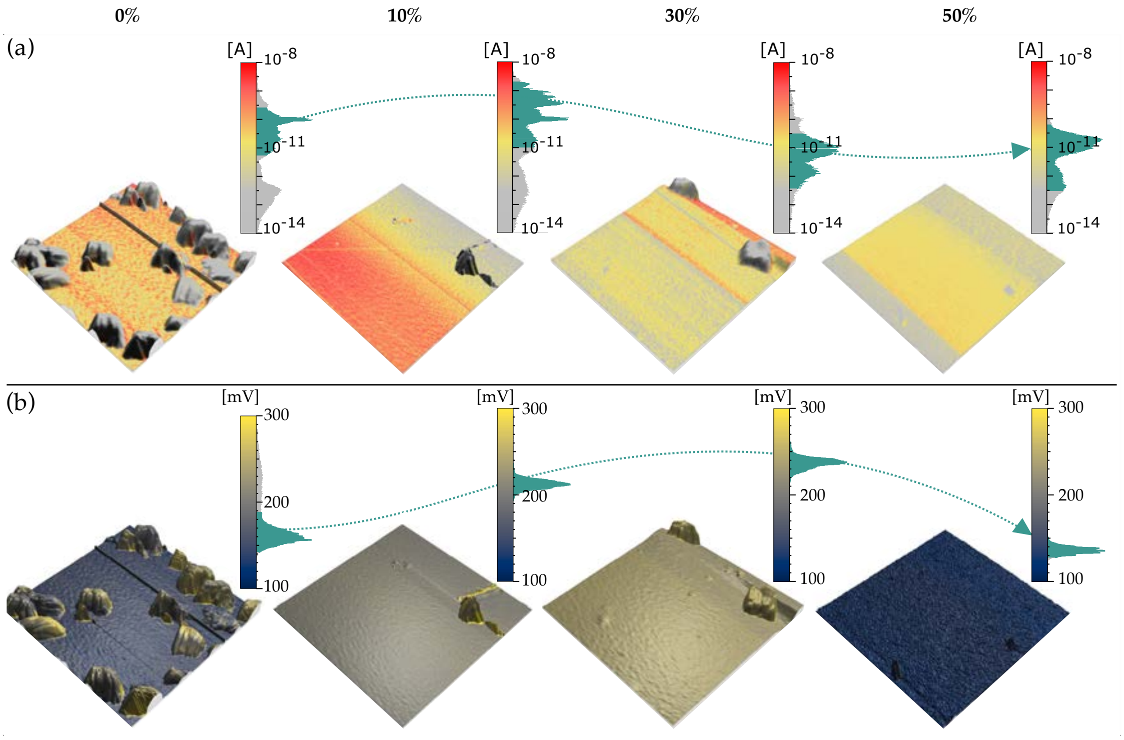

Figure 7.6: (a) Current and (b) mechanical AFM images overlaid on a 3D AFM topography map. The corresponding histograms are shown on the right side of the colorbar. Measured area is 20 µm × 20 µm

Figure 7.6 shows the 3D topography images with an overlay of the current and mechanical measurements. Here we highlight the presence of large agglomerates on the surface of the reference sample. These agglomerates are ∼700 nm high and 2 µm wide. Due to their lower electrical conductivity and increased hardness (indicated by larger values on the color scale) compared to the flat surface (cf. panel a and b), we ascribe them as neutral F4TCNQ accumulated during the vapor-doping process. Interestingly, the films with added P3HT show fewer of these aggregates, even though the doping conditions are identical for all samples. The latter may indicate that the polymer blends have a larger dopant uptake-capacity than the reference material, as the UV-Vis-NIR analysis of doped species also suggested. Aditionally, the current AFM images show a good agreement with the macroscopic electrical measurements presented earlier. By adding 10 % of P3HT, the measured current values at the film increase slightly compared with the reference. Further addition of P3HT induces a gradual decay of the conductivity.

The mechanical measurements, excluding the agglomerates, show a narrow distribution of recorded values and a homogeneous color contrast in the flat surface. The latter can suggest that P3HT is well mixed within the PBTTT matrix, at least for the compositions studied. We also observe a stiffer character for PBTTT than P3HT, in good agreement with previous reports. [169] However, we highlight that the mechanical characterization is only qualitative, as we did not measured a distinct reference material to correlate the measurement to an actual tensile strength value. As for polymer mixtures, we can only speculate they become stiffer than the neat starting material due to F4TCNQ infiltrating into the free volume of the polymer, reducing the segment motion and essentially vitrifying the material. [170]

In Figure 7.7 we analyze a smaller area of the topography from the samples shown earlier. Here, the reference sample exhibits a layered structure typically referred to as 'wide terraces.' [55, 132, 167] These terraces, show lateral dimensions that range from 200 nm to 1000 nm and step heights from 2 nm to 6 nm, which agrees reasonably well with previous reports. [68, 167]. Noteworthy, in this configuration, we do not observe a preferential orientation as seen by the processed 2D image.

Alternatively, the doped polymer mixtures present a layered slabs-like configuration. These slabs have a dimension between 80 nm to 200 nm in width and up to a couple of microns in length. These structures appear to be oriented (along the horizontal axis), yet, they become less coherent and more textured for the 30 % and 50 % compositions compared with the 10 % sample. Strikingly, these structures resemble the more ordered ribbon phase of PBTTT attained when reaching higher temperatures (240 °C). The ribbon configuration is characterized by orienting along the fluid direction during deposition, with polymer chains that fully extend across the ribbon's width. [55, 132, 167] For the material used in this work, this value is expected between 100 nm to 120 nm , which coincides reasonably well with the width measured for polymer mixtures and the pure ribbon phase of PBTTT (100 nm to 150 nm). We highlight that the polymer blends are annealed at the same temperature as the reference, i. e., *well below* the temperature required for a transition into the ribbon phase of pure PBTTT. Thus, the observed morphology can be attributed to an effect of the added P3HT fraction.

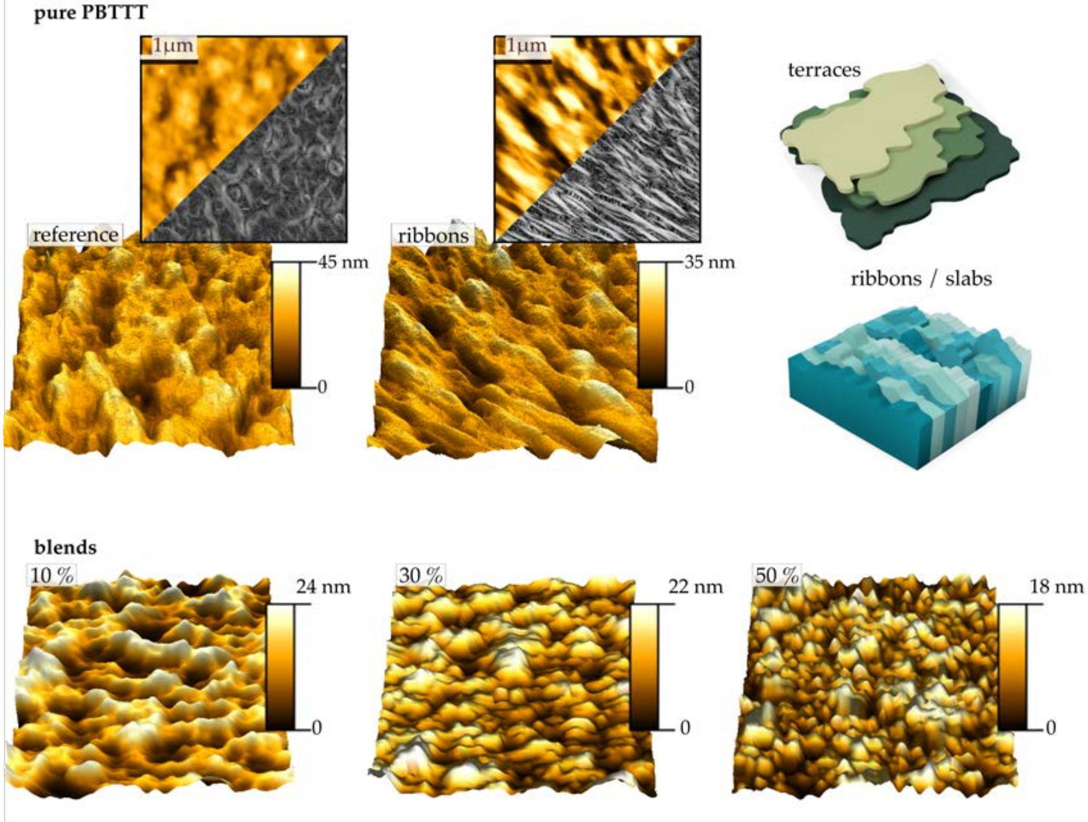

Figure 7.7: 3D Small area AFM topography images for the measurements shown earlier. Shown area is a 4 µm × 4 µm. For comparison, we include the topography of a pure PBTTT film with a typical ribbon structure. Insets in the reference and ribbon images show the 2D topography along the same image processed with a step edge filter (gray scale)[a] An illustration of terrace and ribbon structures is also included for comparison.

---

[a] The edge detection filter generates two lines; at the bottom and at the top of the step. The images where processed using a mean squared edge filter using the Gwyddieon software along the OpenCV libraries in Python

It is worth noting that the phase transition of terraces → ribbons in pure PBTTT occurs when the material gains enough molecular motion to rearrange and provide a template upon re-crystallization.[68, 167] The latter leads us inevitably to think of P3HT acting as a *plasticizer*, thus increasing the host's free volume, segment motion, and effectively giving the polymer mixtures the required mobility to rearrange in a ribbon-like structure, albeit at a lower temperature. [171] We can consider the previous assumption, provided that glass transition of a polymer blend (T_g^{blend}) follows Fox's equation given in Equation 7.1

$$\frac{1}{T_g^{blend}} = \frac{W_1}{T_{g1}} + \frac{W_2}{T_{g2}} \tag{7.1}$$

where T_{gx} is the glass transition of the pure components and W_x is their respective weight fractions. In this framework, the 15 % composi-

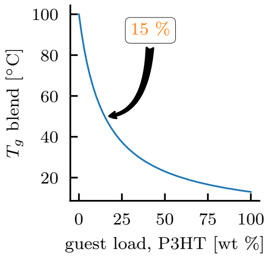

Figure 7.8: T_g of the polymer blend assuming Fox's equation. The glass transition of the pure materials are extracted from references [172]

tion has a T_g^{blend} value that is half of the reference, as seen in Figure 7.8. [170, 173]

We note that Fox's equation fails to describe all the parameters involved in estimating the glass transition of binary polymer compositions and that other more accurate and complex models are available. [173] Nonetheless, this is our current working theory, and future work will aim to measure the glass transition of the neat and doped materials experimentally. We also note that P3HT can form fibril-like structures that share certain characteristics with the presented images. Nonetheless, P3HT lacks interdigitated sidechains necessary to form coherent, vertically adjacent layers, such as the layered slabs seen in our samples. [68]. Therefore, we can suggest that the morphology found in the polymer blends is driven by the presence of P3HT.

The possible impact of the structural order on the charge transport properties of PBTTT is notorious and well described in references [65, 167, 174]. In a nutshell, the FET mobility reported for the pure material varies from $0.1\,\mathrm{cm^2\,V^{-1}\,s^{-1}}$ to $1.6\,\mathrm{cm^2\,V^{-1}\,s^{-1}}$ for the as-deposited and ribbon phase, respectively.[65, 167, 174]

7.4.2 *Microstructure analysis*

Here, we analyze the GIWAXS measurements of the 5 % and 10 % compositions and compare the results with two phases of PBTTT that have different degrees in structural order, specifically, the terraced (reference) and ribbon phase mentioned earlier and produced at high temperature.

Figure 7.9 shows the 2D GIWAXS images for the films described earlier. As mentioned in Chapter 5, PBTTT orients in an edge-on configuration where the out-of-plane scattering features along the Q_Z axis correspond to the lamella-stacked sidechains $(h00)$ and the in-plane scattering features along the Q_R axis, to the backbone chain ($14.2\,\mathrm{nm^{-1}}$), and the $\pi-\pi$-stacking ($17.1\,\mathrm{nm}$) direction. Likewise, P3HT also orients in an edge-on configuration, and typically shows three strong reflections at $3.9\,\mathrm{nm^{-1}}$, $7.7\,\mathrm{nm^{-1}}$ and $11.4\,\mathrm{nm^{-1}}$ along the Q_Z axis, and one reflection along the Q_R axis at $16.4\,\mathrm{nm^{-1}}$. [104, 130, 175]. For the polymer blends, apart from the typical features of PBTTT, we can distinguish one scattering feature at Q_Z=$3.8\,\mathrm{nm^{-1}}$, that due to its position and intensity, we ascribe to the P3HT fraction. We can assume that the rest of the features corresponding to P3HT, are overlapped with the features of PBTTT, due to being in a lower proportion,. We also note a lower scattering intensity in the blend samples than in the reference and the ribbon materials, yet it is not clear if the origin is a difference in film thickness or an induced disorder in the crystalline domains caused by P3HT. Besides these changes, the neat films are not qualitatively different from each other; that is, the scattering features shift slightly in some cases, but no new *strong* scattering features emerge as one may expect if co-crystallization occurred.

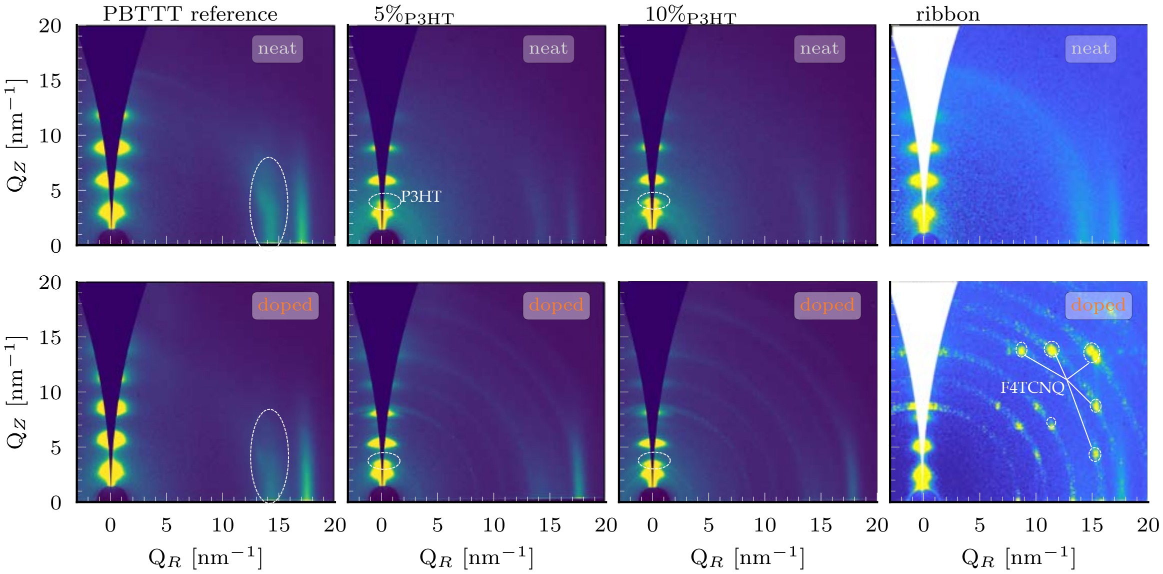

Figure 7.9: 2D GIWAXS images for the neat and doped references, and the polymer blend with a 10 % of P3HT. [a]

---

[a] GIWAXS measurements were done by Sara Marina and Dr. Jaime Martín. University of the Basque Country, POLYMAT. The unprocessed data is available for further reference in the GitHub repository of this thesis.

Doping, on the other hand, provokes more significant changes in the lattice of all samples. The scattering features along the out-of-plane and in-plane directions shift due to the dopant allocating and expanding the lattice. We also observe a partial blurring at Q_{xy}=14.2 nm^{-1}, previously attributed to dopant-induced disorder along the backbone chain direction. [35] For the ribbon sample, we observe the appearance of rings and dot-like scattering features that are likely from the excess dopant accumulated on the surface. More interestingly, the in-plane scattering of the peak ascribed to P3HT increases in intensity compared to their neat counter-parts possibly due to an induced-ordering effect caused by doping, as discussed in references [121].

Figure 7.10 shows further analysis of the out-of-plane and in-plane integrations. As noted before, the most apparent differences between the polymer mixtures and the reference occur after doping. In the out-of-plane direction, the diffraction peaks attributed to P3HT narrow and increase in intensity. Additionally, the out-of-plane peaks shift towards shorter scattering vectors, Q, thus indicating an expansion of the lamella and in the blends, they simultaneously narrow compared to their neat materials, possibly indicating improved order [55, 58] By contrast, the in-plane peak at 17.1 nm^{-1} shows the opposite behavior, that is, it contracts along the (010) direction and as before, appears to narrow. It is difficult to evaluate the scattering patterns of the ribbon phase due to the excess dopant, as seen by the narrow peaks overlapped in the scattering features of PBTTT. Nonetheless we highlight that upon doping, the peaks of the blend materials shift more similarly to what we observe for the ribbon material than for the reference.

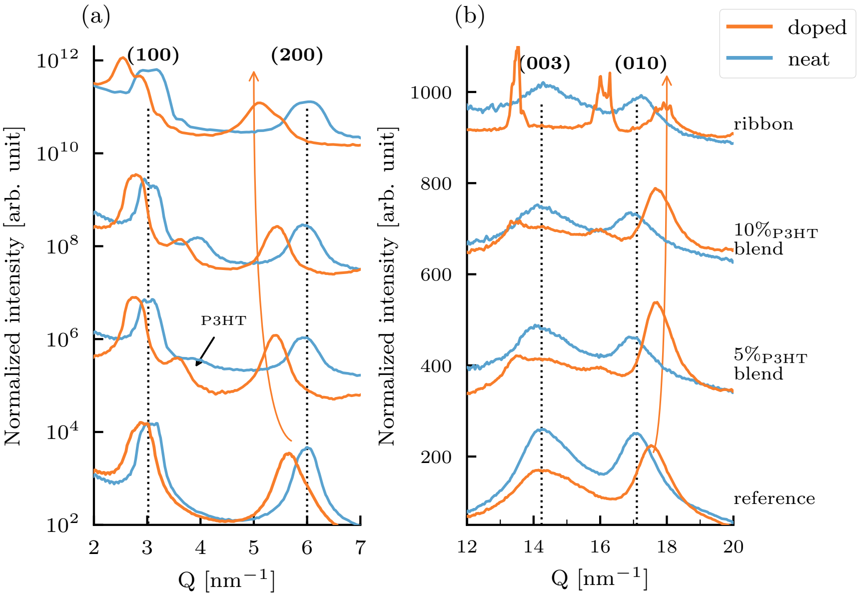

Figure 7.10: (a) out-of-plane and (b) in-plane GIWAXS patterns for the neat and doped films studied in this section. Dashed lines indicate the position of prominent peaks of the neat-reference.

In a nutshell, doping (i) increases the (100) lamellar spacing and (ii) reduces the (010) spacing. The result is an expansion of the unit cell volume (as seen in Figure 7.11a) due to F4TCNQ allocating within the lamella. [120, 130] Noteworthy, (i) this effect is more substantial for the polymer mixtures and the ribbon material. Possibly due to a (i) larger amount of dopant infiltrated within the lamella —– while, the (ii) shorter $\pi - \pi$ stacking distance indicates stronger co-facial interactions between conjugated systems, which leads to the formation of co-crystals and charge transfer complexes. [35]

To quantify the degree of positional disorder of the conjugated subunits, we evaluate the paracrystallinity along specific crystal directions using only the peak center position and breadth (Δ_q) of the diffraction peak (q_0), [57] following Equation 7.4.2.

$$g = \sqrt{\frac{\Delta_q}{2\pi q_0}} \tag{7.2}$$

For this analysis, we exclude the ribbon material due to the increased texture and new reflections caused by excess dopant that will affect the peak's height and width.

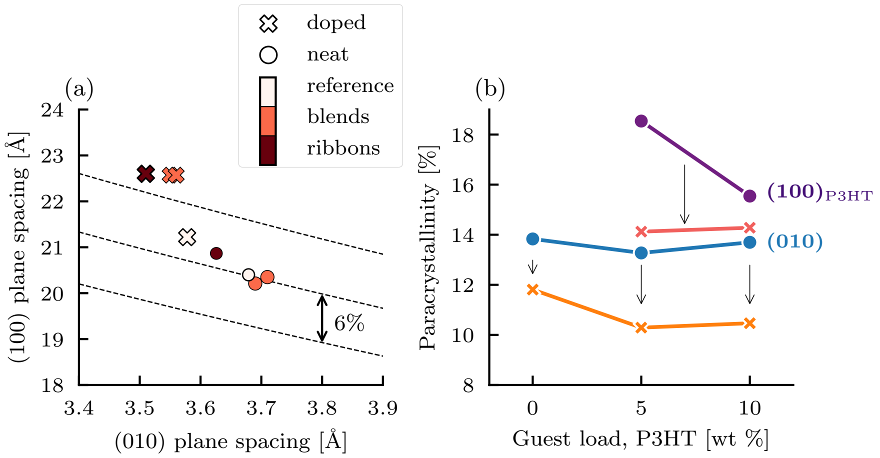

Figure 7.11: (a) (100) and (010) plane spacings obtained from the GIWAXS patterns. Dashed line is a contour plots of the unit cell volume relative to a neat as-cast sample of PBTTT. (b) Paracrystallinity in the $\pi-\pi$-stacking (010) direction and in the (100) of the P3HT peaks.

As seen in Figure 7.11b, doping lowers the paracrystallinity in the (010) direction relative to the neat materials, thus indicating a dopant-induced ordering effect in this direction. We also observe the same effect in the isolated peak of P3HT, indicating that the induced ordering effect occurs on both polymer fractions. In films of F4TCNQ-doped RRa-P3HT and blends of P3HT:RRa-P3HT, the doping-induced ordering effect is ascribed to polaron delocalization along the backbone — increasing the planarity, conjugation length, and thus, provoking a long-range periodicity of the polymer chains. [121, 122] Remarkably, the doping-induced ordering effect appears to be stronger in the materials with higher CTCs content (ribbons and polymer mixtures), which is in good agreement with previous publications regarding CTCs in RR-P3HT. [108].

The current section revealed three critical details about the blending and doping process. (1) The addition of P3HT into a PBTTT matrix induces a morphology with a preferential orientation that resembles the ribbon phase of PBTTT. (2) Doping favors CTCs formation more in the polymer-polymer mixtures than in the reference material, which also (3) contributes to a doping-induced ordering effect in the $\pi-\pi$ stacking direction.

7.5 POTENTIAL IMPACT ON THE THERMOELECTRIC PERFORMANCE

Optimization of the doping level is essential to find the best ZT. Nonetheless, this process is limited by the transport properties of the studied material. To exemplify the latter, in Figure 7.12 we plot the thermopower-conductivity relation given by Equation 7.3.

$$S = \frac{k_B}{e}\frac{\pi^2}{3}s\left(\frac{\sigma}{\sigma_{E0}}\right)^{1/s} \tag{7.3}$$

where k_B/e is the natural unit of the thermopower of 86.17 µV K^{-1}, s is the transport parameter generally fitted to 3, and σ_{E0} is the transport coefficient, which can be considered as a weighed mobility with a strong correlation with sample preparation. [54, 176] To benchmark our results, we plotted contour lines for different values of ZT following Equation 7.5.

$$S = \sqrt{\frac{\kappa_{total}\, zT}{\sigma T}} \tag{7.4}$$

Where $\kappa_{total} = \kappa_{\mathrm{e}} + \kappa_{\mathrm{latt}}$ and $\kappa_{\mathrm{latt}} = 0.3\,\mathrm{W\,m^{-1}\,K^{-1}}$. In this framework, changing the material's doping level while maintaining a fixed transport coefficient bounds the possible achievable ZT. [176]

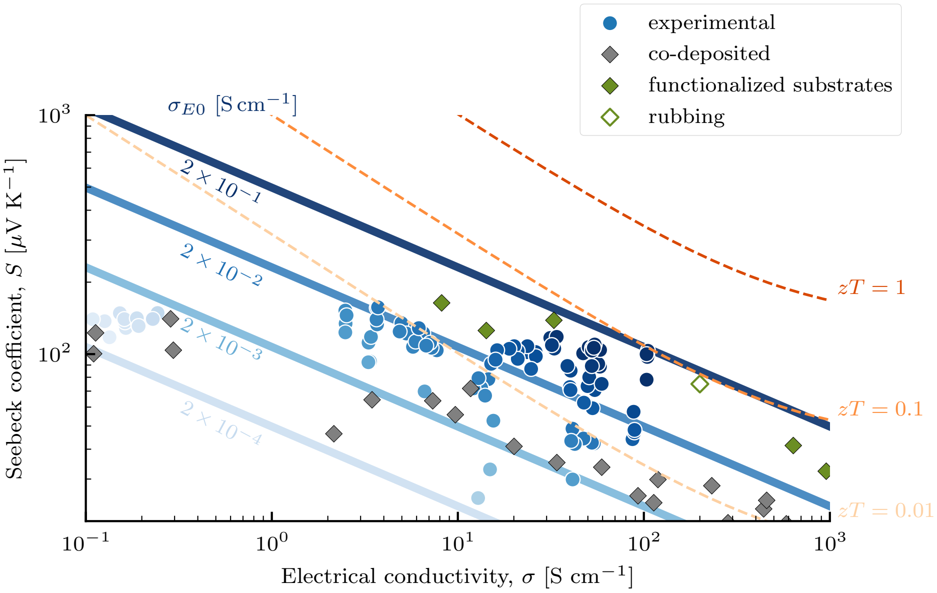

Figure 7.12: Contour plot of the thermoelectric figure of merit. Solid lines represent different σ_{E0} values following Equation 7.3. Green and gray diamonds is data from the literature for PBTTT doped with F4TCNQ following different methods. Blue circles correspond to all the measurements show in in Figure 7.4.

Thus, a possible solution to reach a higher ZT is to find materials with higher σ_{E0}, with a fundamentally different charge transport mechanism, or capable of acquiring a range of σ_{E0} values through processing. A good example is found already within PBTTT when comparing the thermoelectric properties reported in the literature for F4TCNQ-doped PBTTT processed through distinct methods. Specifically: (1) films oriented through rubbing,[34] to achieve macroscopically oriented samples; (2) deposited on functionalized substrates to achieve a high length scale of aligned backbones; [35] and (3) through co-deposition [158] (cf. green diamonds and gray diamonds from Figure 7.12). In short, the best performing materials are those with a high structural order, even though the materials are the same in all cases.

Similarly, the transport coefficient σ_{E0} in our polymer mixtures varies up to two orders of magnitude, matching some of the exemplified materials and almost reaching a ZT of 0.1. Nonetheless, we expect the polymer-mixtures approach to be more practical than other highly elaborated methods, such as rubbing[59] or substrate functionalization[35], as they can complicate the fabrication process. For instance, using a higher annealing temperature to induce structural order requires careful control of the environment to avoid the polymer's degradation. [67] Also, requiring such high annealing temperatures strongly limits the choice of flexible substrates for sample preparation.

For comparison, in Figure 7.13 we have compiled the calculated anion concentration, C_{anion} and thermoelectric properties of pure doped PBTTT dependent on the annealing temperature, and those of various 10 % and 15 % compositions.

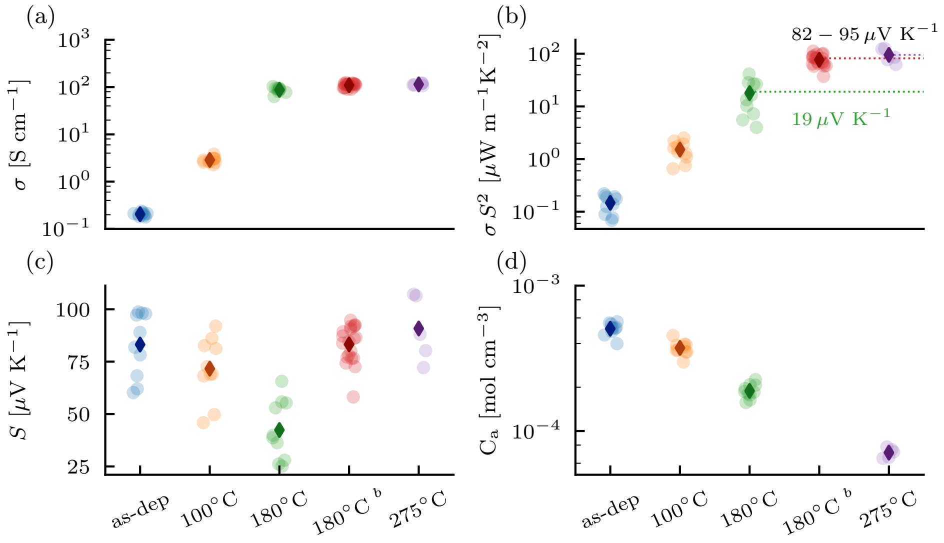

Figure 7.13: (a) Electrical conductivity, (b) power factor, (c) Seebeck coefficient and (d) calculated anion concentration for doped films of pure PBTTT and doped samples of 10 % and 15 % compositions (denoted with a 'b') dependent on the annealing temperature. Diamonds depict the mean value of the shown distributions.

Reassuringly, the performance of the blends processed at 180 °C is statistically the same as that of the ribbon phase, which was treated at 275 °C. While the electrical conductivity for the reference samples, the ribbon phase and the blends is similar, the improved thermoelectric performance in the polymer blends and the ribbon materials is due to a much larger Seebeck coefficient.

7.6 EXTENSION TO OTHER MATERIALS

To evaluate if our observations are confined to using just P3HT as a possible guest material, we fabricated an additional set of films with varied HOMO energy levels, T_g, and melting temperature (T_m). The latter not only to discover new guest candidates but to identify critical parameters for our previous observations. In this context, we fabricated films comprising PBTTT mixed with 5 %, 10 % and 15 % wt% fractions of varied polymers PTB7-Th, PFO, PCPDTBT, PCDTBT, and with 5 %, 10 %, 15 %, 30 %, 60 % and 80 % of PC71BM. Table 7.1 shows the literature-compiled propeties of these materials, and for clarity, we present the T_gs and HOMO values plotted in Figure 7.14.

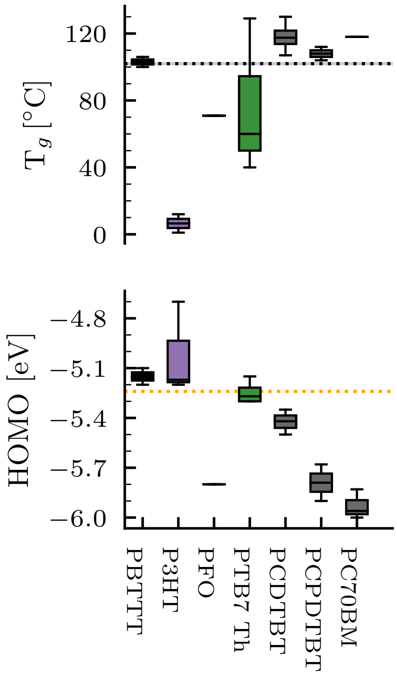

Figure 7.14: T_g and HOMO energy levels from literature-compiled data shown in Table 7.1. Dashed lines are the LUMO level of F4TCNQ and the T_g of the reference material.

Polymer	T_g [°C]	T_m [°C]	HOMO [eV]
RR-P3HT	1 [177], Rh	248 [178], DSC	−4.7[179], PYS
	12 [180], Rh	233[181], DSC	−5.17[182], CV
			−5.2 [42], CV
PBTTT	100 [172], UV-Vis-Nir	250[68], DSC	−5.2 [29], CV
	106 [177], Rh	232 [172], DSC	−5.1[55], UPS
PCDTBT	107 [177], Rh	277[183], DSC	−5.5 [184], CV
	116 [177], Rh		−5.35 [184], CV
	119 [177], Rh		−5.42 [185], CV
	130 [186], DSC		
PCPDTBT	112[177], Rh	318[187], DSC	−5.9 [188], CV
	104 [172], UV-Vis-Nir		−5.68 [189], CV
PFO	71 [177], Rh	170[190], DSC	−5.8 [191], CV
	70.8 [177], Rh		−5.8[166], CV
PTB7-Th	40 [177], Rh	276[178], DSC	−5.4 [192], CV
	60 [193], Rh		−5.3 [194], CV
	129 [193], Rh		−5.15 [195], CV
PC71BM	118[181], DSC	-	−5.83[196], CV
		-	−5.96[197], CV
		-	−6[198], CV

Table 7.1: T_g, T_m and HOMO energy levels for the guest materials chosen in this work. Data was extracted from the shown references and methods and characterization methods; UV-Vis-NIR spectroscopy, Rheology (Rh), Differential Scanning Calorimetry (DSC), Cyclic Voltammetry (CV), Ultraviolet photoelectron spectroscopy (UPS) and Photoelectron Yield Spectroscopy (PYS). The values compiled in this table correspond to the reported T_gs and T_ms of the backbone.

Of the chosen guest materials, PTB7-Th, PFO and P3HT have a lower T_g than the reference material, making them candidates for acting as a plasticizer.[170] Alternatively, PFO is the only material with a lower

T_m than the reference. As for the energy levels, all the chosen guest materials have a deeper HOMO than the LUMO of F4TCNQ, thus we expect a less efficient or null charge transfer between these materials and the dopant.

7.6.1 *Transport coefficient as a proxy for evaluating microstructure and disorder*

Figure 7.15 shows the measured thermoelectric properties for the previously described samples and plotted in the same thermopower-conductivity relation scheme. The latter allows us to identify leaps between different transport coefficients, as we did for the PBTTT:P3HT compositions and thus, utilize the value of σ_{E0} as a proxy for changes in the carrier mobility.

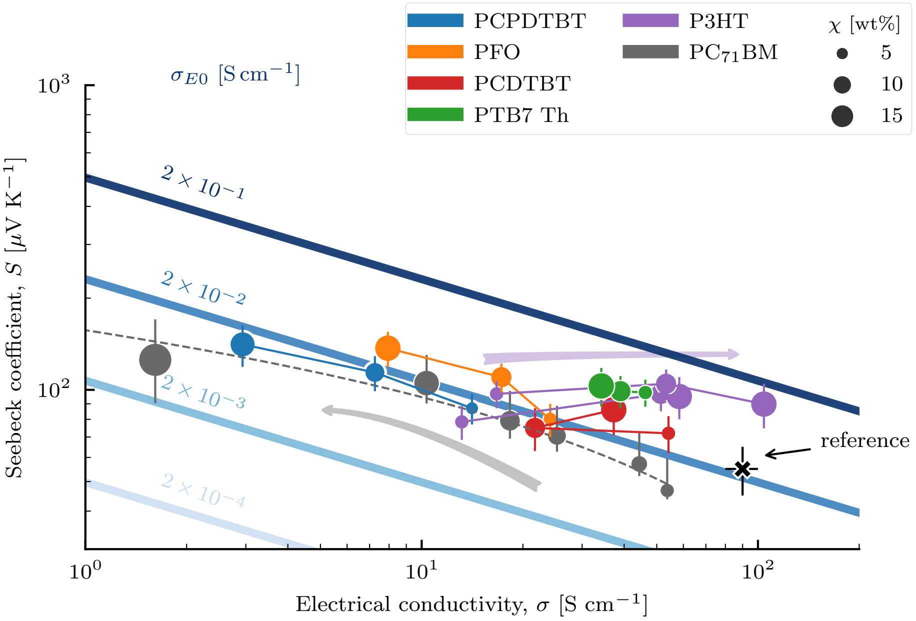

Figure 7.15: Thermoelectric properties of doped PBTTT with a distinct set of added guest materials. Solid lines represent the Equation 7.3 with different values of σ_{E0}. The error bars represent the standard deviation of different measurements. Gray dashed line is a guide to the eye for the PC71BM based composite.

At first glance, we can identify that none of the chosen compositions show a lower σ_{E0} than the reference, indicating that the percolating network does not deteriorate for the compositions under study. We can also distinguish that σ and S in the PCPDTBT-, PFO- and PCDTBT-based composites exhibit a fixed σ_{E0} value for the tested compositions. This is the expected trend when blending simply modulates the doping level. However, we are not intentionally changing the doping level for these samples but adding increasing fractions of a guest material that occupies free space in the lattice, thus leaving fewer vacancies for the dopant. Other effects can be possible, e. g., a fraction of the dopant can be allocated within the guest material, leading also to a dilution effect of the dopant.

On the other hand, PTB7-Th-based composites show a significantly higher σ_{E0} relative to the reference, suggesting that these films have better charge transport properties, albeit less substantial than what we observe when using P3HT. The changes in S and σ for this material do not change drastically, but they appear to shift horizontally as seen with P3HT. However, more samples with a broader range of compositions are needed to confirm it. Conversely, the P3HT-based composites are the only ones that jump between different σ_{E0} values and that show a simultaneous increase in σ and S when increasing the guest fraction from 0 % to 15 %. Whether PTB7-Th interacts with the dopant is not entirely clear, but the results presented in Section 6.5 indicate this is not the case. Moreover, we observe that the 5 % PTB7-Th composite does not induce CTCs to the same degree as its P3HT counterpart either, as seen in figure Figure 7.16.

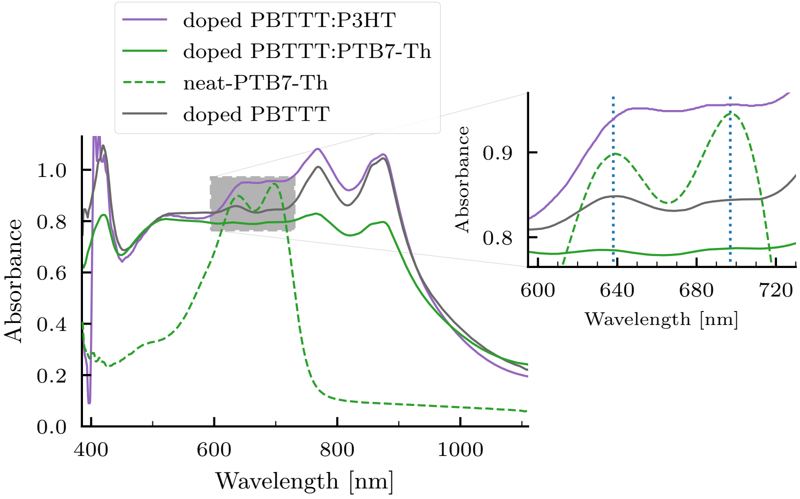

Figure 7.16: UV-Vis-NIR spectra for doped pure PBTTT and the 5 % PTB7-Th- and P3HT-based composites. Also for comparison, we show the spectrum of neat PTB7-Th. Data is normalized at the neutral band of PBTTT.

PC71BM-based composites offer insight to our previous observations. This particular guest material does not have a T_g nor a T_m lower than the reference material. The HOMO energy level is not ideal for a charge-transfer process with F4TCNQ either. Mixtures of PBTTT: PC71BM generate bimolecular crystals, in which the fullerene derivative intercalates between the sidechains and each face of the polymer backbone tilts and partially faces a PC71BM molecule. [159] The latter disrupts the $\pi - \pi$ stacking and thus, reduces the size of the hole-percolating network.[199] Moreover, we can expect a dilution of the available doping-sites, given that F4TCNQ competes for the same position in the lattice (between the sidechains). Consequently, with this particular coposition we *do* expect a pure blending effect, where the electrical conductivity decreases due to the limited available doping-sites. With a subsequent comparison of the trend followed by the PC71BM-based composites against the rest of the blends, we can further propose that the PCPDTBT-, PFO- and PCDTBT-based composites show a pure blending effect.

The thermoelectric properties of PC71BM-based blends are included in Appendix A.

7.6.2 *GIWAXS analysis for selected polymer blends*

As with P3HT-based composites, we studied the structural changes through GIWAXS analysis. Figure 7.17 shows the evolution of the $(h00)$ and $(0k0)$ crystalline planes for the neat, and doped 5 % and 10 % PTB7-Th- and PFO-based compositions. Here we observed a similar trend to the one we have seen for PBTTT:P3HT composites (here reproduced for comparison). Specifically, the scattering features of the neat compositions do not change significantly compared with the neat reference — but with doping, they expand along the (100) and (200) direction to a similar degree than the P3HT-based compositions.

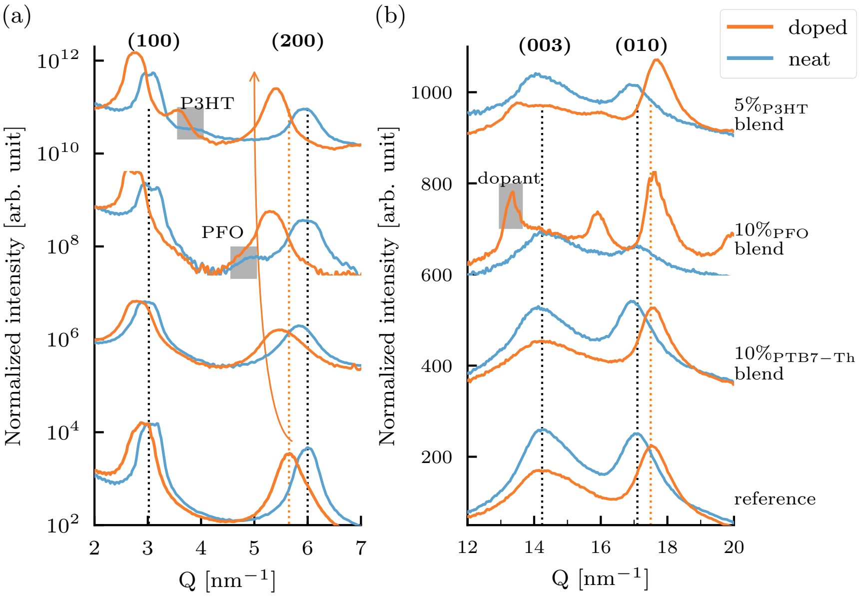

Figure 7.17: (a) out-of-plane and (b) in-plane GIWAXS patterns for the neat and doped films of pure PBTTT and for different polymer mixtures. Dashed lines are guides to the eye for representative peaks. Data is offset for clarity.

For the PFO-based composite, we additionally note two new scattering peaks at $4.8\,\mathrm{nm}^{-1}$ and $13.3\,\mathrm{nm}^{-1}$ that we tentatively ascribe to pure PFO and F4TCNQ, respectively. Also noteworthy, the isolated peak of PFO does not shift with doping nor appears to increase in intensity as it occurs for the P3HT counterpart, further suggesting that doping occurs in the P3HT fractions, and that the observed shift is due to a charge-transfer process and not a filling effect, as discussed in references [35, 121, 139].

Figure 7.18 shows the fitted σ_{E0} of different polymer mixtures as a function of the HOMO energy level of their respective guest material. At first sight, we can observe that σ_{E0} increases for materials that are more compatible with the LUMO of F4TCNQ or within closer range. A possible rationalization is the following; in the pure composition, holes move through the most optimal pathways, preferentially through sites that are near in energy. [82]. Given that the HOMO level of P3HT and PBTTT is relatively similar, it is possible that generated holes in P3HT or PBTTT can be injected arbitrarily in any given fraction [42, 82] With low fractions of P3HT, one could imagine few obstacles that are not necessarily too different in energy, and thus, provide a good percolating path.

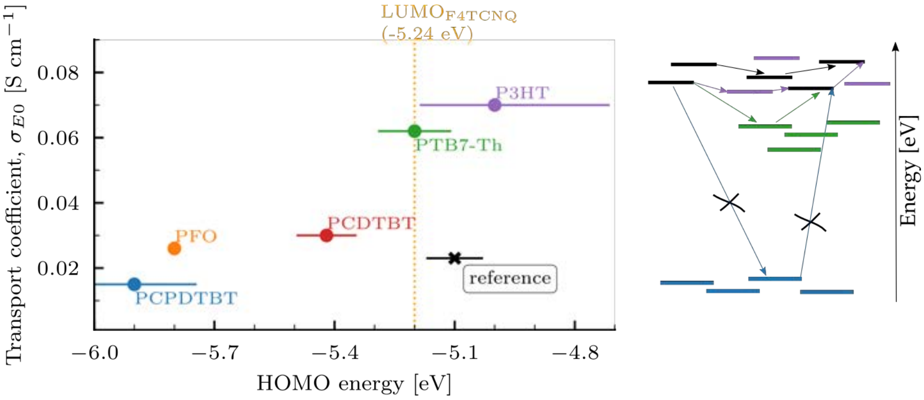

Figure 7.18: σ_{E0} dependent on the HOMO energy level. The error bars are the standard deviation of the values shown in Table 7.1. Additionally, energy diagram for the proposed mechanism occurring in this chapter.

By contrast, for materials with deeper HOMO levels than the reference, hopping is a trade-off between sites near in energy and sites that are nearby. Here, for small fractions of the guest material, holes will be located in PBTTT, but with higher fractions, ($>$ 80%) we should observe a maximum in S due to a shift of E_{tr} towards the material with the deeper HOMO, as demonstrated in references [41, 82]. Consequently, our results indicate that besides inducing local order in the microstructure with an added guest material, a percolating path similar in energy is also necessary.

We consider previous observations as an initial screening for new guest materials. Future work with broader composition ratios complemented with other characterization techniques will help us elucidate the whole picture of our current results. For instance;

1. A more in-depth analysis of the doping level is required. This will help us to fully understand if the observed thermoelec-

tric improvement is driven entirely by a change in the charge mobility.

2. Measuring the hole mobility would help us understand the interplay between microstructure, doping and charge transport.
3. Measuring the T_g and T_m of the blends would help to corroborate one of our proposed theories regarding the plastizicer effect.
4. Further AFM and GIWAXS analysis (without dopant agglomeration) is required to corroborate if the new guest materials achieve a preferential orientation, lower paracrystallinity or a larger coherence length. In any case, The recent observations indicate that besides a lower T_g, other parameters are at play e. g., similar energy levels between the guest and host materials.
5. We still do not fully understand the effect that CTCs have on the structural order of semi-crystalline polymers like PBTTT. Our results suggest that they induce a small degree of order in the $\pi - \pi$ stacking but the nature is not fully understood.

7.7 CONCLUSIONS

In this chapter, we have demonstrated that polymer mixtures of PBTTT with P3HT have outstanding thermoelectric properties. The achieved electrical conductivity and Seebeck coefficient are comparable to films processed through other, more complex methods that yield high macroscopically oriented samples or large orientational correlation lengths. We ascribe our results to a combined effect of induced-ordering, driven by the blending process and doping, and a percolating network with hopping sites similar in energy. In conclusion, adding P3HT appears to lower the necessary processing temperature for generating a similar structure than the ribbon phase of pure PBTTT. On the other hand, doping appears to induce order in the $\pi - \pi$ stacking direction due to charge delocalization and the presence of CTCs that reside closer to the backbone. The resulting films of polymer mixtures have a transport coefficient that varies several orders of magnitude depending on the guest fraction. Our results present a simple yet effective method to enhance the Seebeck coefficient and electrical conductivity in a matrix of PBTTT simultaneously.

Part IV

CONCLUSIONS

8

CONCLUSIONS

This thesis detailed three essential aspects for developing organic thermoelectric materials: improving the thermoelectric stability under thermal stress, stretching our understanding of the thermal and electric transport in doped materials, and strategies to improve electrical conductivity and the Seebeck coefficient simultaneously.

We demonstrated that it is possible to take advantage of the higher thermal stability of CTCs that naturally coexists with IPAs in doped PBTTT. While CTC formation is detrimental to the electrical conductivity, we were able to adjust the content of either CTCs or IPAs with an in-house developed method. With the latter, we show that introducing a small amount of CTCs improves the long-term thermoelectric stability without a significant sacrifice in the electrical conductivity and thus in the thermoelectric properties. Our results indicate that the improved thermal stability arises from dopant locating closer to the polymer backbone and in positions less prone to dedoping under thermal stress. These results provide alternative routes for improving the thermoelectric stability, relying on controlling the microstructure and interactions between the conjugated polymers and the dopants.

Additionally, we demonstrated that in neat films of PBTTT the thermal charge transport is determined by the degree of crystallinity and structural order present in the film. Doping a polymer film with a high degree of crystallinity does not deteriorate the crystallinity quality or structural order; however, it induces a drastic reduction of the thermal conductivity. These observations show that thermal transport, at least for the material in this study, is dominated by disorder, comparable to what is commonly referred to as *'alloy scattering'* in inorganic materials. The potential impact and implications of these results highlight a meaningful opportunity in developing organic thermoelectric materials. That is, doping results in a semicrystalline solid for electrons and an amorphous solid for heat transport.

Finally, we demonstrate that introducing P3HT into a PBTTT matrix is a simple yet effective method to improve the structural order of the solid state in thin films. The achieved electrical conductivity and Seebeck coefficient are comparable to films processed through other, more complex methods that yield high orientation and correlation lengths. We ascribe our results to a combined effect of induced-ordering driven by the blending process and doping. In conclusion, adding P3HT lowers the necessary temperature for generating a similar structure than the ribbon phase of pure PBTTT. Alternatively, doping induces order in the $\pi - \pi$ stacking direction due to charge delocalization and the presence of CTCs that reside closer to the backbone. The resulting films of polymer mixtures have a transport coefficient that varies several orders of magnitude depending on the guest fraction. Our results present a simple yet effective method to enhance the Seebeck coefficient and electrical conductivity in a matrix of PBTTT simultaneously.

Part V

APPENDIX

APPENDIX

A

Figure A.1 Shows the UV-Vis-NIR absorbance spectra of neat and doped films of oriented PBTTT as well as the measured electrical conductivity at times 0, 3 and 69 days. The films processed at 180 °C were fabricated as described in Chapter 4 while the film with the label of 270 °C was rubbed and then annealed at the corresponding temperature. Temperature annealing of PBTTT at temperatures above 260 °C may lead to the formation of a ribbon phase. No AFM measurements were done for this samples, but we observed different trends of σ over time.

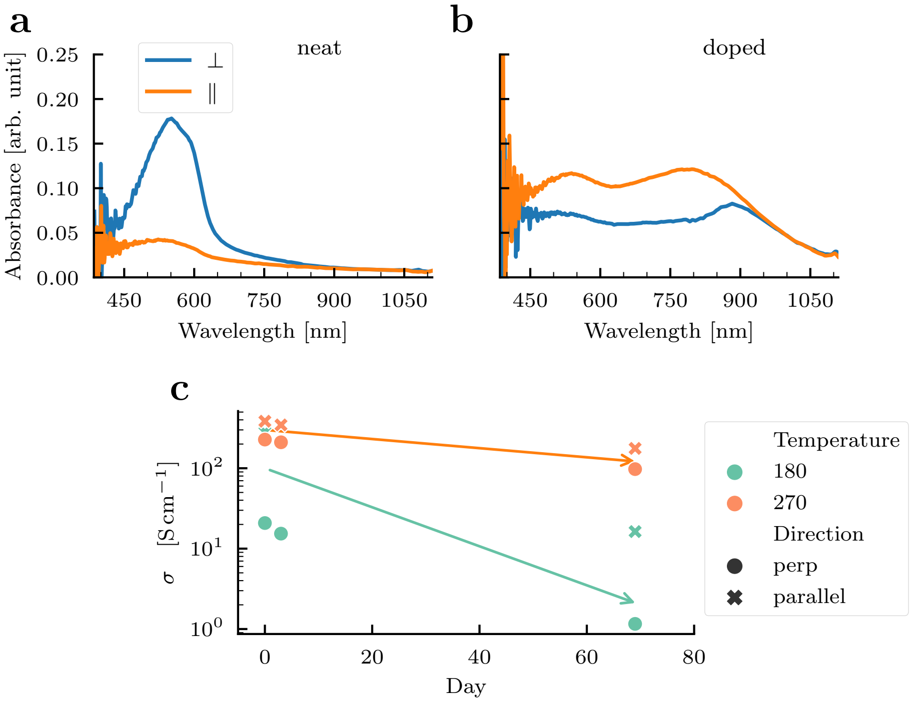

Figure A.1: UV-Vis-NIR of doped and neat films of rubbed PBTTT, as well as the electrical conductivity.

Figure A.2 shows the thermoelectric properties for blends of neat and doped PBTTT:PC71BM at varying PC71BM compositions. Both S and σ follow a trend that resembles a modulation of the doping level, as mentioned in Chapter 7. On the other hand, doping decreases the thermal conductivity of PBTTT compared to the neat film in agreement with the results presented in Chapter 6. Alternatively, adding fractions of PC71BM below 25wt% and then doping increases the thermal conductivity and finally with fractions closer to pure PC71BM we observe a thermal conductivity that resembles that other reported fullerenes.

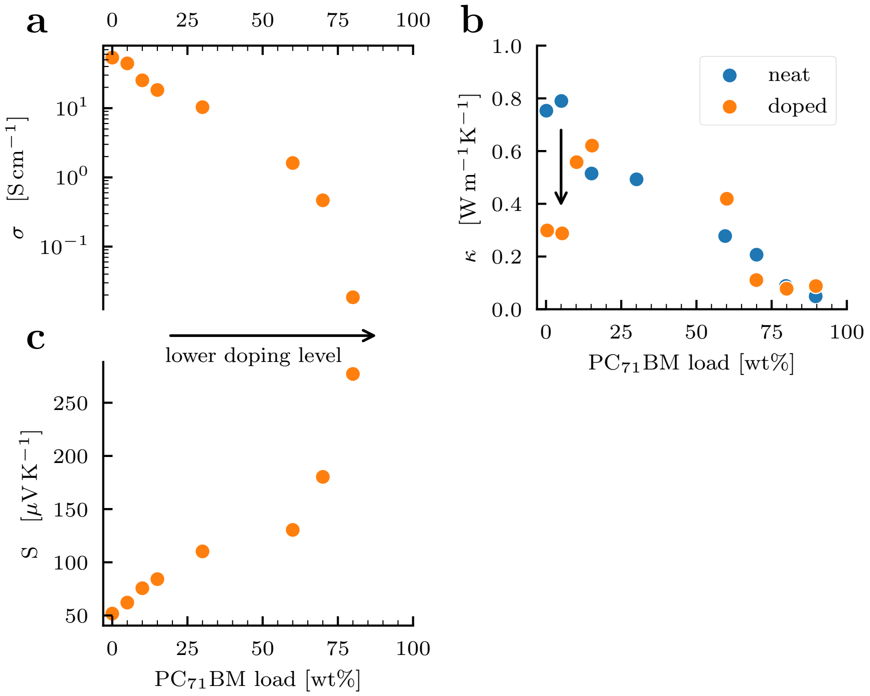

Figure A.2: (a) Electrical conductivity, (b) thermal conductivity and (c) Seebeck coefficient of PBTTT as a function of added PC71BM.

BIBLIOGRAPHY

[1] Zhuhua Hu, Ruoqing Li, Xin Xia, Chuang Yu, Xiang Fan, and Yaochi Zhao. “A method overview in smart aquaculture.” In: *Environmental Monitoring and Assessment* 192.8 (Aug. 2020), p. 493. DOI: 10.1007/s10661-020-08409-9.

[2] Robert Freer and Anthony V. Powell. “Realising the potential of thermoelectric technology: a Roadmap.” In: *Journal of Materials Chemistry C* 8.2 (2020), pp. 441–463. DOI: 10.1039/C9TC05710B.

[3] Héctor Espinoza, Gerhard Kling, Frank McGroarty, Mary O’Mahony, and Xenia Ziouvelou. “Estimating the impact of the Internet of Things on productivity in Europe.” In: *Heliyon* 6.5 (May 2020), e03935. DOI: 10.1016/j.heliyon.2020.e03935.

[4] Deyaa Abol-Fotouh, Bernhard Dörling, Osnat Zapata-Arteaga, Xabier Rodríguez-Martínez, Andrés Gómez, J. Sebastian Reparaz, Anna Laromaine, Anna Roig, and Mariano Campoy-Quiles. “Farming thermoelectric paper.” In: *Energy & Environmental Science* 12.2 (2019), pp. 716–726. DOI: 10.1039/C8EE03112F.

[5] Michael Papapetrou, George Kosmadakis, Andrea Cipollina, Umberto La Commare, and Giorgio Micale. “Industrial waste heat: Estimation of the technically available resource in the EU per industrial sector, temperature level and country.” In: *Applied Thermal Engineering* 138.April (June 2018), pp. 207–216. DOI: 10.1016/j.applthermaleng.2018.04.043.

[6] Albert Tarancón. “Powering the IoT revolution with heat.” In: *Nature Electronics* 2.7 (July 2019), pp. 270–271. DOI: 10.1038/s41928-019-0276-4.

[7] Boris Russ, Anne Glaudell, Jeffrey J. Urban, Michael L. Chabinyc, and Rachel A. Segalman. “Organic thermoelectric materials for energy harvesting and temperature control.” In: *Nature Reviews Materials* 1.10 (Oct. 2016), p. 16050. DOI: 10.1038/natrevmats.2016.50.

[8] Glen Slack. “New Materials and Performance Limits for Thermoelectric Cooling.” In: *CRC Handbook of Thermoelectrics*. CRC Press, July 1995. DOI: 10.1201/9781420049718.ch34.

[9] José P. Jurado, Bernhard Dörling, Osnat Zapata-Arteaga, Anna Roig, Agustín Mihi, and Mariano Campoy-Quiles. "Solar Harvesting: a Unique Opportunity for Organic Thermoelectrics?" In: *Advanced Energy Materials* (2019). DOI: `10.1002/aenm.201902385`.

[10] G.P. Kenny and A.D. Flouris. "The human thermoregulatory system and its response to thermal stress." In: *Protective Clothing*. Elsevier, 2014, pp. 319–365. DOI: `10.1533/9781782420408.3.319`.

[11] H. J. Goldsmid, A. R. Sheard, and D. A. Wright. "The performance of bismuth telluride thermojunctions." In: *British Journal of Applied Physics* 9.9 (Sept. 1958), pp. 365–370. DOI: `10.1088/0508-3443/9/9/306`.

[12] Shaoqing Zhang, Long Ye, Wenchao Zhao, Delong Liu, Huifeng Yao, and Jianhui Hou. "Side chain selection for designing highly efficient photovoltaic polymers with 2D-conjugated structure." In: *Macromolecules* 47.14 (July 2014), pp. 4653–4659. DOI: `10.1021/ma500829r`.

[13] Joseph Davidow and Yaniv Gelbstein. "A comparison between the mechanical and thermoelectric properties of three highly efficient p-type GeTe-Rich compositions: TAGS-80, TAGS-85 and 3% Bi 2Te3-Doped Ge0.87Pb0.13Te." In: *Journal of Electronic Materials* 42.7 (July 2013), pp. 1542–1549. DOI: `10.1007/s11664-012-2316-y`.

[14] Hu Yan, Norina Sada, and Naoki Toshima. "Thermal transporting properties of electrically conductive polyaniline films as organic thermoelectric materials." In: *Journal of Thermal Analysis and Calorimetry* 69.3 (2002), pp. 881–887. DOI: `10.1023/A:1020612123826`.

[15] Dasaroyong Kim, Yeonseok Kim, Kyungwho Choi, Jaime C. Grunlan, and Choongho Yu. "Improved thermoelectric behavior of nanotube-filled polymer composites with poly(3,4-ethylenedioxythiophene) poly(styrenesulfonate)." In: *ACS Nano* 4.1 (Jan. 2010), pp. 513–523. DOI: `10.1021/nn9013577`.

[16] Olga Bubnova, Zia Ullah Khan, Abdellah Malti, Slawomir Braun, Mats Fahlman, Magnus Berggren, and Xavier Crispin. "Optimization of the thermoelectric figure of merit in the conducting polymer poly(3,4-ethylenedioxythiophene)." In: *Nature Materials* 10.6 (June 2011), pp. 429–433. DOI: `10.1038/nmat3012`.

[17] G-H Kim, L Shao, K Zhang, and K P Pipe. "Engineered doping of organic semiconductors for enhanced thermoelectric efficiency." In: *Nature Materials* 12.8 (Aug. 2013), pp. 719–723. DOI: `10.1038/nmat3635`.

[18] Prospero J. Taroni et al. "Toward Stretchable Self-Powered Sensors Based on the Thermoelectric Response of PEDOT:PSS/Polyurethane Blends." In: *Advanced Functional Materials* 28.15 (Apr. 2018), p. 1704285. DOI: `10.1002/adfm.201704285`.

[19] Cheng Jin An, Young Hun Kang, A-Young Lee, Kwang-Suk Jang, Youngjin Jeong, and Song Yun Cho. "Foldable Thermoelectric Materials: Improvement of the Thermoelectric Performance of Directly Spun CNT Webs by Individual Control of Electrical and Thermal Conductivity." In: *ACS Applied Materials & Interfaces* 8.34 (Aug. 2016), pp. 22142–22150. DOI: `10.1021/acsami.6b04485`.

[20] Anja Lund, Yuan Tian, Sozan Darabi, and Christian Müller. "A polymer-based textile thermoelectric generator for wearable energy harvesting." In: *Journal of Power Sources* 480 (Dec. 2020), p. 228836. DOI: `10.1016/j.jpowsour.2020.228836`.

[21] Sozan Darabi et al. "Green Conducting Cellulose Yarns for Machine-Sewn Electronic Textiles." In: *ACS Applied Materials and Interfaces* 12 (Dec. 2020), pp. 56403–56412. DOI: `10.1021/acsami.0c15399`.

[22] Jason D. Ryan, Desalegn Alemu Mengistie, Roger Gabrielsson, Anja Lund, and Christian Müller. "Machine-Washable PEDOT:PSS Dyed Silk Yarns for Electronic Textiles." In: *ACS Applied Materials & Interfaces* 9.10 (Mar. 2017), pp. 9045–9050. DOI: `10.1021/acsami.7b00530`.

[23] Davide Beretta et al. "Thermoelectrics: From history, a window to the future." In: *Materials Science and Engineering: R: Reports* 138.July 2018 (Oct. 2019), p. 100501. DOI: `10.1016/j.mser.2018.09.001`.

[24] W M Haynes. *CRC Handbook of Chemistry and Physics*. CRC Press, 2016.

[25] Meetu Bharti, Ajay Singh, Soumen Samanta, and D.K. Aswal. "Conductive polymers for thermoelectric power generation." In: *Progress in Materials Science* 93 (Apr. 2018), pp. 270–310. DOI: `10.1016/j.pmatsci.2017.09.004`.

[26] Kai Xu et al. "Ground-state electron transfer in all-polymer donor–acceptor heterojunctions." In: *Nature Materials* (Mar. 2020). DOI: `10.1038/s41563-020-0618-7`.

[27] Renee Kroon, David Kiefer, Dominik Stegerer, Liyang Yu, Michael Sommer, and Christian Müller. "Polar Side Chains Enhance Processability, Electrical Conductivity, and Thermal Stability of a Molecularly p-Doped Polythiophene." In: *Advanced Materials* 29.24 (June 2017), p. 1700930. DOI: `10.1002/adma.201700930`.

[28] Jun Li, Chris W Rochester, Ian E Jacobs, Stephan Friedrich, Pieter Stroeve, Moritz Riede, and Adam J. Moulé. "Measurement of Small Molecular Dopant F4TCNQ and C 60 F 36 Diffusion in Organic Bilayer Architectures." In: *ACS Applied Materials & Interfaces* 7.51 (Dec. 2015), pp. 28420–28428. DOI: 10.1021/acsami.5b09216.

[29] David Kiefer et al. "Double doping of conjugated polymers with monomer molecular dopants." In: *Nature Materials* 18.2 (Feb. 2019), pp. 149–155. DOI: 10.1038/s41563-018-0263-6.

[30] Alexandra F. Paterson et al. "Water stable molecular n-doping produces organic electrochemical transistors with high transconductance and record stability." In: *Nature Communications* 11.1 (Dec. 2020), p. 3004. DOI: 10.1038/s41467-020-16648-0.

[31] Zeng Fan, Donghe Du, Xin Guan, and Jianyong Ouyang. "Polymer films with ultrahigh thermoelectric properties arising from significant seebeck coefficient enhancement by ion accumulation on surface." In: *Nano Energy* 51 (Sept. 2018), pp. 481–488. DOI: 10.1016/j.nanoen.2018.07.002.

[32] Annie Weathers, Zia Ullah Khan, Robert Brooke, Drew Evans, Michael T. Pettes, Jens Wenzel Andreasen, Xavier Crispin, and Li Shi. "Significant Electronic Thermal Transport in the Conducting Polymer Poly(3,4-ethylenedioxythiophene)." In: *Advanced Materials* 27.12 (Mar. 2015), pp. 2101–2106. DOI: 10.1002/adma.201404738.

[33] Chungyeon Cho, Kevin L. Wallace, Ping Tzeng, Jui Hung Hsu, Choongho Yu, and Jaime C. Grunlan. "Outstanding Low Temperature Thermoelectric Power Factor from Completely Organic Thin Films Enabled by Multidimensional Conjugated Nanomaterials." In: *Advanced Energy Materials* 6.7 (Apr. 2016). DOI: 10.1002/aenm.201502168.

[34] Vishnu Vijayakumar, Yuhan Zhong, Viktoriia Untilova, Mounib Bahri, Laurent Herrmann, Laure Biniek, Nicolas Leclerc, and Martin Brinkmann. "Bringing Conducting Polymers to High Order: Toward Conductivities beyond 10^5 S cm^-1 and Thermoelectric Power Factors of 2 mW m^-1 K^-2." In: *Advanced Energy Materials* 9.24 (June 2019), p. 1900266. DOI: 10.1002/aenm.201900266.

[35] Shrayesh N Patel, Anne M Glaudell, Kelly A Peterson, Elayne M Thomas, Kathryn A. O'Hara, Eunhee Lim, and Michael L Chabinyc. "Morphology controls the thermoelectric power factor of a doped semiconducting polymer." In: *Science Advances* 3.6 (June 2017), e1700434. DOI: 10.1126/sciadv.1700434.

[36] Anne M. Glaudell, Justin E. Cochran, Shrayesh N. Patel, and Michael L. Chabinyc. "Impact of the Doping Method on Conductivity and Thermopower in Semiconducting Polythiophenes." In: *Advanced Energy Materials* 5.4 (Feb. 2015), p. 1401072. DOI: 10.1002/aenm.201401072.

[37] Yu Yamashita, Junto Tsurumi, Masahiro Ohno, Ryo Fujimoto, Shohei Kumagai, Tadanori Kurosawa, Toshihiro Okamoto, Jun Takeya, and Shun Watanabe. "Efficient molecular doping of polymeric semiconductors driven by anion exchange." In: *Nature* 572.7771 (2019), pp. 634–638. DOI: 10.1038/s41586-019-1504-9.

[38] Kentaro Harada, Mao Sumino, Chihaya Adachi, Saburo Tanaka, and Koji Miyazaki. "Improved thermoelectric performance of organic thin-film elements utilizing a bilayer structure of pentacene and 2,3,5,6-tetrafluoro-7,7,8,8-tetracyanoquinodimethane (F4-TCNQ)." In: *Applied Physics Letters* 96.25 (June 2010), p. 253304. DOI: 10.1063/1.3456394.

[39] Patrick Pingel, Malavika Arvind, Lisa Kölln, Robert Steyrleuthner, Felix Kraffert, Jan Behrends, Silvia Janietz, and Dieter Neher. "p-Type Doping of Poly(3-hexylthiophene) with the Strong Lewis Acid Tris(pentafluorophenyl)borane." In: *Advanced Electronic Materials* 2.10 (Oct. 2016), p. 1600204. DOI: 10.1002/aelm.201600204.

[40] Cheng-Kang Mai, Jun Liu, Christopher M Evans, Rachel A Segalman, Michael L Chabinyc, David G Cahill, and Guillermo C Bazan. "Anisotropic Thermal Transport in Thermoelectric Composites of Conjugated Polyelectrolytes/Single-Walled Carbon Nanotubes." In: *Macromolecules* 49.13 (July 2016), pp. 4957–4963. DOI: 10.1021/acs.macromol.6b00546.

[41] Guangzheng Zuo, Xianjie Liu, Mats Fahlman, and Martijn Kemerink. "High Seebeck Coefficient in Mixtures of Conjugated Polymers." In: *Advanced Functional Materials* 28.15 (2018), pp. 1–7. DOI: 10.1002/adfm.201703280.

[42] J. Sun, M.-L. Yeh, B. J. Jung, B. Zhang, J. Feser, A. Majumdar, and H. E. Katz. "Simultaneous Increase in Seebeck Coefficient and Conductivity in a Doped Poly(alkylthiophene) Blend with Defined Density of States." In: *Macromolecules* 43.6 (Mar. 2010), pp. 2897–2903. DOI: 10.1021/ma902467k.

[43] Ruth A. Schlitz, Fulvio G. Brunetti, Anne M. Glaudell, P. Levi Miller, Michael A. Brady, Christopher J. Takacs, Craig J. Hawker, and Michael L. Chabinyc. "Solubility-limited extrinsic n-type doping of a high electron mobility polymer for thermoelectric applications." In: *Advanced Materials* 26.18 (May 2014), pp. 2825–2830. DOI: 10.1002/adma.201304866.

[44] Jian Liu et al. "Enhancing Molecular n-Type Doping of Donor–Acceptor Copolymers by Tailoring Side Chains." In: *Advanced Materials* 30.7 (Feb. 2018). DOI: 10.1002/adma.201704630.

[45] David Kiefer et al. "Enhanced n-Doping Efficiency of a Naphthalenediimide-Based Copolymer through Polar Side Chains for Organic Thermoelectrics." In: *ACS Energy Letters* 3.2 (2018), pp. 278–285. DOI: 10.1021/acsenergylett.7b01146.

[46] Suhao Wang et al. "Thermoelectric Properties of Solution-Processed n-Doped Ladder-Type Conducting Polymers." In: *Advanced Materials* 28.48 (2016), pp. 10764–10771. DOI: 10.1002/adma.201603731.

[47] Chenchen Wang, Duc T Duong, Koen Vandewal, Jonathan Rivnay, and Alberto Salleo. "Optical measurement of doping efficiency in poly(3-hexylthiophene) solutions and thin films." In: *Physical Review B* 91.8 (Feb. 2015), p. 085205. DOI: 10.1103/PhysRevB.91.085205.

[48] Jian Liu et al. "N-type organic thermoelectrics: demonstration of ZT > 0.3." In: *Nature Communications* 11.1 (2020), pp. 1–9. DOI: 10.1038/s41467-020-19537-8.

[49] Francis A. Carey, Richard J. Sundberg, Francis A. Carey, and Richard J. Sundberg. "Chemical Bonding and Molecular Structure." In: *Advanced Organic Chemistry*. Springer US, 1984, pp. 1–60. DOI: 10.1007/978-1-4757-1143-1{_}1.

[50] Fang Chung Chen. "Organic semiconductors." In: *Encyclopedia of Modern Optics* 1-5 (2018), pp. 220–231. DOI: 10.1016/B978-0-12-803581-8.09538-2.

[51] Hugo Bronstein, Christian B. Nielsen, Bob C. Schroeder, and Iain McCulloch. "The role of chemical design in the performance of organic semiconductors." In: *Nature Reviews Chemistry* 4.2 (Feb. 2020), pp. 66–77. DOI: 10.1038/s41570-019-0152-9.

[52] Shrayesh N. Patel and Michael L. Chabinyc. "Anisotropies and the thermoelectric properties of semiconducting polymers." In: *Journal of Applied Polymer Science* 134.3 (Jan. 2017). DOI: 10.1002/app.44403.

[53] Jonathan Rivnay, Stefan C. B. Mannsfeld, Chad E. Miller, Alberto Salleo, and Michael F. Toney. "Quantitative Determination of Organic Semiconductor Microstructure from the Molecular to Device Scale." In: *Chemical Reviews* 112.10 (Oct. 2012), pp. 5488–5519. DOI: 10.1021/cr3001109.

[54] Anas Abutaha, Pawan Kumar, Erol Yildirim, Wen Shi, Shuo-Wang Yang, Gang Wu, and Kedar Hippalgaonkar. "Correlating charge and thermoelectric transport to paracrystallinity in conducting polymers." In: *Nature Communications* 11.1 (Dec. 2020), p. 1737. DOI: 10.1038/s41467-020-15399-2.

[55] Iain McCulloch et al. "Liquid-crystalline semiconducting polymers with high charge-carrier mobility." In: *Nature Materials* 5.4 (Apr. 2006), pp. 328–333. DOI: 10.1038/nmat1612.

[56] Peng Hu et al. "Impact of C–H···X (X = F, N) and π–π Interactions on Tuning the Degree of Charge Transfer in F 6 TNAP-Based Organic Binary Compound Single Crystals." In: *Crystal Growth & Design* 18.3 (Mar. 2018), pp. 1776–1785. DOI: 10.1021/acs.cgd.7b01669.

[57] Rodrigo Noriega, Jonathan Rivnay, Koen Vandewal, Felix P. V. Koch, Natalie Stingelin, Paul Smith, Michael F. Toney, and Alberto Salleo. "A general relationship between disorder, aggregation and charge transport in conjugated polymers." In: *Nature Materials* 12.11 (Nov. 2013), pp. 1038–1044. DOI: 10.1038/nmat3722.

[58] Jonathan Rivnay, Rodrigo Noriega, R. Joseph Kline, Alberto Salleo, and Michael F. Toney. "Quantitative analysis of lattice disorder and crystallite size in organic semiconductor thin films." In: *Physical Review B - Condensed Matter and Materials Physics* 84.4 (2011), pp. 1–20. DOI: 10.1103/PhysRevB.84.045203.

[59] Amer Hamidi-Sakr, Laure Biniek, Jean Louis Bantignies, David Maurin, Laurent Herrmann, Nicolas Leclerc, Patrick Lévêque, Vishnu Vijayakumar, Nicolas Zimmermann, and Martin Brinkmann. "A Versatile Method to Fabricate Highly In-Plane Aligned Conducting Polymer Films with Anisotropic Charge Transport and Thermoelectric Properties: The Key Role of Alkyl Side Chain Layers on the Doping Mechanism." In: *Advanced Functional Materials* 27.25 (2017). DOI: 10.1002/adfm.201700173.

[60] Ian E Jacobs, Faustine Wang, Nema Hafezi, Cristina Medina-Plaza, Thomas F Harrelson, Jun Li, Matthew P Augustine, Mark Mascal, and Adam J. Moulé. "Quantitative Dedoping of Conductive Polymers." In: *Chemistry of Materials* 29.2 (Jan. 2017), pp. 832–841. DOI: 10.1021/acs.chemmater.6b04880.

[61] Yong Xu, Huabin Sun, Ao Liu, Hui-Hui Zhu, Wenwu Li, Yen-Fu Lin, and Yong-Young Noh. "Doping: A Key Enabler for Organic Transistors." In: *Advanced Materials* 30.46 (Nov. 2018), p. 1801830. DOI: 10.1002/adma.201801830.

[62] Keehoon Kang et al. “2D coherent charge transport in highly ordered conducting polymers doped by solid state diffusion.” In: *Nature Materials* 15.8 (Aug. 2016), pp. 896–902. DOI: 10.1038/nmat4634.

[63] Alan J. Heeger. “Semiconducting and metallic polymers: The fourth generation of polymeric materials.” In: *Journal of Physical Chemistry B* 105.36 (Sept. 2001), pp. 8475–8491. DOI: 10.1021/jp011611w.

[64] Sanyin Qu, Qin Yao, Liming Wang, Zhenhua Chen, Kunqi Xu, Huarong Zeng, Wei Shi, Tiansong Zhang, Ctirad Uher, and Lidong Chen. “Highly anisotropic P3HT films with enhanced thermoelectric performance via organic small molecule epitaxy.” In: *NPG Asia Materials* 8.7 (2016). DOI: 10.1038/am.2016.97.

[65] Dean M. Delongchamp et al. “Molecular basis of mesophase ordering in a thiophene-based copolymer.” In: *Macromolecules* 41.15 (2008), pp. 5709–5715. DOI: 10.1021/ma800440f.

[66] Iain McCulloch et al. “Semiconducting Thienothiophene Copolymers: Design, Synthesis, Morphology, and Performance in Thin-Film Organic Transistors.” In: *Advanced Materials* 21.10-11 (Mar. 2009), pp. 1091–1109. DOI: 10.1002/adma.200801650.

[67] Torben Schuettfort, Benjamin Watts, Lars Thomsen, Mijung Lee, Henning Sirringhaus, and Christopher R. McNeill. “Microstructure of Polycrystalline PBTTT Films: Domain Mapping and Structure Formation.” In: *ACS Nano* 6.2 (Feb. 2012), pp. 1849–1864. DOI: 10.1021/nn2051295.

[68] Dean M. DeLongchamp, R. Joseph Kline, Youngsuk Jung, David S. Germack, Eric K. Lin, Andrew J. Moad, Lee J. Richter, Michael F. Toney, Martin Heeney, and Iain McCulloch. “Controlling the Orientation of Terraced Nanoscale “Ribbons” of a Poly(thiophene) Semiconductor.” In: *ACS Nano* 3.4 (Apr. 2009), pp. 780–787. DOI: 10.1021/nn800574f.

[69] Laure Biniek, Nicolas Leclerc, Thomas Heiser, Rony Bechara, and Martin Brinkmann. “Large Scale Alignment and Charge Transport Anisotropy of pBTTT Films Oriented by High Temperature Rubbing.” In: *Macromolecules* 46.10 (May 2013), pp. 4014–4023. DOI: 10.1021/ma400516d.

[70] Jimmy Jiahong Kuo, Max Wood, Tyler J. Slade, Mercouri G. Kanatzidis, and G. Jeffrey Snyder. “Systematic over-estimation of lattice thermal conductivity in materials with electrically-resistive grain boundaries.” In: *Energy & Environmental Science* 13.4 (2020), pp. 1250–1258. DOI: 10.1039/C9EE03921J.

[71] Dorothea Scheunemann and Martijn Kemerink. "Non-Wiedemann-Franz behavior of the thermal conductivity of organic semiconductors." In: *Physical Review B* 101.7 (Feb. 2020), p. 075206. DOI: 10.1103/PhysRevB.101.075206.

[72] Meenakshi Upadhyaya, Connor J. Boyle, Dhandapani Venkataraman, and Zlatan Aksamija. "Effects of Disorder on Thermoelectric Properties of Semiconducting Polymers." In: *Scientific Reports* 9.1 (Dec. 2019), p. 5820. DOI: 10.1038/s41598-019-42265-z.

[73] Hong Wang and Choongho Yu. "Organic Thermoelectrics: Materials Preparation, Performance Optimization, and Device Integration." In: *Joule* 3.1 (Jan. 2019), pp. 53–80. DOI: 10.1016/j.joule.2018.10.012.

[74] Hoil Yoon, Bum Suk Jung, and Hoosung Lee. "Correlation between electrical conductivity, thermal conductivity, and ESR intensity of polyaniline." In: *Synthetic Metals* 41.1-2 (Apr. 1991), pp. 699–702. DOI: 10.1016/0379-6779(91)91162-4.

[75] D. Moses and A. Denenstein. "Experimental determination of the thermal conductivity of a conducting polymer: Pure and heavily doped polyacetylene." In: *Physical Review B* 30.4 (Aug. 1984), pp. 2090–2097. DOI: 10.1103/PhysRevB.30.2090.

[76] Jun Liu, Xiaojia Wang, Dongyao Li, Nelson E. Coates, Rachel A. Segalman, and David G. Cahill. "Thermal Conductivity and Elastic Constants of PEDOT:PSS with High Electrical Conductivity." In: *Macromolecules* 48.3 (Feb. 2015), pp. 585–591. DOI: 10.1021/ma502099t.

[77] Qingshuo Wei, Masakazu Mukaida, Kazuhiro Kirihara, and Takao Ishida. "Experimental studies on the anisotropic thermoelectric properties of conducting polymer films." In: *ACS Macro Letters* 3.9 (Sept. 2014), pp. 948–952. DOI: 10.1021/mz500446z.

[78] H. Fritzsche. "A general expression for the thermoelectric power." In: *Solid State Communications* 9.21 (Nov. 1971), pp. 1813–1815. DOI: 10.1016/0038-1098(71)90096-2.

[79] Guangzheng Zuo, Hassan Abdalla, and Martijn Kemerink. "Conjugated Polymer Blends for Organic Thermoelectrics." In: *Advanced Electronic Materials* 5.11 (2019), pp. 1–20. DOI: 10.1002/aelm.201800821.

[80] Dorothea Scheunemann and Martijn Kemerink. *Thermoelectric properties of doped organic semiconductors*. LTD, 2021, pp. 165–197. DOI: 10.1016/b978-0-12-818890-3.00006-0.

[81] G. D. Mahan and J. O. Sofo. "The best thermoelectric." In: *Proceedings of the National Academy of Sciences* 93.15 (July 1996), pp. 7436–7439. DOI: 10.1073/pnas.93.15.7436.

[82] Guangzheng Zuo, Xianjie Liu, Mats Fahlman, and Martijn Kemerink. “Morphology Determines Conductivity and Seebeck Coefficient in Conjugated Polymer Blends.” In: *ACS Applied Materials & Interfaces* 10.11 (Mar. 2018), pp. 9638–9644. DOI: 10.1021/acsami.8b00122.

[83] Deepak Venkateshvaran et al. “Approaching disorder-free transport in high-mobility conjugated polymers.” In: *Nature* 515.7527 (Nov. 2014), pp. 384–388. DOI: 10.1038/nature13854.

[84] Chhatrasal Gayner and Yaron Amouyal. “Energy Filtering of Charge Carriers: Current Trends, Challenges, and Prospects for Thermoelectric Materials.” In: *Advanced Functional Materials* 30.18 (May 2020), p. 1901789. DOI: 10.1002/adfm.201901789.

[85] Kevin C. See, Joseph P. Feser, Cynthia E. Chen, Arun Majumdar, Jeffrey J. Urban, and Rachel A. Segalman. “Water-processable polymer-nanocrystal hybrids for thermoelectrics.” In: *Nano Letters* 10.11 (2010), pp. 4664–4667. DOI: 10.1021/nl102880k.

[86] Ming He, Jing Ge, Zhiqun Lin, Xuhui Feng, Xinwe Wang, Hongbin Lu, Yuliang Yang, and Feng Qiu. “Thermopower enhancement in conducting polymer nanocomposites via carrier energy scattering at the organic-inorganic semiconductor interface.” In: *Energy and Environmental Science* 5.8 (July 2012), pp. 8351–8358. DOI: 10.1039/c2ee21803h.

[87] D. M. Rowe and Gao Min. “alpha-ln sigma plot as a thermoelectric material performance indicator.” In: *Journal of Materials Science Letters* 14.9 (Jan. 1995), pp. 617–619. DOI: 10.1007/BF00586157.

[88] A. B. Kaiser. “Electronic transport properties of conducting polymers and carbon nanotubes.” In: *Reports on Progress in Physics* 64.1 (Jan. 2001), pp. 1–49. DOI: 10.1088/0034-4885/64/1/201.

[89] Morgan Lepinoy, Patrice Limelette, Bruno Schmaltz, and François Tran Van. “Thermopower scaling in conducting polymers.” In: *Scientific Reports* 10.1 (2020), pp. 1–7. DOI: 10.1038/s41598-020-64951-z.

[90] Guangzheng Zuo, Zhaojun Li, Ergang Wang, and Martijn Kemerink. “High Seebeck Coefficient and Power Factor in n-Type Organic Thermoelectrics.” In: *Advanced Electronic Materials* 4.1 (Jan. 2018), p. 1700501. DOI: 10.1002/aelm.201700501.

[91] Fatma Abdallah, Laura Ciammaruchi, Alex Jiménez-Arguijo, El-shazly M Duraia, Hossam S Ragab, Bernhard Dörling, and Mariano Campoy-Quiles. "Investigating Thermoelectric Stability under Encapsulation Using PEI-Doped CNT Films as a Model System." In: *Advanced Materials Technologies* 2000256 (May 2020), p. 2000256. DOI: `10.1002/admt.202000256`.

[92] Pradip Kar. *Doping in Conjugated Polymers*. Hoboken, NJ, USA: John Wiley & Sons, Inc., Aug. 2013, p. 156. DOI: `10.1002/9781118816639`.

[93] Alan G. MacDiarmid. ""Synthetic Metals": A Novel Role for Organic Polymers (Nobel Lecture)." In: *Angewandte Chemie International Edition* 40.14 (July 2001), pp. 2581–2590. DOI: `10.1002/1521-3773(20010716)40:14<2581::AID-ANIE2581>3.0.CO;2-2`.

[94] Hideki Shirakawa. "The Discovery of Polyacetylene Film: The Dawning of an Era of Conducting Polymers (Nobel Lecture)." In: *Angewandte Chemie International Edition* 40.14 (July 2001), pp. 2574–2580. DOI: `10.1002/1521-3773(20010716)40:14<2574::AID-ANIE2574>3.0.CO;2-N`.

[95] Ingo Salzmann, Georg Heimel, Martin Oehzelt, Stefanie Winkler, and Norbert Koch. "Molecular Electrical Doping of Organic Semiconductors: Fundamental Mechanisms and Emerging Dopant Design Rules." In: *Accounts of Chemical Research* 49.3 (Mar. 2016), pp. 370–378. DOI: `10.1021/acs.accounts.5b00438`.

[96] Brett Yurash et al. "Towards understanding the doping mechanism of organic semiconductors by Lewis acids." In: *Nature Materials* 18.12 (Dec. 2019), pp. 1327–1334. DOI: `10.1038/s41563-019-0479-0`.

[97] Han Yan and Wei Ma. "Making weak dopants strong." In: *Nature Materials* 18.12 (Dec. 2019), pp. 1269–1270. DOI: `10.1038/s41563-019-0493-2`.

[98] J L Bredas and G B Street. *Polarons, Bipolarons, and Solitons in Conducting Polymers*. Tech. rep. 1985, pp. 309–315.

[99] Olga Bubnova et al. "Semi-metallic polymers." In: *Nature Materials* 13.1 (2013), pp. 1–5. DOI: `10.1038/nmat3824`.

[100] Igor Zozoulenko, Amritpal Singh, Sandeep Kumar Singh, Viktor Gueskine, Xavier Crispin, and Magnus Berggren. "Polarons, Bipolarons, And Absorption Spectroscopy of PEDOT." In: *ACS Applied Polymer Materials* 1.1 (Jan. 2019), pp. 83–94. DOI: `10.1021/acsapm.8b00061`.

[101] Rui Qi Png, Mervin C.Y. Ang, Meng How Teo, Kim Kian Choo, Cindy Guanyu Tang, Dagmawi Belaineh, Lay Lay Chua, and Peter K.H. Ho. "Madelung and Hubbard interactions in polaron band model of doped organic semiconductors." In: *Nature Communications* 7.May (2016), pp. 1–9. DOI: 10.1038/ncomms11948.

[102] Max L Tietze, Johannes Benduhn, Paul Pahner, Bernhard Nell, Martin Schwarze, Hans Kleemann, Markus Krammer, Karin Zojer, Koen Vandewal, and Karl Leo. "Elementary steps in electrical doping of organic semiconductors." In: *Nature Communications* 9.1 (Dec. 2018), p. 1182. DOI: 10.1038/s41467-018-03302-z.

[103] Katelyn P Goetz, Derek Vermeulen, Margaret E Payne, Christian Kloc, Laurie E. McNeil, and Oana D Jurchescu. "Charge-transfer complexes: new perspectives on an old class of compounds." In: *J. Mater. Chem. C* 2.17 (2014), pp. 3065–3076. DOI: 10.1039/C3TC32062F.

[104] Duc T. Duong, Chenchen Wang, Erin Antono, Michael F. Toney, and Alberto Salleo. "The chemical and structural origin of efficient p-type doping in P3HT." In: *Organic Electronics* 14.5 (May 2013), pp. 1330–1336. DOI: 10.1016/j.orgel.2013.02.028.

[105] Keng Hoong Yim, Gregory L. Whiting, Craig E. Murphy, Jonathan J.M. Halls, Jeremy H. Burroughes, Richard H. Friend, and Ji Seon Kim. "Controlling electrical properties of conjugated polymers via a solution-based p-type doping." In: *Advanced Materials* 20.17 (Sept. 2008), pp. 3319–3324. DOI: 10.1002/adma.200800735.

[106] Emad F. Aziz, Antje Vollmer, Stefan Eisebitt, Wolfgang Eberhardt, Patrick Pingel, Dieter Neher, and Norbert Koch. "Localized charge transfer in a molecularly doped conducting polymer." In: *Advanced Materials* 19.20 (Sept. 2007), pp. 3257–3260. DOI: 10.1002/adma.200700926.

[107] Henry Méndez et al. "Charge-transfer crystallites as molecular electrical dopants." In: *Nature Communications* 6.1 (Dec. 2015), p. 8560. DOI: 10.1038/ncomms9560.

[108] Ian E Jacobs, Camila Cendra, Thomas F Harrelson, Zaira I Bedolla Valdez, Roland Faller, Alberto Salleo, and Adam J Moulé. "Polymorphism controls the degree of charge transfer in a molecularly doped semiconducting polymer." In: *Materials Horizons* 5.4 (2018), pp. 655–660. DOI: 10.1039/C8MH00223A.

[109] Bharati Neelamraju, Kristen E Watts, Jeanne E Pemberton, and Erin L Ratcliff. "Correlation of Coexistent Charge Transfer States in F 4 TCNQ-Doped P3HT with Microstructure."

In: *The Journal of Physical Chemistry Letters* 9.23 (Dec. 2018), pp. 6871–6877. DOI: 10.1021/acs.jpclett.8b03104.

[110] Elayne M. Thomas, Emily C. Davidson, Reika Katsumata, Rachel A. Segalman, and Michael L. Chabinyc. "Branched Side Chains Govern Counterion Position and Doping Mechanism in Conjugated Polythiophenes." In: *ACS Macro Letters* 7.12 (2018), pp. 1492–1497. DOI: 10.1021/acsmacrolett.8b00778.

[111] Taylor J. Aubry et al. "Dodecaborane-Based Dopants Designed to Shield Anion Electrostatics Lead to Increased Carrier Mobility in a Doped Conjugated Polymer." In: *Advanced Materials* 31.11 (Mar. 2019), p. 1805647. DOI: 10.1002/adma.201805647.

[112] Ian E. Jacobs et al. "Ion-exchange doped polymers at the degenerate limit: what limits conductivity at 100% doping efficiency?" In: (Jan. 2021).

[113] Chi Yuan Yang et al. "A thermally activated and highly miscible dopant for n-type organic thermoelectrics." In: *Nature Communications* 11.1 (2020), pp. 1–10. DOI: 10.1038/s41467-020-17063-1.

[114] Hannes Hase, Katie O'Neill, Johannes Frisch, Andreas Opitz, Norbert Koch, and Ingo Salzmann. "Unraveling the Microstructure of Molecularly Doped Poly(3-hexylthiophene) by Thermally Induced Dedoping." In: *The Journal of Physical Chemistry C* 122.45 (Nov. 2018), pp. 25893–25899. DOI: 10.1021/acs.jpcc.8b08591.

[115] Ian E Jacobs, Erik W Aasen, Julia L Oliveira, Tayane N Fonseca, John D Roehling, Jun Li, Gwangwu Zhang, Matthew P Augustine, Mark Mascal, and Adam J Moulé. "Comparison of solution-mixed and sequentially processed P3HT:F4TCNQ films: effect of doping-induced aggregation on film morphology." In: *J. Mater. Chem. C* 4.16 (2016), pp. 3454–3466. DOI: 10.1039/C5TC04207K.

[116] Alexandra F. Paterson et al. "Addition of the Lewis Acid Zn(C6F5)2 Enables Organic Transistors with a Maximum Hole Mobility in Excess of 20 cm 2 V-1s-1." In: *Advanced Materials* 31.27 (July 2019), p. 1900871. DOI: 10.1002/adma.201900871.

[117] Julianna Panidi, Alexandra F. Paterson, Dongyoon Khim, Zhuping Fei, Yang Han, Leonidas Tsetseris, George Vourlias, Panos A. Patsalas, Martin Heeney, and Thomas D. Anthopoulos. "Remarkable Enhancement of the Hole Mobility in Several Organic Small-Molecules, Polymers, and Small-Molecule:Polymer Blend Transistors by Simple Admixing of the Lewis Acid p-

Dopant B(C 6 F 5) 3." In: *Advanced Science* 5.1 (Jan. 2018), p. 1700290. DOI: 10.1002/advs.201700290.

[118] Chuan Liu, Kairong Huang, Won-Tae Park, Minmin Li, Tengzhou Yang, Xuying Liu, Lijuan Liang, Takeo Minari, and Yong-Young Noh. "A unified understanding of charge transport in organic semiconductors: the importance of attenuated delocalization for the carriers." In: *Materials Horizons* 4.4 (2017), pp. 608–618. DOI: 10.1039/C7MH00091J.

[119] Guangzheng Zuo, Olof Andersson, Hassan Abdalla, and Martijn Kemerink. "High thermoelectric power factor from multilayer solution-processed organic films." In: *Applied Physics Letters* 112.8 (Feb. 2018), p. 083303. DOI: 10.1063/1.5016908.

[120] Shrayesh N Patel, Anne M Glaudell, David Kiefer, and Michael L Chabinyc. "Increasing the Thermoelectric Power Factor of a Semiconducting Polymer by Doping from the Vapor Phase." In: *ACS Macro Letters* 5.3 (Mar. 2016), pp. 268–272. DOI: 10.1021/acsmacrolett.5b00887.

[121] Patrick Y. Yee, D. Tyler Scholes, Benjamin J. Schwartz, and Sarah H. Tolbert. "Dopant-Induced Ordering of Amorphous Regions in Regiorandom P3HT." In: *The Journal of Physical Chemistry Letters* 10.17 (Sept. 2019), pp. 4929–4934. DOI: 10.1021/acs.jpclett.9b02070.

[122] Eunhee Lim, Anne M. Glaudell, Rachel Miller, and Michael L. Chabinyc. "The Role of Ordering on the Thermoelectric Properties of Blends of Regioregular and Regiorandom Poly(3-hexylthiophene)." In: *Advanced Electronic Materials* 5.11 (2019). DOI: 10.1002/aelm.201800915.

[123] Sunbin Hwang, William J. Potscavage, Ryosuke Nakamichi, and Chihaya Adachi. "Processing and doping of thick polymer active layers for flexible organic thermoelectric modules." In: *Organic Electronics* 31 (Apr. 2016), pp. 31–40. DOI: 10.1016/j.orgel.2016.01.007.

[124] Renee Kroon, Jason D. Ryan, David Kiefer, Liyang Yu, Jonna Hynynen, Eva Olsson, and Christian Müller. "Bulk Doping of Millimeter-Thick Conjugated Polymer Foams for Plastic Thermoelectrics." In: *Advanced Functional Materials* 27.47 (Dec. 2017), p. 1704183. DOI: 10.1002/adfm.201704183.

[125] Ippei Enokida and Yukio Furukawa. "Doping-level dependent mobilities of positive polarons and bipolarons in poly(2,5-bis(3-hexadecylthiophen-2-yl)thieno[3,2-b]thiophene) (PBTTT-C16) based on an ionic-liquid-gated transistor configuration." In: *Organic Electronics* 68 (May 2019), pp. 28–34. DOI: 10.1016/j.orgel.2019.01.045.

[126] Mario Culebras, Belén Uriol, Clara M. Gómez, and Andrés Cantarero. "Controlling the thermoelectric properties of polymers: Application to PEDOT and polypyrrole." In: *Physical Chemistry Chemical Physics* 17.23 (2015), pp. 15140–15145. DOI: `10.1039/c5cp01940k`.

[127] M. Culebras, C. M. Gómez, and A. Cantarero. "Enhanced thermoelectric performance of PEDOT with different counterions optimized by chemical reduction." In: *Journal of Materials Chemistry A* 2.26 (2014), pp. 10109–10115. DOI: `10.1039/c4ta01012d`.

[128] Antonio Sánchez-Díaz, Xabier Rodríguez-Martínez, Laura Córcoles-Guija, Germán Mora-Martín, and Mariano Campoy-Quiles. "High-Throughput Multiparametric Screening of Solution Processed Bulk Heterojunction Solar Cells." In: *Advanced Electronic Materials* 4.10 (2018). DOI: `10.1002/aelm.201700477`.

[129] Bernhard Dörling, Osnat Zapata-Arteaga, and Mariano Campoy-Quiles. "A setup to measure the Seebeck coefficient and electrical conductivity of anisotropic thin-films on a single sample." In: *Review of Scientific Instruments* 91.10 (Oct. 2020), p. 105111. DOI: `10.1063/5.0021715`.

[130] Eunhee Lim, Kelly A. Peterson, Gregory M. Su, and Michael L. Chabinyc. "Thermoelectric Properties of Poly(3-hexylthiophene) (P3HT) Doped with 2,3,5,6-Tetrafluoro-7,7,8,8-tetracyanoquinodimethane (F 4 TCNQ) by Vapor-Phase Infiltration." In: *Chemistry of Materials* 30.3 (Feb. 2018), pp. 998–1010. DOI: `10.1021/acs.chemmater.7b04849`.

[131] Jonna Hynynen, David Kiefer, Liyang Yu, Renee Kroon, Rahim Munir, Aram Amassian, Martijn Kemerink, and Christian Müller. "Enhanced Electrical Conductivity of Molecularly p-Doped Poly(3-hexylthiophene) through Understanding the Correlation with Solid-State Order." In: *Macromolecules* 50.20 (Oct. 2017), pp. 8140–8148. DOI: `10.1021/acs.macromol.7b00968`.

[132] D. M. DeLongchamp, R. J. Kline, E. K. Lin, D. A. Fischer, L. J. Richter, L. A. Lucas, Martin Heeney, Iain McCulloch, and J. E. Northrup. "High Carrier Mobility Polythiophene Thin Films: Structure Determination by Experiment and Theory." In: *Advanced Materials* 19.6 (Mar. 2007), pp. 833–837. DOI: `10.1002/adma.200602651`.

[133] Gisela L. Schulz and Sabine Ludwigs. "Controlled Crystallization of Conjugated Polymer Films from Solution and Solvent Vapor for Polymer Electronics." In: *Advanced Functional Materials* 27.1 (2017). DOI: `10.1002/adfm.201603083`.

[134] Frank C Spano. “Modeling disorder in polymer aggregates: The optical spectroscopy of regioregular poly(3-hexylthiophene) thin films.” In: *The Journal of Chemical Physics* 122.23 (June 2005), p. 234701. DOI: 10.1063/1.1914768.

[135] Jenny Clark, Jui-Fen Chang, Frank C Spano, Richard H. Friend, and Carlos Silva. “Determining exciton bandwidth and film microstructure in polythiophene films using linear absorption spectroscopy.” In: *Applied Physics Letters* 94.16 (Apr. 2009), p. 163306. DOI: 10.1063/1.3110904.

[136] Matthew Newville, Till Stensitzki, Daniel B. Allen, and Antonino Ingargiola. “LMFIT: Non-Linear Least-Square Minimization and Curve-Fitting for Python.” In: (Sept. 2014). DOI: 10.5281/ZENODO.11813.

[137] Ping Hsun Chu, Gang Wang, Boyi Fu, Dalsu Choi, Jung Ok Park, Mohan Srinivasarao, and Elsa Reichmanis. “Synergistic Effect of Regioregular and Regiorandom Poly(3-hexylthiophene) Blends for High Performance Flexible Organic Field Effect Transistors.” In: *Advanced Electronic Materials* 2.2 (2016), pp. 1–12. DOI: 10.1002/aelm.201500384.

[138] Peter J. Brown, Henning Sirringhaus, Mark Harrison, Maxim Shkunov, and Richard H Friend. “Optical spectroscopy of field-induced charge in self-organized high mobility poly(3-hexylthiophene).” In: *Physical Review B* 63.12 (Mar. 2001), p. 125204. DOI: 10.1103/PhysRevB.63.125204.

[139] Ian E. Jacobs and Adam J. Moulé. “Controlling Molecular Doping in Organic Semiconductors.” In: *Advanced Materials* 29.42 (Nov. 2017), p. 1703063. DOI: 10.1002/adma.201703063.

[140] Tengzhou Ma, Ban Xuan Dong, Garrett L. Grocke, Joseph Strzalka, and Shrayesh N. Patel. “Leveraging Sequential Doping of Semiconducting Polymers to Enable Functionally Graded Materials for Organic Thermoelectrics.” In: *Macromolecules* 53.8 (Apr. 2020), pp. 2882–2892. DOI: 10.1021/acs.macromol.0c00402.

[141] J. S. Chappell, A. N. Bloch, W. A. Bryden, M. Maxfield, T. O. Poehler, and D. O. Cowan. “Degree of charge transfer in organic conductors by infrared absorption spectroscopy.” In: *Journal of the American Chemical Society* 103.9 (May 1981), pp. 2442–2443. DOI: 10.1021/ja00399a066.

[142] C Francis, D. Fazzi, S B Grimm, F Paulus, S Beck, S. Hillebrandt, A. Pucci, and J Zaumseil. “Raman spectroscopy and microscopy of electrochemically and chemically doped high-mobility semiconducting polymers.” In: *Journal of Materials Chemistry C* 5.25 (2017), pp. 6176–6184. DOI: 10.1039/C7TC01277B.

[143] G. M. Paternò, V. Robbiano, K. J. Fraser, C. Frost, V. García Sakai, and F. Cacialli. “Neutron Radiation Tolerance of Two Benchmark Thiophene-Based Conjugated Polymers: the Importance of Crystallinity for Organic Avionics.” In: *Scientific Reports* 7.1 (Feb. 2017), p. 41013. DOI: 10.1038/srep41013.

[144] Frank Neese. “The ORCA program system.” In: *Wiley Interdisciplinary Reviews: Computational Molecular Science* 2.1 (2012), pp. 73–78. DOI: 10.1002/wcms.81.

[145] Oleksiy V Khavryuchenko and Benjamin Frank. “Theoretical Investigation of Anion-Radical States of Edge-Oxidized Carbon Model Clusters.” In: *The Journal of Physical Chemistry A* 121.16 (Apr. 2017), pp. 3167–3173. DOI: 10.1021/acs.jpca.7b02437.

[146] Aleksandr Perevedentsev and Mariano Campoy-Quiles. “Rapid and high-resolution patterning of microstructure and composition in organic semiconductors using ‘molecular gates’.” In: *Nature Communications* 11.1 (Dec. 2020), p. 3610. DOI: 10.1038/s41467-020-17361-8.

[147] Leo J. van der Pauw. “A method of measuring the resistivity and Hall coefficient on lamellae of arbitrary shape.” In: *Philips Technical Review* 20 (1958), pp. 220–224.

[148] Aaron J. Schmidt, Ramez Cheaito, and Matteo Chiesa. “A frequency-domain thermoreflectance method for the characterization of thermal properties.” In: *Review of Scientific Instruments* 80.9 (2009). DOI: 10.1063/1.3212673.

[149] Osnat Zapata-Arteaga, Bernhard Dörling, Aleksandr Perevedentsev, Jaime Martín, J Sebastian Reparaz, and Mariano Campoy-Quiles. “Closing the Stability–Performance Gap in Organic Thermoelectrics by Adjusting the Partial to Integer Charge Transfer Ratio.” In: *Macromolecules* 53.2 (Jan. 2020), pp. 609–620. DOI: 10.1021/acs.macromol.9b02263.

[150] Jun Li, Guangwu Zhang, Daniella M Holm, Ian E Jacobs, Bin Yin, Pieter Stroeve, Mark Mascal, and Adam J. Moulé. “Introducing Solubility Control for Improved Organic P-Type Dopants.” In: *Chemistry of Materials* 27.16 (Aug. 2015), pp. 5765–5774. DOI: 10.1021/acs.chemmater.5b02340.

[151] Paul Beyer et al. “State-of-Matter-Dependent Charge-Transfer Interactions between Planar Molecules for Doping Applications.” In: *Chemistry of Materials* 31.4 (Feb. 2019), pp. 1237–1249. DOI: 10.1021/acs.chemmater.8b01447.

[152] Ana M Valencia and Caterina Cocchi. “Electronic and Optical Properties of Oligothiophene-F4TCNQ Charge-Transfer Complexes: The Role of the Donor Conjugation Length.” In: *The*

Journal of Physical Chemistry C 123.14 (Apr. 2019), pp. 9617–9623. DOI: 10.1021/acs.jpcc.9b01390.

[153] Jack Fuzell, Ian E Jacobs, Sophia Ackling, Thomas F Harrelson, David M Huang, Delmar Larsen, and Adam J. Moulé. “Optical Dedoping Mechanism for P3HT:F4TCNQ Mixtures.” In: *The Journal of Physical Chemistry Letters* 7.21 (Nov. 2016), pp. 4297–4303. DOI: 10.1021/acs.jpclett.6b02048.

[154] Lingyun Zhu, Eung-Gun Kim, Yuanping Yi, and Jean-Luc Brédas. “Charge Transfer in Molecular Complexes with 2,3,5,6-Tetrafluoro-7,7,8,8-tetracyanoquinodimethane (F 4 - TCNQ): A Density Functional Theory Study.” In: *Chemistry of Materials* 23.23 (Dec. 2011), pp. 5149–5159. DOI: 10.1021/cm201798x.

[155] Björn Lüssem, Chang-Min Keum, Daniel Kasemann, Ben Naab, Zhenan Bao, and Karl Leo. “Doped Organic Transistors.” In: *Chemical Reviews* 116.22 (Nov. 2016), pp. 13714–13751. DOI: 10.1021/acs.chemrev.6b00329.

[156] Jun Yamamoto and Yukio Furukawa. “Electronic and Vibrational Spectra of Positive Polarons and Bipolarons in Regioregular Poly(3-hexylthiophene) Doped with Ferric Chloride.” In: *The Journal of Physical Chemistry B* 119.13 (Apr. 2015), pp. 4788–4794. DOI: 10.1021/jp512654b.

[157] Yuexing Zhang, Robert Steyrleuthner, and Jean-Luc Bredas. “Charge Delocalization in Oligomers of Poly(2,5-bis(3-alkylthiophene-2-yl)thieno[3,2- b]thiophene) (PBTTT).” In: *The Journal of Physical Chemistry C* 120.18 (May 2016), pp. 9671–9677. DOI: 10.1021/acs.jpcc.6b02378.

[158] Justin E. Cochran, Matthias J. N. Junk, A. M. Glaudell, P. Levi Miller, John S. Cowart, Michael F. Toney, Craig J. Hawker, Bradley F. Chmelka, and Michael L. Chabinyc. “Molecular Interactions and Ordering in Electrically Doped Polymers: Blends of PBTTT and F 4 TCNQ.” In: *Macromolecules* 47.19 (Oct. 2014), pp. 6836–6846. DOI: 10.1021/ma501547h.

[159] Nichole Cates Miller et al. “Use of X-Ray Diffraction, Molecular Simulations, and Spectroscopy to Determine the Molecular Packing in a Polymer-Fullerene Bimolecular Crystal.” In: *Advanced Materials* 24.45 (Nov. 2012), pp. 6071–6079. DOI: 10.1002/adma.201202293.

[160] Mariano Campoy-Quiles. “Will organic thermoelectrics get hot?” In: *Philosophical Transactions of the Royal Society A: Mathematical, Physical and Engineering Sciences* 377.2152 (Aug. 2019), p. 20180352. DOI: 10.1098/rsta.2018.0352.

[161] D. Tyler Scholes, Patrick Y. Yee, Jeffrey R. Lindemuth, Hyeyeon Kang, Jonathan Onorato, Raja Ghosh, Christine K. Luscombe, Frank C. Spano, Sarah H. Tolbert, and Benjamin J. Schwartz. "The Effects of Crystallinity on Charge Transport and the Structure of Sequentially Processed F 4 TCNQ-Doped Conjugated Polymer Films." In: *Advanced Functional Materials* 27.44 (Nov. 2017), p. 1702654. DOI: 10.1002/adfm.201702654.

[162] Hanhui Xie, Heng Wang, Chenguang Fu, Yintu Liu, G. Jeffrey Snyder, Xinbing Zhao, and Tiejun Zhu. "The intrinsic disorder related alloy scattering in ZrNiSn half-Heusler thermoelectric materials." In: *Scientific Reports* 4.1 (May 2015), p. 6888. DOI: 10.1038/srep06888.

[163] Yongjin Lee, Alexander J. Pak, and Gyeong S. Hwang. "What is the thermal conductivity limit of silicon germanium alloys?" In: *Physical Chemistry Chemical Physics* 18.29 (2016), pp. 19544–19548. DOI: 10.1039/C6CP04388G.

[164] D. Abbaszadeh, A. Kunz, G. A. H. Wetzelaer, J. J. Michels, N. I. Crăciun, K. Koynov, I. Lieberwirth, and P. W. M. Blom. "Elimination of charge carrier trapping in diluted semiconductors." In: *Nature Materials* 15.6 (June 2016), pp. 628–633. DOI: 10.1038/nmat4626.

[165] David Kiefer, Liyang Yu, Erik Fransson, Andrés Gómez, Daniel Primetzhofer, Aram Amassian, Mariano Campoy-Quiles, and Christian Müller. "A Solution-Doped Polymer Semiconductor:Insulator Blend for Thermoelectrics." In: *Advanced Science* 4.1 (Jan. 2017), p. 1600203. DOI: 10.1002/advs.201600203.

[166] Guanghao Lu, Laju Bu, Sijun Li, and Xiaoniu Yang. "Bulk Interpenetration Network of Thermoelectric Polymer in Insulating Supporting Matrix." In: *Advanced Materials* 26.15 (Apr. 2014), pp. 2359–2364. DOI: 10.1002/adma.201305320.

[167] Michael L. Chabinyc, Michael F. Toney, R. Joseph Kline, Iain McCulloch, and Martin Heeney. "X-ray Scattering Study of Thin Films of Poly(2,5-bis(3-alkylthiophen-2-yl)thieno[3,2-b]thiophene)." In: *Journal of the American Chemical Society* 129.11 (Mar. 2007), pp. 3226–3237. DOI: 10.1021/ja0670714.

[168] Ricardo Garcia and Roger Proksch. "Nanomechanical mapping of soft matter by bimodal force microscopy." In: *European Polymer Journal* 49.8 (2013), pp. 1897–1906. DOI: 10.1016/j.eurpolymj.2013.03.037.

[169] Adam D. Printz, Suchol Savagatrup, Daniel Rodriquez, and Darren J. Lipomi. "Role of molecular mixing on the stiffness of polymer:fullerene bulk heterojunction films." In: *Solar*

Energy Materials and Solar Cells 134 (Mar. 2015), pp. 64–72. DOI: 10.1016/j.solmat.2014.11.030.

[170] Robbert A. de Graaf, Andre P. Karman, and Léon P. B. M. Janssen. “Material Properties and Glass Transition Temperatures of Different Thermoplastic Starches After Extrusion Processing.” In: *Starch - Stärke* 55.2 (Feb. 2003), pp. 80–86. DOI: 10.1002/star.200390020.

[171] K. K. Chee. “Dependence of glass transition temperature on chain flexibility and intermolecular interactions in polymers.” In: *Journal of Applied Polymer Science* 43.6 (Sept. 1991), pp. 1205–1208. DOI: 10.1002/app.1991.070430622.

[172] Samuel E Root, Mohammad A Alkhadra, Daniel Rodriquez, Adam D Printz, and Darren J Lipomi. “Measuring the Glass Transition Temperature of Conjugated Polymer Films with Ultraviolet–Visible Spectroscopy.” In: *Chemistry of Materials* 29.7 (Apr. 2017), pp. 2646–2654. DOI: 10.1021/acs.chemmater.7b00242.

[173] Ioannis M. Kalogeras and Witold Brostow. “Glass transition temperatures in binary polymer blends.” In: *Journal of Polymer Science Part B: Polymer Physics* 47.1 (Jan. 2009), pp. 80–95. DOI: 10.1002/polb.21616.

[174] Xiao Xue, George Chandler, Xinran Zhang, R. Joseph Kline, Zhuping Fei, Martin Heeney, Peter J Diemer, Oana D Jurchescu, and Brendan T. O’Connor. “Oriented Liquid Crystalline Polymer Semiconductor Films with Large Ordered Domains.” In: *ACS Applied Materials & Interfaces* 7.48 (Dec. 2015), pp. 26726–26734. DOI: 10.1021/acsami.5b08710.

[175] D Tyler Scholes, Steven A Hawks, Patrick Y Yee, Hao Wu, Jeffrey R Lindemuth, Sarah H Tolbert, and Benjamin J Schwartz. “Overcoming Film Quality Issues for Conjugated Polymers Doped with F 4 TCNQ by Solution Sequential Processing: Hall Effect, Structural, and Optical Measurements.” In: *The Journal of Physical Chemistry Letters* 6.23 (Dec. 2015), pp. 4786–4793. DOI: 10.1021/acs.jpclett.5b02332.

[176] Stephen Dongmin Kang and G. Jeffrey Snyder. “Charge-transport model for conducting polymers.” In: *Nature Materials* 16.2 (Feb. 2017), pp. 252–257. DOI: 10.1038/nmat4784.

[177] Renxuan Xie et al. “Glass transition temperature from the chemical structure of conjugated polymers.” In: *Nature Communications* 11.1 (Dec. 2020), p. 893. DOI: 10.1038/s41467-020-14656-8.

[178] Masoud Ghasemi et al. "Delineation of Thermodynamic and Kinetic Factors that Control Stability in Non-fullerene Organic Solar Cells." In: *Joule* 3.5 (May 2019), pp. 1328–1348. DOI: `10.1016/j.joule.2019.03.020`.

[179] Yanbin Wang, Jinxing Chen, Hyung Do Kim, Biaobing Wang, Ryo Iriguchi, and Hideo Ohkita. "Ternary Blend Solar Cells Based on a Conjugated Polymer With Diketopyrrolopyrrole and Carbazole Units." In: *Frontiers in Energy Research* 6.OCT (Oct. 2018), p. 113. DOI: `10.3389/fenrg.2018.00113`.

[180] Si Wang, Andre Mayer, Khalid Dhima, Christian Steinberg, and Hella-Christin Scheer. "Imprint-induced ordering of crystallizing polymers below stamp protrusions." In: *Journal of Vacuum Science & Technology B, Nanotechnology and Microelectronics: Materials, Processing, Measurement, and Phenomena* 31.6 (Nov. 2013), 06FB06. DOI: `10.1116/1.4831765`.

[181] Trinh Tung Ngo, Duc Nghia Nguyen, and Van Tuyen Nguyen. "Glass transition of PCBM, P3HT and their blends in quenched state." In: *Advances in Natural Sciences: Nanoscience and Nanotechnology* 3.4 (Sept. 2012), p. 045001. DOI: `10.1088/2043-6262/3/4/045001`.

[182] Beate Burkhart, Petr P. Khlyabich, and Barry C. Thompson. "Influence of the Ethylhexyl Side-Chain Content on the Open-Circuit Voltage in rr-Poly(3-hexylthiophene- co -3-(2-ethylhexyl)thiophene) Copolymers." In: *Macromolecules* 45.9 (May 2012), pp. 3740–3748. DOI: `10.1021/ma300263a`.

[183] Jon Maiz, Miguel Muñoz Rojo, Begoña Abad, Adam Andrew Wilson, Aurora Nogales, Diana-Andra Borca-Tasciuc, Theodorian Borca-Tasciuc, and Marisol Martín-González. "Enhancement of thermoelectric efficiency of doped PCDTBT polymer films." In: *RSC Advances* 5.82 (2015), pp. 66687–66694. DOI: `10.1039/C5RA13452H`.

[184] Nicolas Blouin, Alexandre Michaud, and Mario Leclerc. "A low-bandgap poly(2,7-carbazole) derivative for use in high-performance solar cells." In: *Advanced Materials* 19.17 (Sept. 2007), pp. 2295–2300. DOI: `10.1002/adma.200602496`.

[185] Hunan Yi, Solyman Al-Faifi, Ahmed Iraqi, Darren C. Watters, James Kingsley, and David G. Lidzey. "Carbazole and thienyl benzo[1,2,5]thiadiazole based polymers with improved open circuit voltages and processability for application in solar cells." In: *Journal of Materials Chemistry* 21.35 (Sept. 2011), pp. 13649–13656. DOI: `10.1039/c1jm12089a`.

[186] Christian Müller. “On the glass transition of polymer semiconductors and its impact on polymer solar cell stability.” In: *Chemistry of Materials* 27.8 (2015), pp. 2740–2754. DOI: 10.1021/acs.chemmater.5b00024.

[187] Gada Muleta Fanta, Pawel Jarka, Urszula Szeluga, Tomasz Tański, and Jung Yong Kim. “Phase Behavior of Amorphous/Semicrystalline Conjugated Polymer Blends.” In: *Polymers* 12.8 (July 2020), p. 1726. DOI: 10.3390/polym12081726.

[188] Yuan Zhang and Paul W.M. Blom. “Electron and hole transport in poly(fluorene-benzothiadiazole).” In: *Applied Physics Letters* 98.14 (2011), pp. 2011–2014. DOI: 10.1063/1.3574907.

[189] Wenyue Dong, Shanfeng Xue, Ping Lu, Jian Deng, Donglin Zhao, Cheng Gu, and Yuguang Ma. “Functionality of peripheral side chain for enhanced performance of conjugated polymer-F8BT as an example.” In: *Journal of Polymer Science Part A: Polymer Chemistry* 49.21 (Nov. 2011), pp. 4549–4555. DOI: 10.1002/pola.24898.

[190] Aleksandr Perevedentsev, Paul N. Stavrinou, Paul Smith, and Donal D.C. Bradley. “Solution-crystallization and related phenomena in 9,9-dialkyl-fluorene polymers. II. Influence of side-chain structure.” In: *Journal of Polymer Science, Part B: Polymer Physics* 53.21 (2015), pp. 1492–1506. DOI: 10.1002/polb.23797.

[191] S. Janietz, D. D.C. Bradley, M. Grell, C. Giebeler, M. Inbasekaran, and E. P. Woo. “Electrochemical determination of the ionization potential and electron affinity of poly(9,9-dioctylfluorene).” In: *Applied Physics Letters* 73.17 (Oct. 1998), pp. 2453–2455. DOI: 10.1063/1.122479.

[192] Chaohua Cui, Wai-Yeung Wong, and Yongfang Li. “Improvement of open-circuit voltage and photovoltaic properties of 2D-conjugated polymers by alkylthio substitution.” In: *Energy Environ. Sci.* 7.7 (June 2014), pp. 2276–2284. DOI: 10.1039/C4EE00446A.

[193] Jingping Yin, Weihua Zhou, Lin Zhang, Yuanpeng Xie, Zoukangning Yu, Jun Shao, Wei Ma, Jianrong Zeng, and Yiwang Chen. “Improved Glass Transition Temperature towards Thermal Stability via Thiols Solvent Additive versus DIO in Polymer Solar Cells.” In: *Macromolecular Rapid Communications* 38.20 (Oct. 2017), p. 1700428. DOI: 10.1002/marc.201700428.

[194] Tao Jiang, Jie Yang, Youtian Tao, Cong Fan, Lingwei Xue, Zhiguo Zhang, Hai Li, Yongfang Li, and Wei Huang. “Random terpolymer with a cost-effective monomer and comparable efficiency to PTB7-Th for bulk-heterojunction polymer

solar cells.” In: *Polymer Chemistry* 7.4 (Jan. 2016), pp. 926–932. DOI: `10.1039/c5py01771h`.

[195] Qing Ya Li, Jingyang Xiao, Lu Ming Tang, Hua Chun Wang, Ziming Chen, Zhiyong Yang, Hin Lap Yip, and Yun Xiang Xu. “Thermally stable high performance non-fullerene polymer solar cells with low energy loss by using ladder-type small molecule acceptors.” In: *Organic Electronics* 44 (May 2017), pp. 217–224. DOI: `10.1016/j.orgel.2017.02.008`.

[196] Zicheng Ding, Xiaojing Long, Bin Meng, Keyan Bai, Chuandong Dou, Jun Liu, and Lixiang Wang. “Polymer solar cells with open-circuit voltage of 1.3 V using polymer electron acceptor with high LUMO level.” In: *Nano Energy* 32 (Feb. 2017), pp. 216–224. DOI: `10.1016/j.nanoen.2016.12.041`.

[197] Ming Ao Pan, Tsz Ki Lau, Yabing Tang, Yi Ching Wu, Tao Liu, Kun Li, Ming Chou Chen, Xinhui Lu, Wei Ma, and Chuanlang Zhan. “16.7%-efficiency ternary blended organic photovoltaic cells with PCBM as the acceptor additive to increase the open-circuit voltage and phase purity.” In: *Journal of Materials Chemistry A* 7.36 (Sept. 2019), pp. 20713–20722. DOI: `10.1039/c9ta06929a`.

[198] Luyao Lu, Wei Chen, Tao Xu, and Luping Yu. “High-performance ternary blend polymer solar cells involving both energy transfer and hole relay processes.” In: *Nature Communications* 6.1 (June 2015), pp. 1–7. DOI: `10.1038/ncomms8327`.

[199] A C Mayer, Michael F Toney, Shawn R Scully, Jonathan Rivnay, Christoph J Brabec, Marcus Scharber, Marcus Koppe, Martin Heeney, Iain Mcculloch, and Michael D Mcgehee. “Bimolecular Crystals of Fullerenes in Conjugated Polymers and the Implications of Molecular Mixing for Solar Cells.” In: (). DOI: `10.1002/adfm.200801684`.